

ISABELLA STEVANI

**Robust Control of a 2-DOF Parallel Mechanism  
Combining Feedback Linearization and H-infinity  
Design**

São Paulo  
2020

ISABELLA STEVANI

**Robust Control of a 2-DOF Parallel Mechanism  
Combining Feedback Linearization and H-infinity  
Design**

Dissertation submitted to Escola Politécnica of the Universidade de São Paulo for degree of Master of Science.

São Paulo  
2020

ISABELLA STEVANI

**Robust Control of a 2-DOF Parallel Mechanism  
Combining Feedback Linearization and H-infinity  
Design**

Dissertation submitted to Escola Politécnica of the Universidade de São Paulo for degree of Master of Science.

Concentration area:

3139 - Systems engineering

Advisor:

Prof. Dr. Diego Colón

São Paulo  
2020

Autorizo a reprodução e divulgação total ou parcial deste trabalho, por qualquer meio convencional ou eletrônico, para fins de estudo e pesquisa, desde que citada a fonte.

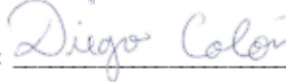
Este exemplar foi revisado e corrigido em relação à versão original, sob responsabilidade única do autor e com a anuência de seu orientador.

São Paulo, 02 de Fevereiro de 2021

Assinatura do autor:



Assinatura do orientador:



#### Catálogo-na-publicação

Stevani, Isabella

Robust Control of a 2-DOF Parallel Mechanism Combining Feedback Linearization and H-infinity Design / I. Stevani -- versão corr. -- São Paulo, 2021.

91 p.

Dissertação (Mestrado) - Escola Politécnica da Universidade de São Paulo. Departamento de Engenharia de Telecomunicações e Controle.

1. Robust control 2. Feedback linearization 3. H-infinity control 4. Robotics 5. Parallel mechanism I. Universidade de São Paulo. Escola Politécnica. Departamento de Engenharia de Telecomunicações e Controle II. t.

# ACKNOWLEDGMENTS

I would like to acknowledge everyone who supported, advised and encouraged me since I begun this journey towards my Master's degree. Professors, family, friends, colleagues, university staff, thank you all!

A second acknowledgment to CAPES – Coordenação de Aperfeiçoamento de Pessoal de Nível Superior for sponsoring this research (process number 1771660).

I would like to dedicate the remaining of this section for some special acknowledgements.

First of all, a special thanks to my parents, Adriana and Marcio. I gave you two all my gratitude for always taught me the importance of studying hard and perceive my dreams. Without you and my little brother Marcelo I would not be able to accomplish the great things I did in my life, and I am very proud to belong to such a strong family.

A special acknowledgement to my supervisor professor, Prof. Dr. Diego Colón. Thank you for your patience and dedication, and specially for believing and encouraging me during the development of this research.

Another special thanks to my colleague André Garnier Coutinho, who introduced me to the world of parallel mechanisms. Being all this area such a novelty to me, thank you for your patience and fertile discussions concerning primordial topics of this research.

One more special acknowledge to the very special and unique crew this Master's gave me. Arthur Castello Branco de Oliveira, Ivan Fischman Ekman Simões and Katharina Reis Farina, although the main destination of this Master's was to accomplish the proposed project, the trip was bright and fun mainly due to you, folks. While my Master's degree journey is finally coming to an end, hopefully this is only the beginning of our friendship.

Last but not least, a special thanks to my partner in crime and best friend Vitor Finotti Ferreira, who supported me in every decision I took since my graduation, even the ones he did not quite agree. Without you I would never have the strength and resilience to conclude my Master's degree, thank you so much for everything.

*"If you are neutral in situations of injustice, you have chosen the side of the oppressor".*

-Desmond Tutu

# RESUMO

Este trabalho apresenta o controle robusto de uma planta não linear considerando incertezas de parâmetros, no caso um mecanismo paralelo de 2-GDL. Primeiramente, as modelagens dinâmica e cinemática do robô foram deduzidas a partir de uma nova metodologia, esta baseada nos modelos dos subsistemas seriais que compõe a topologia paralela que são combinados posteriormente a partir de equações de restrições mecânicas, assim gerando o modelo completo do robô paralelo. Em seguida, uma arquitetura de controle robusta combinando controle  $H_\infty$  e linearização por realimentação foi projetada a fim de se garantir robustez de estabilidade e desempenho do sistema, inclusive na presença de incertezas de parâmetros do modelo. Com o objetivo de validar tanto a modelagem do mecanismo quanto seu controle, resultados simulados foram obtidos.

**Palavras-Chave** – Controle robusto, Linearização por realimentação, Controle H-infinito, Robótica, Mecanismo paralelo.

# ABSTRACT

This work presents the robust control of a nonlinear plant with uncertain parameters, in this case a 2-DOF parallel mechanism. First, the robot dynamic and kinematic models were computed using a new methodology based on the serial subsystems models that compose the parallel topology, which are later pieced together through mechanical constraints to form the complete parallel robot model. Then, a robust control architecture combining  $H_\infty$  design and feedback linearization was designed in order to guarantee robust performance and stability even in the presence of uncertain parameters in the model. To validate both mechanism's modeling and control, simulation results were provided.

**Keywords** – Robust control, Feedback linearization, H-infinity control, Robotics, Parallel mechanism.

# LIST OF FIGURES

Figure 1	2-DOF parallel mechanism schematics. . . . .	22
Figure 2	RR serial mechanism schematics. . . . .	22
Figure 3	Feedback linearization schematics. . . . .	35
Figure 4	Feedback linearization with feedforward loop for model matrices computation schematics. . . . .	36
Figure 5	Control loop schematics. . . . .	38
Figure 6	Standard control configuration. . . . .	44
Figure 7	$S/KS/T$ Mixed-sensitivity control configuration. . . . .	47
Figure 8	Control closed-loop. . . . .	47
Figure 9	RRR spatial serial mechanism. . . . .	48
Figure 10	Robustness analysis. . . . .	52
Figure 11	Nominal model response for sinusoidal input. . . . .	55
Figure 12	Uncertain model response for sinusoidal input. . . . .	57
Figure 13	Randomly sampled variables versus Latin hypercube samples (bidi- mensional space). . . . .	59
Figure 14	How the LHS works when increasing the number of samples (bidi- mensional space). . . . .	59
Figure 15	End-effector reference trajectory. . . . .	61
Figure 16	Example of Fourier Transform analysis. . . . .	62
Figure 17	Frequency response considering nominal parameters (Table 3) and no disturbances. . . . .	62
Figure 18	Frequency response considering nominal parameters (Table 3) and feedforward loop for model matrices computation. . . . .	63
Figure 19	Frequency response considering uncertain parameters (Table 4) and feedforward loop for model matrices computation. . . . .	64

Figure 20	Example of total harmonic distortion analysis. . . . .	65
Figure 21	Total harmonic distortion analysis for sample 11 open-loop simulation. . . . .	67
Figure 22	Frequency response considering uncertain parameters (Table 4) and feedforward loop for model matrices computation, with new proposed nominal plant $G(s)$ . . . . .	68
Figure 23	Worst case uncertainty $l_m(\omega)$ and its upper bound $w_\Delta(s)$ with respect to the centric nominal model $G(s)$ . . . . .	69
Figure 24	Weight functions for mixed-sensitivity design. . . . .	70
Figure 25	$H_\infty$ controller order reduction. . . . .	71
Figure 26	Closed-loop transfer functions $S(s)$ and $T(s)$ with respect to the centric nominal model $G(s)$ . . . . .	72
Figure 27	Closed-loop frequency response considering uncertain parameters (Table 4) and feedforward loop for model matrices computation. . . . .	73
Figure 28	Total harmonic distortion analysis for sample 11 closed-loop simulation. . . . .	74
Figure 29	THD analysis comparison. . . . .	76
Figure 30	Time domain simulation with 1 Hz reference signal. . . . .	78
Figure 31	Time domain simulation with 2 Hz reference signal. . . . .	79
Figure 32	Time domain simulation with 4 Hz reference signal. . . . .	80

# LIST OF TABLES

Table 1	Denavit-Hatenberg parameters for the RRR spatial serial mechanism.	51
Table 2	3-DOF RRR spatial serial mechanism nominal parameters. . . . .	53
Table 3	2-DOF parallel mechanism nominal parameters. . . . .	58
Table 4	2-DOF parallel mechanism uncertain parameters. . . . .	60
Table 5	Total harmonic distortion analysis for open-loop system. . . . .	66
Table 6	Total harmonic distortion analysis for closed-loop system. . . . .	75
Table 7	RMSE for closed-loop time domain simulation. . . . .	76

# LIST OF ABBREVIATIONS

CLS	Closed-loop system
CTC	Computed-torque control
DOB	Disturbance observer
DOBC	Disturbance observer-based control
DOF	Degrees of freedom
FFT	Fast Fourier transform
FL	Feedback linearization
FT	Fourier transform
GDL	Graus de liberdade
GMSIE	Grupo de Mecânica dos Sólidos e Impacto em Estruturas
LHS	Latin hypercube sampling
MIMO	Multi-input multi-output
NOC	Natural orthogonal complement
NP	Nominal performance
NS	Nominal stability
OLS	Open-loop system
PD	Proportional-derivative
PID	Proportional-integral-derivative
RMSE	Root-mean-square error
RP	Robust performance
RS	Robust stability
SISO	Single-input single-output
SMC	Sliding mode control
SSV	Structured singular values
THD	Total harmonic distortion
VWP	Virtual work principle

# LIST OF SYMBOLS

$c(x)$	$\cos(x)$
$H_\infty$	H-infinity
$\ \cdot\ _\infty$	H-infinity norm
$F_l(\cdot)$	Lower fractional transformation
R	Rotational joint
$s(x)$	$\sin(x)$
$\theta_{a+b}$	$\theta_a + \theta_b$
$\theta_{a,b+c}$	$\theta_{a,b} + \theta_{a,c}$

# CONTENTS

<b>1</b>	<b>Introduction</b>	<b>14</b>
1.1	Research Objectives . . . . .	15
1.2	Publications . . . . .	15
1.3	Bibliography Review . . . . .	16
<b>2</b>	<b>2-DOF Parallel Mechanism</b>	<b>21</b>
2.1	Forward Kinematics . . . . .	23
2.2	Forward Dynamics . . . . .	25
2.2.1	Serial Subsystems . . . . .	25
2.2.2	Coupling Equations . . . . .	29
2.3	Inverse Dynamics . . . . .	31
2.4	Actuator Model . . . . .	32
<b>3</b>	<b>Control Design</b>	<b>34</b>
3.1	Feedback Linearization . . . . .	34
3.1.1	Model Matrices Computation Through Feedforward Loop . . . . .	35
3.2	$H_\infty$ Control . . . . .	36
3.2.1	Robust Control Analysis . . . . .	36
3.2.1.1	Nominal Stability and Performance . . . . .	37
3.2.1.2	Robust Stability and Performance . . . . .	39
3.2.2	$H_\infty$ Control Design . . . . .	43
3.2.2.1	Mixed-sensitivity Method . . . . .	46
<b>4</b>	<b>Results and Discussion</b>	<b>48</b>
4.1	Preliminary Results For Desing Proposal Validation . . . . .	48

4.2	Parallel Model . . . . .	57
4.2.1	Nominal Parameters . . . . .	57
4.2.2	Uncertain Parameters . . . . .	57
4.3	Feedback Linearization Analysis . . . . .	59
4.4	Robust Control Analysis and Design . . . . .	68
<b>5</b>	<b>Conclusions</b>	<b>81</b>
	<b>References</b>	<b>82</b>

# 1 INTRODUCTION

There is no doubt that the usage of robots in different fields of study is constantly increasing. With applications from aerospace to medical research, robots have been playing a major role in different tasks as, for example, pick-and-place operations (RICHARD; CLAVEL, 2012), manufacturing processes (KOBEL; CLAVEL, 2011) and even surgical procedures (BEIRA et al., 2011). Among many architectures, the closed-chain robotic mechanism – also known as parallel robot – has been explored for high performance tasks due to its high precision and rigidity, fast dynamics, load capacity and light weight. On the other hand, parallel mechanisms present reduced workspace and more complex modeling in comparison to serial ones (ALMEIDA; HESS-COELHO, 2010).

Following the definition presented in (MERLET; GOSSELIN, 2008), a closed-chain mechanism is constituted by at least two independent kinematic chains linking the end-effector to a fixed base. In the case of the 2-DOF parallel mechanism considered in this work, two distinguished kinematic chains link the end-effector to the robot’s fixed base, configuring a pentagon shape. As shown in (COUTINHO, 2020), different control strategies have been applied to the same parallel mechanism used in this work: sliding mode control (SMC), feedback linearization (FL) and computed torque control (CTC). In order to evaluate the performance of a different control strategy within this same platform, this work proposes a robust control design combining  $H_\infty$  control and feedback linearization. The main objective of this control strategy is to present good trajectory tracking even in the presence of model uncertainties. A similar control approach was proposed by Rachedi, Bouri and Hemici (2014) and applied to the Delta robot, which is a 3-DOF parallel mechanism. Moreover, there are many other control strategies that have been used to control different parallel architectures, from the traditional designs as the PID controller (AL-MAYYAH; ALDAIR; CHATWIN, 2020) and the LQR control (YUN; LI, 2009) to the more unconventional ones such as adaptive control (ANSARIESHLAGHI; EBERHARD, 2019), fuzzy control (WEN et al., 2019) and deep reinforcement learning (MA et al., 2019).

Regarding model uncertainties, this work relies on the latin hypercube sampling (LHS) technique to generate the uncertain samples. Typically, random selection is used (LIU et al., 2021; WU et al., 2016). Although the LHS has been used before in robotics (HE et al., 2018), no works were found in the literature applying it to a parallel mechanism as is proposed in this work, to the best of the author's knowledge. Another novelty is the total harmonic distortion (THD) analysis carried out comparing the level of nonlinear influence between the open-loop linearized system and the closed-loop response with the proposed robust controller. In most cases, the THD is applied in power electronics applications (RAMIREZ; PACAS, 2016; VUKIC; MRVIC; KATIC, 2019) but the author did not find any work applying it to robotics, as far as the author knows.

This work is divided as follows: Chapter 1 presents the main objectives of this research together with a bibliography review highlighting the state-of-the-art in controlling parallel mechanisms; Chapter 2 presents the kinematic and dynamic modeling of the 2-DOF parallel mechanism; Chapter 3 presents the robust control design; Chapter 4 presents the simulation results and addresses some relevant discussions and, finally, Chapter 5 summarizes the obtained conclusions.

## 1.1 Research Objectives

For the master's degree project, the final goal is to combine the robustness of the  $H_\infty$  design with the simplicity of the feedback linearization technique into a controller capable of achieving robust stability and performance for a complex nonlinear uncertain system as the 2-DOF parallel mechanism considered in this work. This main objective could be divided in three main topics:

1. Modeling of the 2-DOF parallel mechanism;
2. Robust control design considering model uncertainties;
3. Validation through simulation results.

## 1.2 Publications

In order to do a first attempt of implementation and validation of the robust control design proposed in Chapter 3, the proposed design was applied to a 3-DOF RRR spatial serial mechanism, with its main results presented in the XXII Brazilian Conference on

Automation on September 2018 (CBA 2018) and published in the conference proceedings with the title "H-Infinity Control of a 3-DOF RRR Spatial Serial Mechanism" (STEVANI et al., 2018). Latter, the parallel mechanism modeling together with simulation and experimental results of applying a feedback linearization control law were presented in the XXV ABCM International Congress of Mechanical Engineering on October 2019 (COBEM 2019) and published with the title "Design and Control of a 2-DOF Parallel Mechanism" (COUTINHO et al., 2019) in the conference proceedings.

### 1.3 Bibliography Review

Robotic mechanisms with parallel architecture have been used in different tasks, both in industrial and research applications (HESS-COELHO; HASZL, 2005), due to their potential to achieve faster dynamics, higher rigidity and precision with lower weight energy consumption in comparison to robots with serial topology (PASHKEVICH; CHABLAT; WENGER, 2006; PATEL; GEORGE, 2012). All this potential comes at a cost: reduced workspace and more complex kinematic and dynamic modeling, which could be overcome with better choices regarding the mechanism's topology as its parameters, joints and mechanical design (HARTMANN, 2018).

On the modeling of these parallel mechanisms, several formulations for the dynamic model of these robots are found in the literature. The two most popular ones are the formalism of Newton-Euler (DASGUPTA; MRUTHYUNJAYA, 1998; ZHANG; ZHANG; CHEN, 2014; LI et al., 2003; ARIAN et al., 2017; SHIAU; TSAI; TSAI, 2008) and Lagrange (LI; XU, 2005; SINGH; SANTHAKUMAR, 2015; SINGH et al., 2015; SINGH; VINOOTH; SANTHAKUMAR, 2014; YAO et al., 2017), although both approaches present inherent mathematical complications that make them inefficient: the need of computing reactive efforts and the usage of multipliers, respectively (COUTINHO et al., 2019).

The Virtual Work Principle (VWP) and the Virtual Power Principle (VPP) are other useful approaches since they avoid the calculation of reactive efforts. However, their need for complex mathematical manipulations and sometimes simplifying hypotheses may difficult their application (CODOUREY; BURDET, 1997; GALLARDO-ALVARADO; RODRÍGUEZ-CASTRO; DELOSSANTOS-LARA, 2018; LI; XU, 2009; STAICU, 2009a; STAICU, 2009b; STAICU; ZHANG, 2008; STAICU; ZHANG; RUGESCU, 2006; ZHAO; GAO, 2009; ZHU et al., 2005). There are also the works that use the Boltzmann-Hamel formalism (ALTUZARRA et al., 2015) and the natural orthogonal complement formulation (NOC) (AKBARZADEH; ENFERADI; SHARIFNIA, 2013; XI; SINATRA, 2002),

which could be interesting choices since they can reuse preconceived models while also avoiding the calculation of reactive efforts. Another possibility is to use a method based on Cartan connection and differential geometry that can be applied to write the kinematical and dynamical equations in several representations, as for example quaternions and dual-quaternions and other Lie groups and algebras representations. Among the advantages of the method is the fact that quaternion and dual-quaternion formulations become more intuitive (COLÓN, 2018; COLÓN, 2015b; COLÓN, 2015a; COLÓN, 2014). Further discussions regarding modeling approaches can be found in Coutinho (2020).

Focusing now on the possible choices of control strategies for these types of robots, consolidated techniques previously applied to serial mechanisms are also being adapted to be applied in parallel ones (HARTMANN, 2018). In order to do that, the modeling complexity inherent to all parallel mechanisms is an obstacle that needs to be surpassed (PACCOT; ANDREFF; MARTINET, 2009). The model could be simplified to be applied in real time control systems as done in Almeida and Hess-Coelho (2013), but the control performance could be compromised as observed in Molina (2012) with both simulation and experimental results.

As pointed out in Zubizarreta et al. (2013), the complexity of the complete inverse dynamics caused by the presence of more than one kinematic chain demands too much computational effort. An interesting strategy to avoid this issue is performed in Wang et al. (2017) where a computed-torque control (CTC) with feedforward terms is used, exempting the need of powerful hardware since the model computation could be performed offline. Another problem that needs to be addressed – not only for closed-chain robots, it is worth mentioning – is the model uncertainties, which includes uncertain parameters, external disturbances, load variation, neglected dynamics and nonlinear effects such as backlash, friction, elastic deformation and clearance (HESELBACH et al., 2004; ZHAN et al., 2018; GRZELCZYK; STAŃCZYK; AWREJCEWICZ, 2016).

Complex control designs involving robust (RIGATOS; SIANO; POMARES, 2017), adaptive (ACHILI et al., 2012) and nonlinear (NATAL; CHEMORI; PIERROT, 2016) control theories have been applied on parallel mechanisms as well (HESELBACH et al., 2004). On the nonlinear control category, sliding mode control (PILTAN; SULAIMAN, 2012) is a popular choice due to its enhanced robustness to model uncertainties in comparison to feedback linearization approach. Singh and Santhakumar (2015) present a robust version of the SMC while Zeinali and Notash (2010) opt for combine an adaptive approach with the SMC. Model and non-model based control approaches have already been experimentally applied to the parallel robot studied in this work: sliding mode con-

trol, computed-torque control and PD control (COUTINHO, 2020). In order to propose a different control design to evaluate its performance in comparison to the previously implemented ones, two control designs were investigated.

The first and more audacious attempt was the disturbance observer-based control (DOBC) (CHEN et al., 2015) combined with CTC. In this configuration, the CTC was responsible for linearize and control the nominal part of the parallel mechanism nonlinear model while the disturbance observer (DOB) would estimate and cancel on real-time any disturbance – including external disturbances, model uncertainties and parameters variation – perceived in the control loop, thus enhancing the robustness of the CTC design. Different methodologies for the DOB design were studied: the linear DOB applied to a delta parallel mechanism from Ramírez-Neria et al. (2015), the nonlinear DOB applicable to single-input single-output (SISO) systems with mismatched disturbances from Yang, Chen and Li (2011) and its extension to multi-input multi-output (MIMO) systems from Yang, Li and Chen (2012). Unfortunately, none of the approaches worked out when applied to the 2-DOF parallel mechanism, mainly due to the lack of available time and expertise on DOBs of this work’s author.

The second and more tangible approach combined  $H_\infty$  design with, again, CTC. The purpose of the CTC was the same as in the previously attempt, but now the  $H_\infty$  controller was aiming to attenuate the disturbances instead of canceling them. Similar control approaches have been implemented for different applications. Rigatos, Siano and Raffo (2016) proposed an  $H_\infty$  design with online local linearization to control robotic mechanisms, with dedicated results for closed-chain mechanisms (RIGATOS; SIANO; POMARES, 2017). Terra et al. (2000) applied the  $H_\infty$  design with feedback linearization (FL) to an underactuated manipulator robot and shown that, in the presence of model uncertainties, this robust control design led to better results in comparison to a PID controller. Pan, Jin and Wang (2011) shown improved robustness when applying the  $H_\infty$  design combined with FL for roll stabilizing of autonomous underwater vehicle under wave disturbances. This second approach was chosen to control the parallel mechanism studied in this work and its design is carried out in Chapter 3.

Basically,  $H_\infty$  control theory constructs an optimization problem in the frequency domain which its solution will result in a controller capable of guaranteeing robust stability and performance of the closed-loop system. This optimization is formulated around the  $H_\infty$  norm, which can be interpreted as the distance in the complex plane from the origin to the farthest point in the Nyquist plot of the considered transfer function (ZHOU; DOYLE, 1998). With that in mind, the goal is to find the controller that produces the closed-loop

with the smallest  $H_\infty$  norm in terms of the desired stability and performance criteria. To define these criteria, first of all the family of plants must be known – that is, the possible plants that could exist due to different parameter values. In this analysis, a trade-off between robustness and performance must be considered: guaranteeing robustness for a larger family of plants leads to worse performance and vice-versa (SKOGESTAD; POSTLETHWAITE, 2007).

In order to generate this family of plants, different sets of parameters must be chosen, all of them respecting the tolerances defined for each parameter. Instead of just choosing each set randomly within the predefined boundaries, this work proposes the use of the latin hypercube sampling technique. The LHS provides a more complete coverage of the sample space since each sample is chosen considering the total number of samples, so the final set is more uniformly distributed along the sample space (HELTON; DAVIS; JOHNSON, 2005; HELTON; DAVIS, 2002). With this approach, the parameter set is effectively distributed inside the sample space. Another advantage of using the LHS is to be able to fix the number of computed samples despite the number of parameters in each sample, as explained in more details in Chapter 4.

With the family of plants defined, different methods can be used to define the stability and performance criteria in order to formulate the  $H_\infty$  control problem. The most popular ones are the mixed-sensitivity and the loop-shaping designs (SKOGESTAD; POSTLETHWAITE, 2007). As examples of these two methods been applied to robotics, Mohammed and Hasnaa (2017) used mixed-sensitivity in the control of a 2-DOF serial manipulator, Alkamachi and Erçelebi (2018) also used mixed-sensitivity but for a quadcopter and, finally, there's the work of Hongliang (2013) where the loop-shaping methodology is applied to flexible systems. Both approaches rely on the frequency domain analysis, specially when dealing with unmodelled disturbances (SKOGESTAD; POSTLETHWAITE, 2007). To quantify the influence of these disturbances in the frequency domain, this work applied sinusoidal inputs with different frequencies to the linearized model – that is, the resultant model after the FL is applied to the nonlinear system – then the Fourier Transform (FT) was used to compute the magnitude response for different disturbances scenarios (BRACEWELL, 1986; WU et al., 2012; TIMCENKO; ALLEN, 1993).

To construct this magnitude response, the magnitude of the model output for the fundamental frequency is considered. Since it is possible that multiple harmonics show up in the FFT analysis – specially when considering highly nonlinear disturbances – it is necessary to quantify the influence of this harmonics over the linear response, the latter represented by the fundamental frequency magnitude. To check if this information is

representative, the total harmonic distortion of the model output is analyzed as well. The THD is the maximum magnitude difference between the fundamental frequency and, usually, the first five harmonics. The lower the THD is, the more representative the linear response is (SHMILOVITZ, 2005). More details can be found in Chapter 4.

## 2 2-DOF PARALLEL MECHANISM

After years of research and validation, many modeling approaches were developed and consolidated for serial mechanisms. Yet, there is not an established methodology to model parallel ones. Searching in the available literature led to the discovery of a simple and systematic methodology developed by Coutinho and Hess-Coelho based on the work of Orsino (ORSINO; HESS-COELHO; PESCE, 2015; ORSINO, 2016; ORSINO; HESS-COELHO, 2015) to compute parallel mechanisms' kinematic and dynamic models, applicable to any closed-chain architecture (COUTINHO, 2020).

This methodology's main idea is to fragment the parallel system into serial subsystems and then piece them together through mechanical constraints obtained from the robot kinematics. In the specific case of the parallel mechanism (Figure 1) considered in this research, the system is fragmented into two RR serial mechanisms (Figure 2) combined through four constraint equations, leading to a 2-DOF mechanism.

In this work, three types of analysis are relevant regarding the parallel mechanism model: forward kinematics, forward dynamics and inverse dynamics. The first one describes the end-effector's coordinates in terms of the joint angles, and is useful to compute reference trajectories and the coupling equations used in the dynamic modeling. The second one describes the mechanism motion in terms of the actuator's efforts, and is used to simulate the mechanism behavior. And the last one is just the opposite: it describes the necessary actuator's efforts to bring the system to its actual state through its kinematics, and is used in control design.

The methodology can be summarized in the following steps:

1. Fragment the parallel mechanism into serial subsystems and obtain the dynamic model for each one of them;
2. Obtain the kinematic constraints between the serial subsystems that piece them together to form the parallel mechanism;

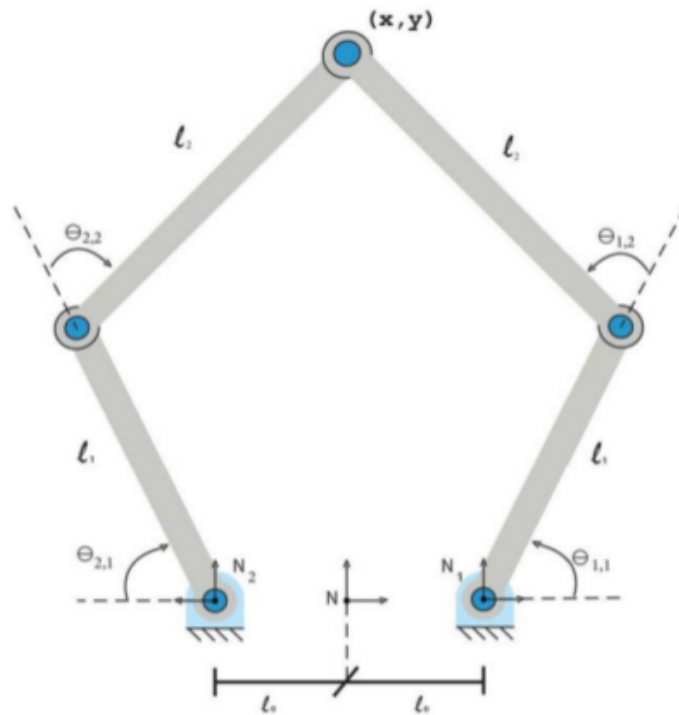


Figure 1: 2-DOF parallel mechanism schematics. Source: Coutinho (2020).

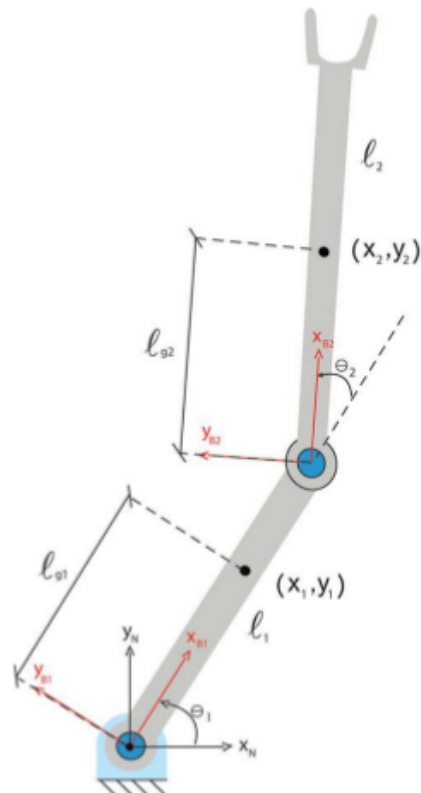


Figure 2: RR serial mechanism schematics. Source: Coutinho (2020).

3. Combine the subsystems dynamic models through the kinematic links found in the previous step (coupling equations);

4. Enforce the mechanical constraints during forward dynamic simulation to avoid drifts due to accumulated error;
5. Compute the inverse dynamic model in terms of the actuated coordinates to obtain the control effort.

The complete modeling methodology description can be found in Coutinho (2020), and the entire deduction for the case of the 2-DOF parallel mechanism presented in this Chapter was published in the XXV ABCM International Congress of Mechanical Engineering (COUTINHO et al., 2019).

## 2.1 Forward Kinematics

In order to obtain the end-effector's coordinates in terms of the joint angles, two possible paths exist in the parallel architecture described in Figure 1: one beginning at the right link and the other at the left one.

Taking the right path leads to:

$$\begin{cases} x = l_0 + l_1 c(\theta_{1,1}) + l_2 c(\theta_{1,1+2}) \\ y = l_1 s(\theta_{1,1}) + l_2 s(\theta_{1,1+2}) \end{cases}, \quad (2.1)$$

while taking the left path leads to:

$$\begin{cases} x = -l_0 - l_1 c(\theta_{2,1}) - l_2 c(\theta_{2,1+2}) \\ y = l_1 s(\theta_{2,1}) + l_2 s(\theta_{2,1+2}) \end{cases}. \quad (2.2)$$

where  $l_j$  [m] is the  $j^{th}$  link length,  $(x, y)$  [m] is the end-effector's linear position and  $\theta_{i,j}$  [rad] is the  $j^{th}$  link joint angle with respect to the  $i^{th}$  kinematic chain. Also,  $s(x)$  and  $c(x)$  states for  $\sin(x)$  and  $\cos(x)$ , respectively, and  $\theta_{a,b+c}$  states for  $\theta_{a,b} + \theta_{a,c}$ .

Since the end-effector coordinates must satisfy both paths, equations (2.1) and (2.2) are combined into:

$$\phi(q) = 0, \quad (2.3)$$

with  $\phi(q)$  as a vector function in terms of the generalized coordinates vector given by:

$$\phi(q) = \begin{bmatrix} x - (l_0 + l_1 c(\theta_{1,1}) + l_2 c(\theta_{1,1+2})) \\ y - (l_1 s(\theta_{1,1}) + l_2 s(\theta_{1,1+2})) \\ x - (-l_0 - l_1 c(\theta_{2,1}) - l_2 c(\theta_{2,1+2})) \\ y - (l_1 s(\theta_{2,1}) + l_2 s(\theta_{2,1+2})) \end{bmatrix}, \quad (2.4)$$

where  $q$  stands for the generalized coordinates vector given by:

$$q = \begin{bmatrix} x \\ y \\ \theta_{1,1} \\ \theta_{1,2} \\ \theta_{2,1} \\ \theta_{2,2} \end{bmatrix}. \quad (2.5)$$

Through equation (2.3), its first variation can be computed, resulting in the system's direct kinematics:

$$\delta\phi(q) = A(q)\delta q = 0, \quad (2.6)$$

with

$$A(q) = \frac{\partial\phi}{\partial q}, \quad (2.7)$$

given by:

$$A(q) = \begin{bmatrix} 1 & 0 & l_1 s(\theta_{1,1}) + l_2 s(\theta_{1,1+2}) & l_2 s(\theta_{1,1+2}) & 0 & 0 \\ 0 & 1 & -l_1 c(\theta_{1,1}) - l_2 c(\theta_{1,1+2}) & -l_2 c(\theta_{1,1+2}) & 0 & 0 \\ 1 & 0 & 0 & 0 & -l_1 s(\theta_{2,1}) - l_2 s(\theta_{2,1+2}) & -l_2 s(\theta_{2,1+2}) \\ 0 & 1 & 0 & 0 & -l_1 c(\theta_{2,1}) - l_2 c(\theta_{2,1+2}) & -l_2 c(\theta_{2,1+2}) \end{bmatrix}. \quad (2.8)$$

Now, the generalized coordinates vector  $q$  could be split into actuated and passive coordinates, the former being the actuated joints and the latter being the passive joints and the end-effector position:

$$q = Q_a q_a + Q_p q_p, \quad (2.9)$$

with

$$Q_a = \begin{bmatrix} 0 & 0 \\ 0 & 0 \\ 1 & 0 \\ 0 & 0 \\ 0 & 1 \\ 0 & 0 \end{bmatrix}, \quad Q_p = \begin{bmatrix} 1 & 0 & 0 & 0 \\ 0 & 1 & 0 & 0 \\ 0 & 0 & 0 & 0 \\ 0 & 0 & 1 & 0 \\ 0 & 0 & 0 & 0 \\ 0 & 0 & 0 & 1 \end{bmatrix}, \quad q_a = \begin{bmatrix} \theta_{1,1} \\ \theta_{2,1} \end{bmatrix}, \quad q_p = \begin{bmatrix} x \\ y \\ \theta_{1,2} \\ \theta_{2,2} \end{bmatrix}, \quad (2.10)$$

and so does its first variation computed in equation (2.6):

$$\delta q = Q_a \delta q_a + Q_p \delta q_p. \quad (2.11)$$

Substituting equation (2.11) in (2.6) results in:

$$A Q_a \delta q_a + A Q_p \delta q_p = 0. \quad (2.12)$$

Manipulating the above equation, one gets:

$$\delta q = C(q) \delta q_a, \quad (2.13)$$

with

$$C(q) = Q_a - Q_p (A(q) Q_p)^{-1} (A(q) Q_a), \quad (2.14)$$

which will be useful together with  $A(q)$  to compute the system dynamics in the next section.

## 2.2 Forward Dynamics

The forward dynamics is computed mainly for simulation purposes. For the parallel mechanism, the serial subsystems dynamics are derived and then combined through the coupling equations to form the complete parallel architecture. All steps are described in the next subsections.

### 2.2.1 Serial Subsystems

The dynamic model of a mechanism presents the relation between the generalized forces acting on it (actuators effort) and its configuration (states) over time. In the case

of the Euler-Lagrange method, this relation is obtained balancing the different energy sources acting on the system: the kinematic and potential energies (LANCZOS, 2012).

First of all, in order to compute the kinetic and potential energies equations, it is necessary to find the kinematic relations between the center of mass positions of each link in terms of the joint angles – that is, the relation between the linear and angular displacements. As can be seen in Figure 2, the kinematic relations are given by:

$$\begin{cases} x_1 = l g_1 c(\theta_1) \\ y_1 = l g_1 s(\theta_1) \\ x_2 = l_1 c(\theta_1) + l g_2 c(\theta_{1+2}) \\ y_2 = l_1 s(\theta_1) + l g_2 s(\theta_{1+2}) \end{cases}, \quad (2.15)$$

where  $(x_i, y_i)$  [m] is the  $i^{th}$  link's center of mass linear position,  $l g_j$  [m] is the distance from the beginning of the  $i^{th}$  link to its center of mass,  $l_i$  [m] is the  $i^{th}$  link length and  $\theta_i$  [rad] is the  $i^{th}$  link joint angle. Also,  $\theta_{a+b}$  stands for  $\theta_a + \theta_b$ .

Assuming that each robot link is a rigid body, the total kinetic energy of the  $i^{th}$  link is given by the sum of its linear and angular kinematic energies:

$$K_i = \frac{1}{2} m_i \|v_i\|^2 + \frac{1}{2} J_i \|\omega_i\|^2, \quad (2.16)$$

with  $m_i$  [kg] is the  $i^{th}$  link mass and the principal moments of inertia  $J_i$  [kg.m<sup>2</sup>] of the  $i^{th}$  link in relation of its center of mass,  $v_i$  [m/s] is the center of mass absolute linear velocity of the  $i^{th}$  link and  $\omega_i$  [rad/s] is the  $i^{th}$  link absolute angular velocity.

The linear and angular velocities can be obtained differentiating the linear and angular positions, respectively:

$$\begin{cases} v_i = \frac{d}{dt}(x_i, y_i) = \left( \frac{d}{dt}x_i, \frac{d}{dt}y_i \right) \\ \omega_i = \frac{d}{dt}\theta_{xy,i} \end{cases}, \quad (2.17)$$

where  $\theta_{xy,i}$  is the angular position of the  $i^{th}$  link in terms of the static reference coordinates.

Replacing the kinematic relations from equation (2.15) in the above equation, one finds that:

$$K_1 = \left( \frac{1}{2} m_1 l g_1^2 + \frac{1}{2} J_1 \right) \dot{\theta}_1^2, \quad (2.18)$$

$$\begin{aligned} K_2 = & \left( \frac{1}{2} m_2 l_1^2 + \frac{1}{2} m_2 l g_2^2 + m_2 l_1 l g_2 c(\theta_2) + \frac{1}{2} J_2 \right) \dot{\theta}_1^2 + \\ & + \left( \frac{1}{2} m_2 l g_2^2 + \frac{1}{2} J_2 \right) \dot{\theta}_2^2 + \left( m_2 l g_2^2 + m_2 l_1 l g_2 c(\theta_2) + J_2 \right) \dot{\theta}_1 \dot{\theta}_2. \end{aligned} \quad (2.19)$$

Now, assuming that the only contribution is the gravitational force, the potential energy of the  $i^{th}$  link is given by:

$$P_i = -m_i \bar{g}^T(x_i, y_i), \quad (2.20)$$

where  $\bar{g}$  is the gravity acceleration vector given by:

$$\bar{g} = g \begin{bmatrix} 0 \\ -1 \end{bmatrix}, \quad (2.21)$$

with  $g$  [m/s<sup>2</sup>] as the gravity constant.

Replacing the kinematic relations from equation (2.15) in the above equation, one finds that:

$$P_1 = gm_1 l g_1 s(\theta_1), \quad (2.22)$$

$$P_2 = gm_2 l_1 s(\theta_1) + gm_2 l g_2 s(\theta_{1+2}). \quad (2.23)$$

The Lagrangian is defined as the difference between the total kinematic and potential energies acting on the mechanism, that is:

$$L = \sum_i K_i - \sum_i P_i. \quad (2.24)$$

In the case of the 2-DOF RR serial mechanism, the Lagrangian is given by:

$$\begin{aligned} L = & \left( \frac{1}{2} m_1 l g_1^2 + \frac{1}{2} J_1 + \frac{1}{2} m_2 l_1^2 + \frac{1}{2} m_2 l g_2^2 + m_2 l_1 l g_2 c(\theta_2) + \frac{1}{2} J_2 \right) \dot{\theta}_1^2 + \\ & + \left( \frac{1}{2} m_2 l g_2^2 + \frac{1}{2} J_2 \right) \dot{\theta}_2^2 + \left( m_2 l g_2^2 + m_2 l_1 l g_2 c(\theta_2) + J_2 \right) \dot{\theta}_1 \dot{\theta}_2 - \\ & - gm_1 l g_1 s(\theta_1) - gm_2 l_1 s(\theta_1) - gm_2 l g_2 s(\theta_{1+2}). \end{aligned} \quad (2.25)$$

Before applying the Euler-Lagrange equation, it is defined a generalized coordinates vector in terms of the joint angles:

$$q = \begin{bmatrix} \theta_1 \\ \theta_2 \end{bmatrix}. \quad (2.26)$$

Then, the Euler-Lagrange equation is defined as a function of the Lagrangian:

$$\frac{d}{dt} \frac{\partial L}{\partial \dot{q}_i} - \frac{\partial L}{\partial q_i} = u_i, \quad (2.27)$$

where  $u_i$  is the  $i^{th}$  actuator effort applied to the  $i^{th}$  link.

Applying the Euler-Lagrange equation (2.27) to the 2-DOF RR serial mechanism Lagrangian from equation (2.25) results in:

$$\begin{aligned}
u_1 &= \left( m_1 l g_1^2 + J_1 + m_2 l_1^2 + m_2 l g_2^2 + 2 m_2 l_1 l g_2 c(\theta_2) + J_2 \right) \ddot{\theta}_1 + \\
&\quad + \left( m_2 l g_2^2 + m_2 l_1 l g_2 c(\theta_2) + J_2 \right) \ddot{\theta}_2 - 2 m_2 l_1 l g_2 s(\theta_2) \dot{\theta}_1 \dot{\theta}_2 - m_2 l_1 l g_2 s(\theta_2) \dot{\theta}_2^2 + \\
&\quad + g m_1 l g_1 c(\theta_1) + g m_2 l_1 c(\theta_1) + g m_2 l g_2 c(\theta_{1+2}), \\
u_2 &= \left( m_2 l g_2^2 + m_2 l_1 l g_2 c(\theta_2) + J_2 \right) \ddot{\theta}_1 + \left( m_2 l g_2^2 + J_2 \right) \ddot{\theta}_2 + m_2 l_1 l g_2 s(\theta_2) \dot{\theta}_1^2 + \\
&\quad + g m_2 l g_2 c(\theta_{1+2}).
\end{aligned} \tag{2.28}$$

The Euler-Lagrange equation can be rewritten in the so-called closed-form given by:

$$M_i(q_i) \ddot{q}_i + V_i(q_i, \dot{q}_i) + G_i(q_i) = U_i, \tag{2.29}$$

with

$$q_i = \begin{bmatrix} \theta_{i,1} \\ \theta_{i,2} \end{bmatrix},$$

where  $M_i(q_i)$  is the inertia matrix,  $V_i(q_i, \dot{q}_i)$  is the vector of centrifugal and Coriolis terms,  $G_i(q_i)$  is the vector of gravitational forces and  $U_i$  is the vector of generalized actuators' efforts (COUTINHO; COELHO, 2016; DOBRIANSKYJ; COUTINHO; HESS-COELHO, 2014; CRAIG, 2005). The coefficients of the matrix  $M(q)$  and vectors  $V(q, \dot{q})$  and  $G(q)$  are the ones from equation (2.28):

$$M(q) = \begin{bmatrix} D_{11}(q) & D_{12}(q) \\ D_{12}(q) & D_{22}(q) \end{bmatrix}, \tag{2.30}$$

$$V(q, \dot{q}) = \begin{bmatrix} D_{111}(q) \dot{\theta}_1^2 + D_{122}(q) \dot{\theta}_2^2 + D_{112}(q) \dot{\theta}_1 \dot{\theta}_2 + D_{121}(q) \dot{\theta}_2 \dot{\theta}_1 \\ D_{211}(q) \dot{\theta}_1^2 + D_{222}(q) \dot{\theta}_2^2 + D_{212}(q) \dot{\theta}_1 \dot{\theta}_2 + D_{221}(q) \dot{\theta}_2 \dot{\theta}_1 \end{bmatrix}, \tag{2.31}$$

$$G(q) = \begin{bmatrix} D_1(q) \\ D_2(q) \end{bmatrix}, \tag{2.32}$$

with

$$\begin{aligned}
D_1(q) &= g(m_1 l g_1 + m_2 l_1) c(\theta_1) + g m_2 l g_2 c(\theta_{1+2}), \\
D_2(q) &= g m_2 l g_2 c(\theta_{1+2}), \\
D_{11}(q) &= m_1 l g_1^2 + J z_1 + m_2 (l_1^2 + l g_2^2) + J z_2 + 2 m_2 l_1 l g_2 c(\theta_2), \\
D_{21}(q) &= D_{12}(q) = m_2 l g_2^2 + J z_2 + m_2 l_1 l g_2 c(\theta_2), \\
D_{22}(q) &= m_2 l g_2^2 + J z_2, \\
D_{221}(q) &= D_{212}(q) = D_{222}(q) = D_{111}(q) = 0, \\
D_{122}(q) &= D_{121}(q) = D_{112}(q) = -m_2 l_1 l g_2 s(\theta_2), \\
D_{211}(q) &= m_2 l_1 l g_2 s(\theta_2).
\end{aligned}$$

## 2.2.2 Coupling Equations

The coupling equations are the matrices  $A(q)$  and  $C(q)$  computed in Section 2.1. First, in order to guarantee that the coupling equations are satisfied during simulation – which means guaranteeing  $\phi(q) = 0$  – an asymptotically stable second order dynamics can be imposed to  $\phi$  so that, if  $\phi$  respects the coupling condition in the beginning of the simulation, the condition will remain satisfied. Doing so,  $\phi$  dynamics is given by:

$$\ddot{\phi}(q) + 2\bar{\lambda}\dot{\phi}(q) + \bar{\lambda}^2\phi(q) = 0, \quad (2.33)$$

with  $\bar{\lambda}$  faster than the robot dynamics. This results in:

$$A(q)\ddot{q} + \dot{A}(q)\dot{q} + 2\bar{\lambda}A(q)\dot{q} + \bar{\lambda}^2\phi = 0. \quad (2.34)$$

Now, to combine the two serial subsystems into the parallel mechanism through the coupling equations, the VWP needs to be applied. Essentially, the VWP states that the sum of all the efforts performed by a mechanism must be zero, therefore the sum of the work performed by internal and external forces related to this mechanism must be equal to zero (TSAI, 1999). For each serial subsystem, the sum of the forces is given by:

$$f_i(q) = U_i - M_i(q_i)\ddot{q}_i - V_i(q_i, \dot{q}_i) - G_i(q_i). \quad (2.35)$$

The sum of the work is defined as the sum of the forces multiplied by the virtual displacement given in terms of the generalized coordinates vector, therefore applying the

VWP results in:

$$f_i^T(q)\delta q_i = 0. \quad (2.36)$$

Since  $\delta q_i$  is an independent virtual coordinates vector, equation (2.36) is satisfied by:

$$f_i(q) = 0. \quad (2.37)$$

The same analysis could be applied to the complete parallel mechanism concatenating the two models with the end-effector, resulting in:

$$f(q) = U - H(q)\ddot{q} - h(q, \dot{q}), \quad (2.38)$$

where  $H(q) = M(q)$  and  $h(q, \dot{q}) = V(q, \dot{q}) + G(q)$  with:

$$M(q) = \begin{bmatrix} 0 & 0 & 0 \\ 0 & M_1(q_1) & 0 \\ 0 & 0 & M_2(q_2) \end{bmatrix}, \quad V(q, \dot{q}) = \begin{bmatrix} 0 \\ V_1(q_1, \dot{q}_1) \\ V_2(q_2, \dot{q}_2) \end{bmatrix}, \quad G(q) = \begin{bmatrix} 0 \\ G_1(q_1) \\ G_2(q_2) \end{bmatrix}, \quad U = \begin{bmatrix} 0 \\ U_1 \\ U_2 \end{bmatrix}.$$

Applying now the VWP to  $f(q)$ , one gets:

$$f^T(q)\delta q = 0, \quad (2.39)$$

but now it can't be concluded that  $f(q) = 0$  because the coordinates in vector  $\delta q$  are not independent. To overcome this issue, matrix  $C(q)$  can be used. Substituting equation (2.13) in (2.39) and doing some mathematical manipulation, one gets:

$$\delta q_a^T C^T(q) f(q) = 0, \quad (2.40)$$

where the vector  $\delta q_a$  has independent coordinates, resulting in:

$$C^T(q) f(q) = 0, \quad (2.41)$$

which is the forward dynamics equation.

Lastly, to simulate the parallel mechanism forward dynamics and guarantee that the coupling conditions are satisfied at the same time, equations (2.34) and (2.41) need to be evaluated together, resulting in the complete simulation forward dynamic model given

by:

$$\begin{bmatrix} C^T(q)H(q) \\ A(q) \end{bmatrix} \ddot{q} = \begin{bmatrix} C^T(q)(U - h(q, \dot{q})) \\ -\dot{A}(q)\dot{q} - 2\bar{\lambda}A(q)\dot{q} - \bar{\lambda}^2\phi(q) \end{bmatrix}. \quad (2.42)$$

## 2.3 Inverse Dynamics

In control design, the inverse dynamics is used to define the control effort needed to drive the system actual state to the desired one. In order to obtain it, both forward kinematics and dynamics are considered. Back to Section 2.1, equation (2.13) shows a relation between the generalized and the actuated coordinates vectors. This same relation can also be found for the vectors' derivatives:

$$\dot{q} = C(q)\dot{q}_a. \quad (2.43)$$

Differentiating the above equation, one gets:

$$\ddot{q} = C(q)\ddot{q}_a + \dot{C}(q)\dot{q}_a, \quad (2.44)$$

To compute  $\dot{C}(q)$ , equation (2.6) is expanded to the generalized coordinate first derivative:

$$A(q)\dot{q} = 0. \quad (2.45)$$

Differentiating the above equation, one gets:

$$\dot{A}(q)\dot{q} + A(q)\ddot{q} = 0. \quad (2.46)$$

Now, differentiating equation (2.9) two times results in:

$$\ddot{q} = Q_a\ddot{q}_a + Q_p\ddot{q}_p. \quad (2.47)$$

Substituting the above equation in equation (2.46) leads to:

$$\dot{A}(q)\dot{q} + A(q)(Q_a\ddot{q}_a + Q_p\ddot{q}_p) = 0. \quad (2.48)$$

Isolating  $\ddot{q}_p$  in the above equation, one gets:

$$\ddot{q}_p = (A(q)Q_p)^{-1}(-\dot{A}(q)\dot{q} - A(q)Q_a\ddot{q}_a). \quad (2.49)$$

Substituting the above equation in equation (2.46) results in:

$$\ddot{q} = Q_a \ddot{q}_a + Q_p (A(q) Q_p)^{-1} (-\dot{A}(q) \dot{q} - A(q) Q_a \ddot{q}_a). \quad (2.50)$$

Manipulating the above equation and substituting equation (2.43) for  $\dot{q}$ , one gets:

$$\ddot{q} = (Q_a - Q_p (A(q) Q_p)^{-1} A(q) Q_a) \ddot{q}_a - Q_p (A(q) Q_p)^{-1} \dot{A}(q) C(q) \dot{q}_a. \quad (2.51)$$

Comparing the above equation with equation (2.44), one gets:

$$\dot{C}(q) = -Q_p (A(q) Q_p)^{-1} \dot{A}(q) C(q). \quad (2.52)$$

Substituting the above equation in (2.41) results in:

$$C^T(q) H(q) (C(q) \ddot{q}_a + \dot{C}(q) \dot{q}_a) = C^T(q) U - C^T(q) h(q, \dot{q}), \quad (2.53)$$

leading to the inverse dynamics equation:

$$H_a(q) \ddot{q}_a + h_a(q, \dot{q}) = U_a, \quad (2.54)$$

with

$$H_a(q) = C(q)^T H(q) C(q), \quad (2.55)$$

$$h_a(q, \dot{q}) = C^T(q) (H(q) \dot{C}(q) \dot{q}_a + h(q, \dot{q})), \quad (2.56)$$

$$U_a = C^T(q) U. \quad (2.57)$$

## 2.4 Actuator Model

In the previous Sections, it is assumed that the control variable is the torque applied to the parallel mechanism actuated joints. However, in practice there are two motors responsible to convert the control signal computed by the control hardware in torque and applied it to each actuated joint – so, the motors play the role of actuators in the control loop. Therefore, the actual controlled variable becomes the current applied to the actuators.

Assuming that the actuators are DC motors with resultant torque proportional to their armature current, they can be modeled as:

$$\tau = K_t i, \quad (2.58)$$

where  $\tau$  is the electromagnetic torque,  $i$  is the armature current and  $K_t$  is the motor torque constant. Bringing these variables to the previous formulation, the resultant torque  $\tau$  is equivalent to  $U_a$  as it is the control effort applied to the parallel mechanism and the armature current is a new control signal  $U_{FL}$  defined as the output of the feedback linearization loop presented in Chapter 3.

In this case, equation (2.58) can be rewritten in terms of  $U_a$  and  $U_{FL}$  as:

$$U_a = K_t U_{FL}, \quad (2.59)$$

so equation (2.54) becomes:

$$H_a(q)\ddot{q}_a + h_a(q, \dot{q}) = K_t U_{FL}. \quad (2.60)$$

## 3 CONTROL DESIGN

### 3.1 Feedback Linearization

The feedback linearization technique allows one to obtain a linear input-output response from a nonlinear system by defining a new input to algebraically transform the original nonlinear system into a linear one (HAJJAJI; OULADSINE, 2001; SLOTINE; LI, 1991; CRAIG, 2005). Since the parallel mechanism inverse dynamics is completely nonlinear due to the presence of the coupling matrix  $C(q)$  and its derivative, it needs to be linearized. Defining the feedback linearization control signal  $U_{FL}$  in terms of a new control signal  $\bar{U}_{FL}$  given by:

$$U_{FL} = \alpha \bar{U}_{FL} + \beta, \quad (3.1)$$

and substituting it in equation (2.60) results in a new inverse dynamic model given by:

$$H_a(q)\ddot{q}_a + h_a(q, \dot{q}) = K_t(\alpha \bar{U}_{FL} + \beta). \quad (3.2)$$

Defining  $\alpha = \frac{1}{K_t}H_a(q)$ ,  $\beta = \frac{1}{K_t}h_a(q, \dot{q})$  and  $\bar{U}_{FL} = -2\lambda\dot{q}_a - \lambda^2(q_a - U_R)$ , equation (3.2) becomes:

$$\ddot{q}_a + 2\lambda\dot{q}_a + \lambda^2q_a = \lambda^2U_R, \quad (3.3)$$

which corresponds to the dynamic response of a decoupled MIMO second order linear system with transfer function matrix given by:

$$\frac{q_a(s)}{U_R(s)} = \frac{\lambda^2}{(s + \lambda)^2} \times I_2, \quad (3.4)$$

with  $I_2$  as the size 2 identity matrix and  $U_R$  as the robust control signal, the latter being the output of the robust controller proposed in Section 3.2.

It is important to highlight the fact that the linearized system is intentionally computed to not result in a double integrator linear system. The reason is because any

disturbance affecting the nonlinear model could lead to an imperfect linearization, possibly resulting in an unstable system. Moving the poles away from the origin makes the system less susceptible to this issue. The feedback linearization loop is schematized in Figure 3.

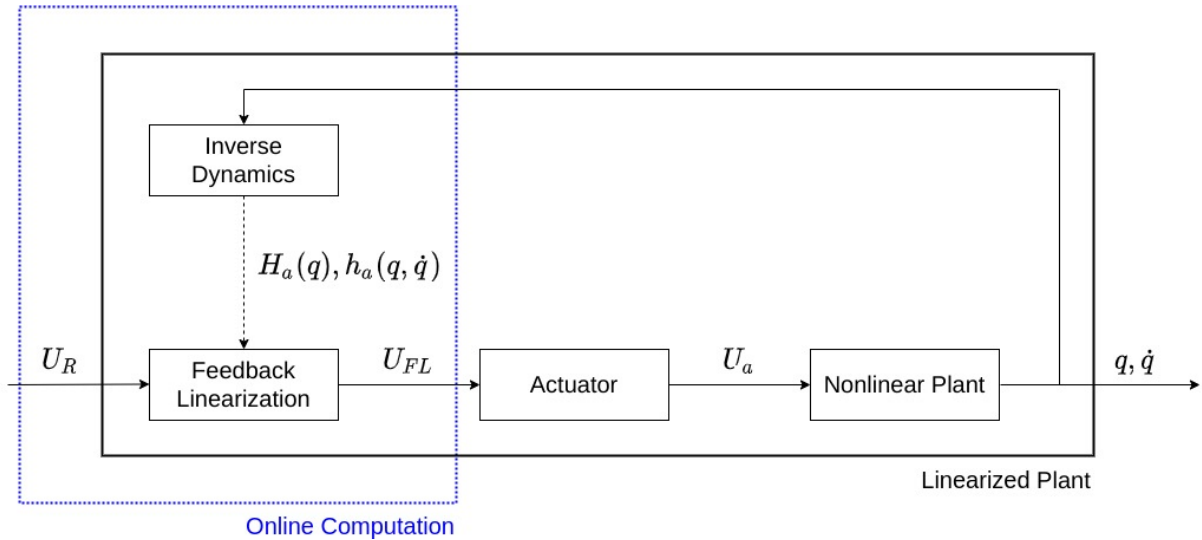


Figure 3: Feedback linearization schematics. Source: the author.

### 3.1.1 Model Matrices Computation Through Feedforward Loop

As pointed out in Hartmann (2018), computing the model matrices in real-time – that is, inside the feedback linearization loop during the system operation – increases the computational effort required to perform the control loop. In order to avoid this, the model matrices could be computed offline using the desired states instead of the actual ones – which means that the model matrices would be computed before the control loop begins to act on the plant. In this case, the feedback linearization loop would change from Figure 3 to Figure 4.

Adopting this strategy prevents the need of a powerful control hardware when implementing the complete system, therefore resulting in a more affordable robotic set. Also, computing the model matrices in advance avoids that possible measurement errors impact these computation. In the works of Coutinho (2020) and Hartmann (2018), this approach is employed as well.

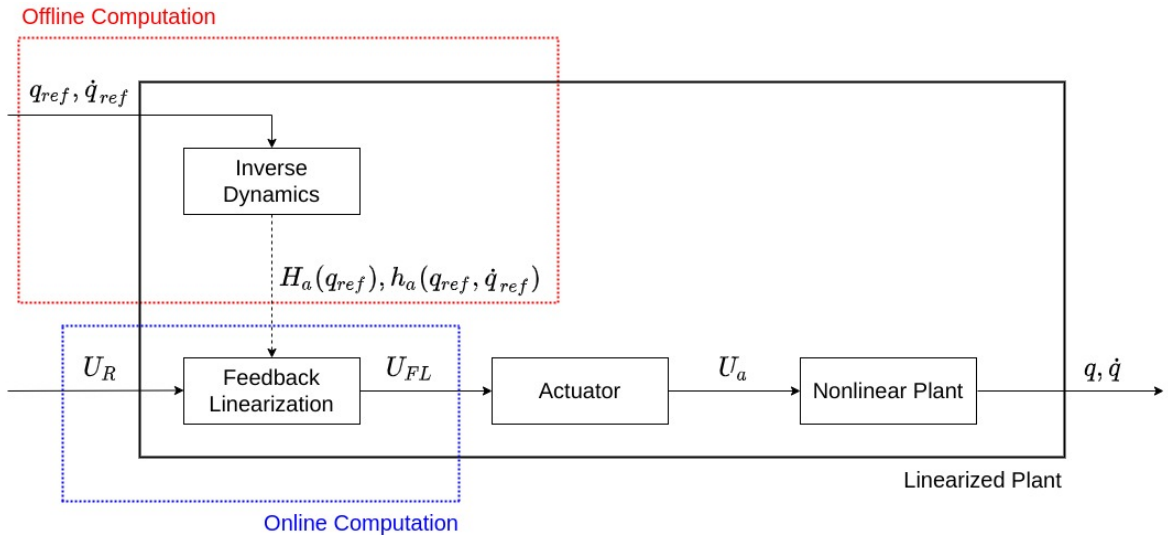


Figure 4: Feedback linearization with feedforward loop for model matrices computation schematics. Source: the author.

## 3.2 $H_\infty$ Control

As shown in Section 3.1, the nonlinear model of the 2-DOF parallel mechanism is transformed into a linear system given by equation (3.4) through the feedback linearization control loop. Atop of that, the original multi-input multi-output (MIMO) system is decoupled, becoming the concatenation of two isolated single-input single-output (SISO) systems given by the same model. For this reason, the following robust control analysis and design can be carried out considering a single SISO system given by:

$$G(s) = \frac{\lambda^2}{(s + \lambda)^2}. \quad (3.5)$$

### 3.2.1 Robust Control Analysis

As stated by Skogestad and Postlethwaite (2007), a robust control system is insensitive to differences between the actual system and the system model considered during control design. Following this definition, the main goal is to design a robust controller capable to guarantee that the closed-loop system satisfies the same control specifications despite possible mismatches between the actual plant and the one considered during control design – the latter also known as nominal plant.

These differences are the so-called model uncertainties, and can be grouped in three categories: parametric uncertainty, where the model structure is known but some parameters are not; neglected and unmodelled dynamics uncertainty, where the model structure

is not entirely known either due to deliberate simplifications or because of a lack of understanding of the physical process; or lumped uncertainty, which comprises one or several uncertainty sources that can be even of different types, all combined into a single representation. For simplicity, the third option is the usual choice since it comprehends the first two.

Different types of uncertainties are best held by different types of controllers. When talking about  $H_\infty$  control, it provides advantages when dealing with unmodelled uncertainty mainly due to its one key point:  $H_\infty$  control design checks if the design specifications are met even for the worst case uncertainty. This approach results in a solid and robust design, although this may lead to conservative results when it is unlikely that the worst case situation will occur. Also, if the uncertainty structure is well known, there are other parametric methods available that can even rely on optimization of some specific aspect of the control response in order to provide more audacious results (OWEN; JAMES, 1992).

When dealing with lumped uncertainty, the frequency domain representation is well suited for describing it since this approach is capable to provide simple yet realistic uncertainty descriptions. Also, a multiplicative structure is usually considered since its numerical value is more informative (SKOGESTAD; POSTLETHWAITE, 2007) when analyzing the capability of the controller to effectively directs the output towards its respective reference value. To explain this, it is considered an uncertain model of the form:

$$G_\Delta(s) = G(s)(1 + w_\Delta(s)\Delta(s)). \quad (3.6)$$

By hypothesis,  $\Delta(s)$  is any stable transfer function that satisfies  $|\Delta(j\omega)| \leq 1, \forall \omega$ . If there is a plant  $G_\Delta(s)$  with  $|w_\Delta(j\omega_0)| \geq 1$  at some specific frequency  $\omega_0$ , then exists a  $|\Delta(j\omega_0)| \leq 1$  such that  $G_\Delta(j\omega_0) = 0$ . This means that at frequency  $\omega_0$ , it does not matter which input value is applied to the plant since it has no effect on the output. So, the magnitude of  $w_\Delta(s)$  can directly provide information regarding the plant controllability. Before analyzing the effects of the uncertainty on system stability and performance, it is important to first address these same aspects about the nominal plant.

### 3.2.1.1 Nominal Stability and Performance

Typically, a feedback control loop is described by the schematics in Figure 5 where  $r(s)$  is the reference input signal,  $y(s)$  is the plant output,  $u(s)$  is the control signal,  $e(s) = r(s) - y(s)$  is the error between the reference and the output,  $d(s)$  is the disturbance

signal,  $n(s)$  is the measurement error and the output and  $K(s)$  and  $G(s)$  are the controller and plant transfer functions, respectively.

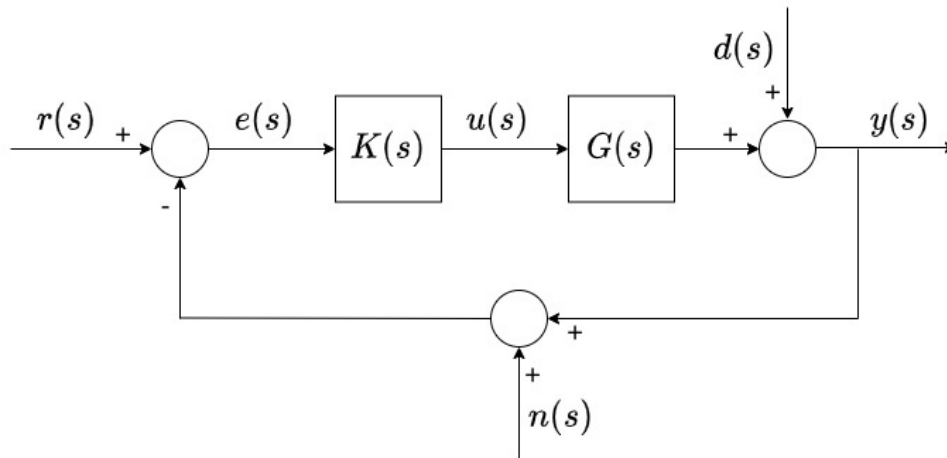


Figure 5: Control loop schematics. Source: the author.

From Figure 5, one can derive that:

$$y(s) = \frac{G(s)K(s)}{1 + G(s)K(s)}r(s) + \frac{1}{1 + G(s)K(s)}d(s) - \frac{G(s)K(s)}{1 + G(s)K(s)}n(s), \quad (3.7)$$

$$e(s) = \frac{1}{1 + G(s)K(s)}r(s) - \frac{1}{1 + G(s)K(s)}d(s) - \frac{1}{1 + G(s)K(s)}n(s). \quad (3.8)$$

Two important relations are the sensitivity and complementary sensitivity functions. The first relates the disturbance  $d(s)$  with the output  $y(s)$  while the second relates the reference input  $r(s)$  with the output  $y(s)$ . So, the sensitivity and complementary sensitivity functions,  $S(s)$  and  $T(s)$  respectively, are given by:

$$S(s) = \frac{1}{1 + L(s)}, \quad (3.9)$$

$$T(s) = \frac{L(s)}{1 + L(s)}, \quad (3.10)$$

where

$$S(s) + T(s) = 1, \quad (3.11)$$

with  $L(s) = G(s)K(s)$  as the open-loop transfer function.

During robust control design, it is typically assumed the stability of the nominal plant. Regarding performance evaluation, different criteria can be used – either on time or frequency domain. For the frequency domain analysis, a typical approach is to analyze the shape of different transfer functions, either in open or closed-loop configuration. For the mixed-sensitivity  $H_\infty$  control design, the closed-loop transfer functions are weighted

in order to achieve the desired system response. Therefore, it is useful to define the performance criteria in terms of the same closed-loop transfer functions.

Following this idea, the sensitivity function  $S(s)$  is a good indicator of closed-loop performance (SKOGESTAD; POSTLETHWAITE, 2007). Typical performance criteria in terms of  $S(s)$  include:

- Minimum bandwidth frequency;
- Maximum tracking error at selected frequencies;
- Maximum steady-state tracking error;
- Shape of  $S(s)$  over selected frequency ranges;
- Maximum peak magnitude of  $S(s)$ .

These specifications can be mathematically captured through an upper bound on the magnitude of  $S(s)$ , that is:

$$|S(j\omega)| < \frac{1}{w_p(j\omega)}, \quad \forall \omega, \quad (3.12)$$

where  $w_p(s)$  is a weight selected by the control designer. Therefore, the following equation represents the nominal performance (NP) condition:

$$|w_p(j\omega)S(j\omega)| < 1, \quad \forall \omega. \quad (3.13)$$

Typically, the performance weight function  $w_p(s)$  is modeled as:

$$w_p(s) = \frac{s/M + \omega_B^*}{s + \omega_B^*A}, \quad (3.14)$$

so  $1/|w_p(j\omega)|$  is equal to  $A \leq 1$  at low frequencies ( $\omega \approx 0$ ) and to  $M \geq 1$  at high ones ( $\omega \gg 1$ ). The parameter  $\omega_B^*$  is approximately the bandwidth requirement.

### 3.2.1.2 Robust Stability and Performance

Ensuring that all possible plants within the family of plants are stable and satisfy the performance requirements means to guarantee robust stability and performance, respectively.

First of all, one needs to define the family of plants model by choosing a suitable representation for the uncertainty regions. As mentioned earlier in this Chapter, the

multiplicative uncertainty is usually considered, leading to a family of plants model given by equation (3.6). To obtain the rational weight  $w_\Delta(j\omega)$ , one typical approach suggested by Skogestad and Postlethwaite (2007) consists in select a nominal model  $G(s)$  and then find the smallest radius  $l_m(\omega)$  which includes all the possible plants  $\Pi$ :

$$l_m(\omega) = \max_{G_\Delta(j\omega) \in \Pi} \left| \frac{G_\Delta(j\omega) - G(j\omega)}{G(j\omega)} \right|. \quad (3.15)$$

The rational weight  $w_\Delta(s)$  must be chosen to cover the set, therefore:

$$|w_\Delta(j\omega)| \geq l_m(\omega), \quad \forall \omega. \quad (3.16)$$

Now, considering the uncertain plant  $G_\Delta(s)$  given by equation (3.6), the open-loop transfer function considering the uncertain plant instead of the nominal one is given by:

$$L_\Delta(s) = G_\Delta(s)K(s) = L(s)(1 + w_\Delta(s)\Delta(s)), \quad \forall \omega, \quad (3.17)$$

and the closed-loop transfer functions – that is, the sensitivity and complementary sensitivity functions – are given by:

$$S_\Delta(s) = \frac{1}{1 + L_\Delta(s)}, \quad (3.18)$$

$$T_\Delta(s) = \frac{L_\Delta(s)}{1 + L_\Delta(s)}, \quad (3.19)$$

As mentioned earlier, the nominal closed-loop system is assumed stable. Also, for simplicity, the uncertain open-loop transfer function  $L_\Delta(s)$  is assumed stable as well. With these assumptions, through the Nyquist stability condition, the nominal open-loop transfer function does not encircle -1. Therefore, as the family of plants is norm-bounded, if there is some plant within the family that encircles -1, then there must be another one that goes exactly through -1 at some frequency (SKOGESTAD; POSTLETHWAITE, 2007). As a consequence, guaranteeing robust stability (RS) means:

$$|1 + L_\Delta(s)| \neq 0, \quad \forall L_\Delta(j\omega), \forall \omega. \quad (3.20)$$

Due to the modulus function, the above equation is equivalent to:

$$|1 + L_\Delta(s)| > 0, \quad \forall L_\Delta(j\omega), \forall \omega, \quad (3.21)$$

which could be rewritten as:

$$|1 + L(s) + w_{\Delta}(s)\Delta(s)L(s)| > 0, \quad \forall \Delta(j\omega), \forall \omega, \quad (3.22)$$

substituting equation (3.17). As pointed out in Skogestad and Postlethwaite (2007), the worst case for the term  $w_{\Delta}(s)\Delta(s)L(s)$  is when  $|\Delta(s)| = 1$  and its phase is such that the terms  $(1 + L)$  and  $w_{\Delta}(s)\Delta(s)L(s)$  point in the opposite direction. Therefore,

$$|1 + L(s) - w_{\Delta}(s)L(s)| > 0, \quad \forall \omega, \quad (3.23)$$

where, applying the reverse triangle inequality, results in:

$$|1 + L(s)| - |w_{\Delta}(s)L(s)| > 0, \quad \forall \omega, \quad (3.24)$$

which could be rewritten as:

$$|w_{\Delta}(s)L(s)| < 1, \quad \forall \omega, \quad (3.25)$$

substituting equation (3.10). The above equation is the robust stability condition.

Now, substituting equation (3.9) in the nominal performance condition from equation (3.13), one gets:

$$|w_p(j\omega)| < |1 + L(j\omega)|, \quad \forall \omega. \quad (3.26)$$

Since  $|1 + L(j\omega)|$  represents, for each frequency  $\omega$ , the distance between  $L(j\omega)$  and the point -1 in the Nyquist plot. Therefore, in order to guarantee nominal performance,  $L(j\omega)$  must be at least a distance of  $|w_p(j\omega)|$  from the point -1.

The robust performance (RP) condition can be obtained applying the same concept from the nominal performance condition to the uncertain model from equation (3.18), resulting in:

$$|w_p(j\omega)S_{\Delta}(j\omega)| < 1, \quad \forall S_{\Delta}(j\omega), \forall \omega, \quad (3.27)$$

which could be rewritten as:

$$|w_p(j\omega)| < |1 + L_{\Delta}(j\omega)|, \quad \forall L_{\Delta}(j\omega), \forall \omega. \quad (3.28)$$

Since the robust performance condition must be satisfied for all possible plants, this includes the worst-case weighted sensitivity function, which means the one with maximum

magnitude:

$$\max_{S_\Delta(j\omega) \in \Pi} |w_p(j\omega)S_\Delta(j\omega)| < 1, \quad \forall \omega. \quad (3.29)$$

Rewriting  $S_\Delta(j\omega)$  in terms of the definition of the open-loop function  $L_\Delta(j\omega)$  given by equation (3.17) results in:

$$S_\Delta(j\omega) = \frac{1}{1 + L(j\omega) + w_\Delta(j\omega)\Delta(j\omega)L(j\omega)}, \quad (3.30)$$

and, as highlighted before, its worst-case scenario is obtained when  $|\Delta(s)| = 1$  and its phase is such that the terms  $(1 + L)$  and  $w_\Delta(s)\Delta(s)L(s)$  point in the opposite direction, thus the worst-case for the sensitivity function  $S_\Delta(j\omega)$  is given by:

$$\max_{S_\Delta(j\omega) \in \Pi} |S_\Delta(j\omega)| = \frac{1}{|1 + L(j\omega)| - |w_\Delta(j\omega)L(j\omega)|} = \frac{|S(j\omega)|}{1 - |w_\Delta(j\omega)T(j\omega)|}, \quad (3.31)$$

and, therefore:

$$\max_{S_\Delta(j\omega) \in \Pi} |w_p(j\omega)S_\Delta(j\omega)| = \frac{|w_p(j\omega)S(j\omega)|}{1 - |w_\Delta(j\omega)T(j\omega)|}. \quad (3.32)$$

Replacing the above equation into equation (3.29) leads to the robustness of performance condition given by:

$$|w_p(j\omega)S(j\omega)| + |w_\Delta(j\omega)T(j\omega)| < 1, \quad \forall \omega. \quad (3.33)$$

As the nominal stability is assumed, the remaining conditions analyzed in this Section – that is, nominal performance and robust stability and performance – can be summarized as follows:

$$\text{NP} \Leftrightarrow |w_p(j\omega)S(j\omega)| < 1, \quad \forall \omega, \quad (3.34)$$

$$\text{RS} \Leftrightarrow |w_\Delta(j\omega)T(j\omega)| < 1, \quad \forall \omega, \quad (3.35)$$

$$\text{RP} \Leftrightarrow |w_p(j\omega)S(j\omega)| + |w_\Delta(j\omega)T(j\omega)| < 1, \quad \forall \omega. \quad (3.36)$$

Therefore, it is clear that, in order to satisfy the robust performance condition, nominal performance and robust stability conditions are prerequisites.

### 3.2.2 $H_\infty$ Control Design

Essentially,  $H_\infty$  control theory relies on the frequency domain analysis to formulate an optimization problem that, once solved, will result in a controller capable of guaranteeing robust stability and performance of the closed-loop system (ZHOU; DOYLE, 1998). Different control design methods based on  $H_\infty$  control theory are available in the literature, but for this work the chosen one was the  $H_\infty$  mixed-sensitivity design. This approach formulates its optimization problem in terms of the  $H_\infty$  norm of the weighted closed-loop transfer functions  $S(s)$  and  $T(s)$ .

In order to do that, first of all, the  $H_\infty$  norm must be defined. So, the  $H_\infty$  norm of a transfer function  $f(s)$  is defined as its maximum value as a function of frequency (SKOGESTAD; POSTLETHWAITE, 2007), which means:

$$\|f(s)\|_\infty \triangleq \max_{\omega} |f(j\omega)|. \quad (3.37)$$

The above definition is valid for SISO systems. For MIMO ones the  $H_\infty$  norm is defined as:

$$\|F(s)\|_\infty \triangleq \max_{\omega} \bar{\sigma}(F(j\omega)), \quad (3.38)$$

where  $F(s)$  is a transfer function matrix and  $\bar{\sigma}$  is the upper singular value function.

For MIMO systems, the robustness of stability and performance conditions use the concept of structured singular values (SSV). As the feedback linearization technique decouple the MIMO system in a set of SISO systems, the SISO theory is enough for this work. Thus, the stability and performance conditions from equations (3.34), (3.35) and (3.36) can be rewritten in terms of the  $H_\infty$  norm as:

$$\text{NP} \Leftrightarrow \|w_p(s)S(s)\|_\infty < 1, \quad (3.39)$$

$$\text{RS} \Leftrightarrow \|w_\Delta(s)T(s)\|_\infty < 1, \quad (3.40)$$

$$\text{RP} \Leftrightarrow \|w_p(s)S(s)\|_\infty + \|w_\Delta(s)T(s)\|_\infty < 1. \quad (3.41)$$

Now that the robust stability and performance conditions are in terms of their  $H_\infty$  norm, the  $H_\infty$  control problem can be formulated. In  $H_\infty$  control design, the standard problem formulation (SKOGESTAD; POSTLETHWAITE, 2007) is presented in Figure 6.

This system is mathematically described by:

$$\begin{bmatrix} z \\ v \end{bmatrix} = P(s) \begin{bmatrix} w \\ u \end{bmatrix} = \begin{bmatrix} P_{11}(s) & P_{12}(s) \\ P_{21}(s) & P_{22}(s) \end{bmatrix} \begin{bmatrix} w \\ u \end{bmatrix}, \quad (3.42)$$

with the state-space realization of  $P(s)$  given by:

$$P(s) \stackrel{s}{=} \left[ \begin{array}{c|cc} A & B_1 & B_2 \\ \hline C_1 & D_{11} & D_{12} \\ C_2 & D_{21} & D_{22} \end{array} \right], \quad (3.43)$$

where  $u(s)$  represents the control variables,  $v(s)$  the measured variables,  $w(s)$  the external signals such as disturbances or reference commands, and  $z(s)$  the so-called "error" signals that should be minimized in some way in order to achieve the desired control characteristics.

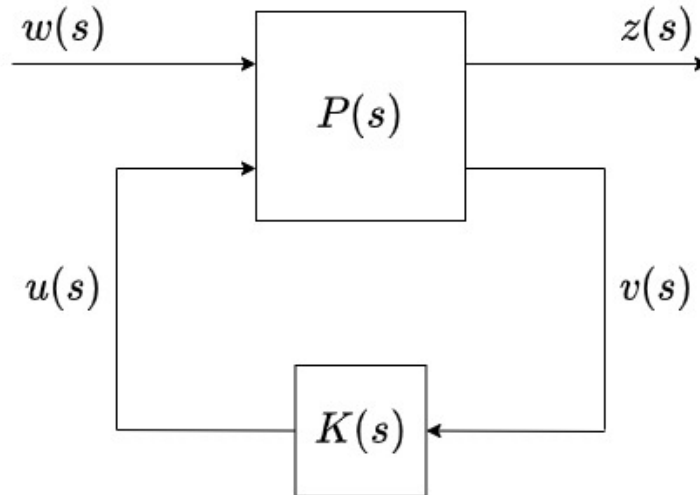


Figure 6: Standard control configuration. Source: the author.

From Figure 6, it is possible to obtain the closed-loop transfer function between  $z(s)$  and  $w(s)$  in the form of a lower fractional transformation given by:

$$z(s) = F_l(P(s), K(s))w(s), \quad (3.44)$$

with

$$F_l(P(s), K(s)) = P_{11}(s) + P_{12}K(I - P_{22}K(s))^{-1}P_{21}(s). \quad (3.45)$$

Essentially, the  $H_\infty$  optimal controller is obtained minimizing the  $H_\infty$  norm of  $F_l(P(s), K(s))$ , that is  $\|F_l(P(s), K(s))\|_\infty$ . In practice,  $H_\infty$  algorithms find a sub-optimal

controller since finding an optimal one is numerically and theoretically complicated (SKOGSTAD; POSTLETHWAITE, 2007).

This means that, with  $\gamma_{min}$  as the minimum value of  $\|F_l(P(s), K(s))\|_\infty$  over all stabilizing controllers  $K(s)$ , the  $H_\infty$  sub-optimal control problem consists in, for a given  $\gamma > \gamma_{min}$ , find all stabilizing controllers  $K(s)$  such that:

$$\|F_l(P(s), K(s))\|_\infty < \gamma. \quad (3.46)$$

This sub-optimal problem can be solved through the iterative algorithm proposed by Doyle et al. (1988). Following Skogestad and Postlethwaite (2007), the algorithm can be summarized as follows: for the standard problem formulation from Figure 6, there exists a stabilizing controller  $K(s)$  such that  $\|F_l(P(s), K(s))\|_\infty < \gamma$  if and only if

1.  $X_\infty \geq 0$  is a solution of the algebraic Riccati equation:

$$A^T X_\infty + X_\infty A + C_1^T C_1 + X_\infty (\gamma^{-2} B_1 B_1^T - B_2 B_2^T) X_\infty = 0, \quad (3.47)$$

with  $Re \lambda_i[A + (\gamma^{-2} B_1 B_1^T - B_2 B_2^T) X_\infty] < 0, \forall i$ , and

2.  $Y_\infty \geq 0$  is a solution of the algebraic Riccati equation:

$$A Y_\infty + X_\infty A^T + B_1 B_1^T + Y_\infty (\gamma^{-2} C_1^T C_1 - C_2^T C_2) Y_\infty = 0, \quad (3.48)$$

with  $Re \lambda_i[A + Y_\infty (\gamma^{-2} C_1^T C_1 - C_2^T C_2)] < 0, \forall i$ , and

- 3.

$$\rho(X_\infty Y_\infty) < \gamma^2. \quad (3.49)$$

All possible controllers are given by the linear fractional transformation  $K(s) = F_l(K_c(s), Q(s))$  where  $K_c(s)$  has its state-space realization given by:

$$K_c(s) \stackrel{s}{=} \left[ \begin{array}{c|cc} A_\infty & -Z_\infty L_\infty & Z_\infty B_2 \\ \hline F_\infty & 0 & I \\ -C_2 & I & 0 \end{array} \right], \quad (3.50)$$

with

$$F_\infty = -B_2^T X_\infty, \quad (3.51)$$

$$L_\infty = -Y_\infty C_2^T, \quad (3.52)$$

$$Z_\infty = (I - \gamma^{-2} Y_\infty X_\infty)^{-1}, \quad (3.53)$$

$$A_\infty = A + \gamma^{-2} B_1 B_1^T X_\infty + B_2 F_\infty + Z_\infty L_\infty C_2, \quad (3.54)$$

and  $Q(s)$  any stable proper transfer function such that  $\|Q(s)\|_\infty < \gamma$ .

In order to approach  $\gamma_{min}$ ,  $\gamma$  is iteratively reduced towards  $\gamma_{min}$  until the defined tolerance is achieved. Yet, to apply the algorithm,  $P(s)$  must be defined to reflect the control problem – specially its control specifications. With this purpose, the mixed-sensitivity method is applied.

### 3.2.2.1 Mixed-sensitivity Method

The mixed-sensitivity method consists in shaping the sensitivity function  $S(s)$  along with one or more closed-loop transfer functions, such as  $K(s)S(s)$  or  $T(s)$  (SKOGESTAD; POSTLETHWAITE, 2007). Since the multiplicative uncertainty is being considered (see equation (3.6)), it is desirable to be able to shape  $T(s)$  in order to achieve robust stability. Also, shaping  $K(s)S(s)$  is important for limiting the size and bandwidth of the controller, thus the control energy used. On top of that, it is typically assumed that the measurement error is negligible.

Therefore, to encompass the cases highlighted above, the chosen cost function is given by:

$$\left\| \left[ \begin{array}{c} W_1(s)S(s) \\ W_2(s)K(s)S(s) \\ W_3(s)T(s) \end{array} \right] \right\|_\infty, \quad (3.55)$$

which corresponds to the control configuration presented in Figure 7.

From Figure 7, the generalized plant  $P(s)$  elements from equation (3.42) are given by:

$$P_{11} = \begin{bmatrix} W_1(s) \\ 0 \\ 0 \end{bmatrix}, \quad P_{12} = \begin{bmatrix} -W_1(s)G(s) \\ W_2(s) \\ W_3(s)G(s) \end{bmatrix}, \quad P_{21} = 1, \quad P_{22} = -G(s). \quad (3.56)$$

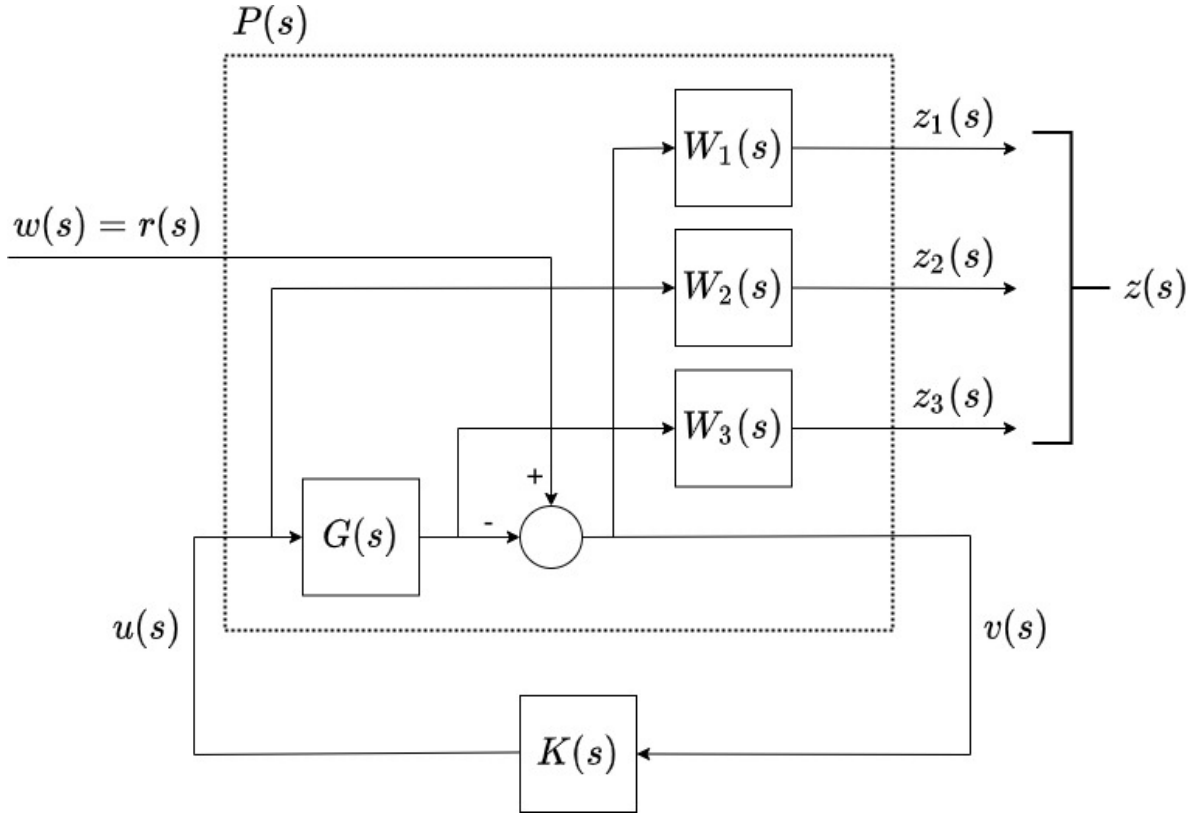


Figure 7:  $S/KS/T$  Mixed-sensitivity control configuration. Source: the author.

After the designer has chosen the weighted functions  $W_1(s)$ ,  $W_2(s)$  and  $W_3(s)$ , the sub-optimal  $H_\infty$  controller can be computed through the algorithm proposed by Doyle et al. (1988) and the robust stability and performance conditions can be checked. If the conditions are not satisfied, new weighted functions are evaluated until they lead to a satisfying  $H_\infty$  controller.

Once the  $H_\infty$  robust controller is obtained, it is combined with the feedback linearization loop to close the complete control loop as shown in Figure 8.

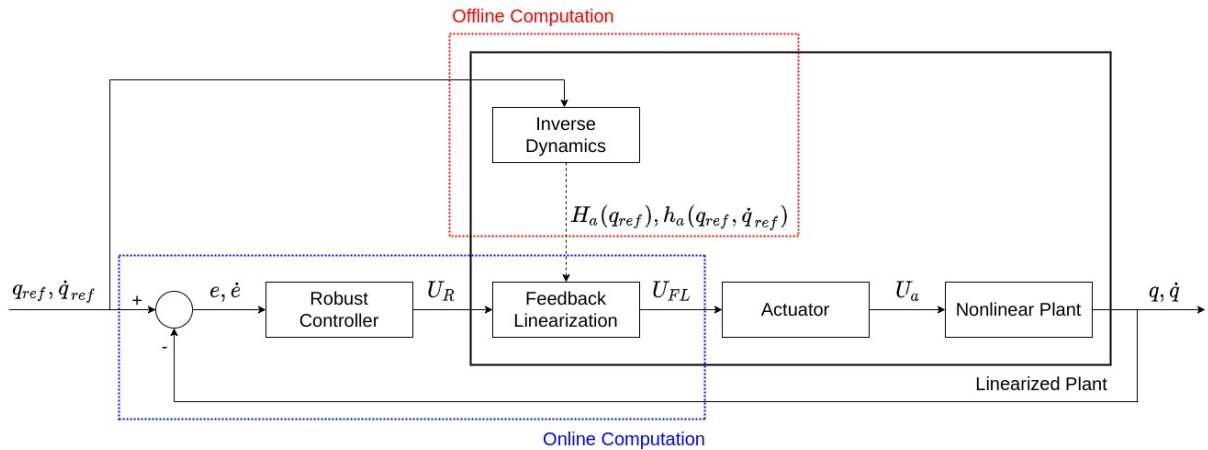


Figure 8: Control closed-loop. Source: the author.

## 4 RESULTS AND DISCUSSION

### 4.1 Preliminary Results For Desing Proposal Validation

Before applying the robust control design proposed on Chapter 3 to the 2-DOF parallel mechanism, the approach was first validated through the 3-DOF spacial serial mechanism presented in Figure 9 which results were published in the XXII Brazilian Conference on Automation (STEVANI et al., 2018).

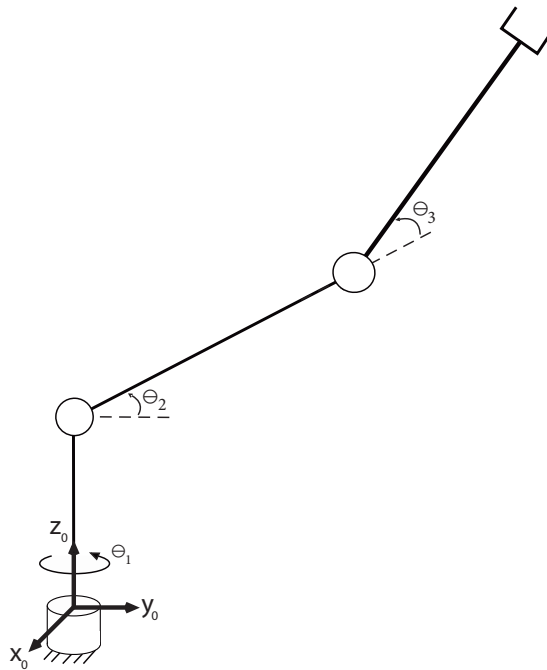


Figure 9: RRR spatial serial mechanism. Source: the author.

As explained in Chapter 2, the dynamic model of a serial mechanism can be written as:

$$M(q)\ddot{q} + V(q, \dot{q}) + G(q) = \tau, \quad (4.1)$$

where  $M(q)$  is the inertia matrix,  $V(q, \dot{q})$  is the vector of centrifugal and Coriolis terms,  $G(q)$  is the vector of gravitational forces,  $q$  is a column-matrix of independent generalized coordinates, whose entries are relative displacements of the joints, and  $\tau$  is a column-matrix of the generalized actuators' efforts in the directions of the independent quasi-velocities  $\dot{q}$  (COUTINHO; COELHO, 2016; DOBRIANSKYJ; COUTINHO; HESS-COELHO, 2014; CRAIG, 2005).

To obtain the dynamic model of a 3-DOF RRR spatial serial mechanism (Fig. 9), the Lagrangian formalism was applied (LANCZOS, 2012) using the Denavit-Hatemberg parameters described in Table 1. The resultant dynamic model is given by:

$$M(q) = \begin{bmatrix} D_{11} & D_{12} & D_{13} \\ D_{12} & D_{22} & D_{23} \\ D_{13} & D_{23} & D_{33} \end{bmatrix}, \quad (4.2)$$

$$V(q, \dot{q}) = \begin{bmatrix} D_{111} & D_{122} & D_{133} \\ D_{211} & D_{222} & D_{233} \\ D_{311} & D_{322} & D_{333} \end{bmatrix} \begin{bmatrix} \dot{q}_1^2 \\ \dot{q}_2^2 \\ \dot{q}_3^2 \end{bmatrix} + \quad (4.3)$$

$$2 \begin{bmatrix} D_{112} & D_{113} & D_{123} \\ D_{212} & D_{213} & D_{223} \\ D_{312} & D_{313} & D_{323} \end{bmatrix} \begin{bmatrix} \dot{q}_1 \dot{q}_2 \\ \dot{q}_1 \dot{q}_3 \\ \dot{q}_2 \dot{q}_3 \end{bmatrix},$$

$$G(q) = \begin{bmatrix} D_1 & D_2 & D_3 \end{bmatrix}^T, \quad (4.4)$$

$$q = \begin{bmatrix} q_1 & q_2 & q_3 \end{bmatrix}^T, \quad (4.5)$$

$$\tau = \begin{bmatrix} \tau_1 & \tau_2 & \tau_3 \end{bmatrix}^T, \quad (4.6)$$

with its coefficients given in terms of the vector  $q$ , the mass  $m_i$  of the  $i^{th}$  rigid body of the mechanical system,  $l_i$  and  $l_{qi}$  whereas the first is the  $i^{th}$  link length and the second is the distance from the beginning of the  $i^{th}$  link to its center of mass, and the principal moments of inertia  $J_{x_i}, J_{y_i}, J_{z_i}$  of the  $i^{th}$  mechanical system's rigid body in relation of its center of mass:

$$\begin{aligned}
D_1 &= 0, \\
D_2 &= m_2 l_{g2} \cos(q_2) + m_3 (l_2 \cos(q_2)) + \\
& l_{g3} \cos(q_2 + q_3), \\
D_3 &= m_3 l_{g3} \cos(q_2 + q_3), \\
D_{11} &= J_{x_2} \sin^2(q_2) + J_{x_3} \sin^2(q_2 + q_3) + J_{y_1} + \\
& J_{y_3} \cos^2(q_2 + q_3) + (J_{y_2} + m_2 l_{g2}^2) \cos^2(q_2) + \\
& m_3 (l_2 \cos(q_2) + l_{g3} \cos(q_2 + q_3))^2, \\
D_{22} &= J_{z_2} + J_{z_3} + m_2 l_{g2}^2 + \\
& m_3 (l_2^2 + 2l_2 l_{g3} \cos(q_3) + l_{g3}^2), \\
D_{33} &= J_{z_3} + m_3 l_{g3}^2, \\
D_{12} &= D_{13} = 0, \\
D_{23} &= J_{z_3} + m_3 l_{g3} (l_2 \cos(q_3) + l_{g3}), \\
D_{111} &= D_{122} = D_{133} = 0, \\
D_{112} &= \frac{1}{2} \sin(2(q_2 + q_3)) (J_{x_3} - J_{y_3}) + \\
& \sin(2q_2) (J_{x_2} - J_{y_2} - m_2 l_{g2}^2) - 2m_3 (l_2 \cos(q_2) + \\
& l_{g3} \cos(q_2 + q_3)) (l_2 \sin(q_2) + l_{g3} \sin(q_2 + q_3)), \\
D_{113} &= \sin(q_2 + q_3) (-m_3 l_2 l_{g3} \cos(q_2) + \\
& (J_{x_3} - J_{y_3} - m_3 l_{g3}^2) \cos(q_2 + q_3)), \\
D_{123}, D_{222}, D_{212}, D_{213} &= 0, \\
D_{211} &= \frac{1}{2} (-J_{x_2} \sin(2q_2)) + (J_{y_2} + m_2 l_{g2}^2) \sin(2q_2) + \\
& m_3 (\sin(2q_2)) l_2^2 + 2l_2 l_{g3} \sin(2q_2 + q_3) + \\
& (-J_{x_3} + J_{y_3} + m_3 l_{g3}^2) \sin(2q_2), \\
D_{233} &= -m_3 l_2 l_{g3} \sin(q_3), \\
D_{311} &= (m_3 l_2 l_{g3} \cos(q_2) + \\
& (-J_{x_3} + J_{y_3} + m_3 l_{g3}^2) \cos(q_2 + q_3)) \sin(q_2 + q_3), \\
D_{322} &= m_3 l_2 l_{g3} \sin(q_3), \\
D_{333} &= 0, \\
D_{312} &= D_{313} = D_{323} = 0.
\end{aligned} \tag{4.7}$$

Applying the feedback linearization explained in Chapter 3, the 3-DOF spacial serial

Table 1: Denavit-Hatenberg parameters for the RRR spatial serial mechanism.

$i$	$a_i$	$\alpha_i$	$d_i$	$\theta_i$
1	0	$\pi/2$	$l_1$	$\theta_1$
2	$l_2$	0	0	$\theta_2$
3	$l_3$	0	0	$\theta_3$

mechanism dynamic model becomes a second order linear system with transfer function matrix given by:

$$\frac{q(s)}{\hat{\tau}(s)} = \frac{\lambda^2}{(s + \lambda)^2} \times I_3, \quad (4.8)$$

with  $I_3$  as the third order identity matrix.

Now, as can be seen in Stevani et al. (2018), the method chosen for the  $H_\infty$  control design was the loop-shaping. The main difference between this methodology and the mixed-sensitivity is that the first one relies on open-loop transfer functions, while the second considers closed-loop transfer functions in the robust analysis. Also, the loop-shaping uses a graphic analysis through robust stability and performance barriers while the mixed-sensitivity evaluate the robust stability and performance conditions by means of weight functions. Yet, both methods lead to  $H_\infty$  controllers. For more details regarding the proposed loop-shaping design refer to Stevani et al. (2018).

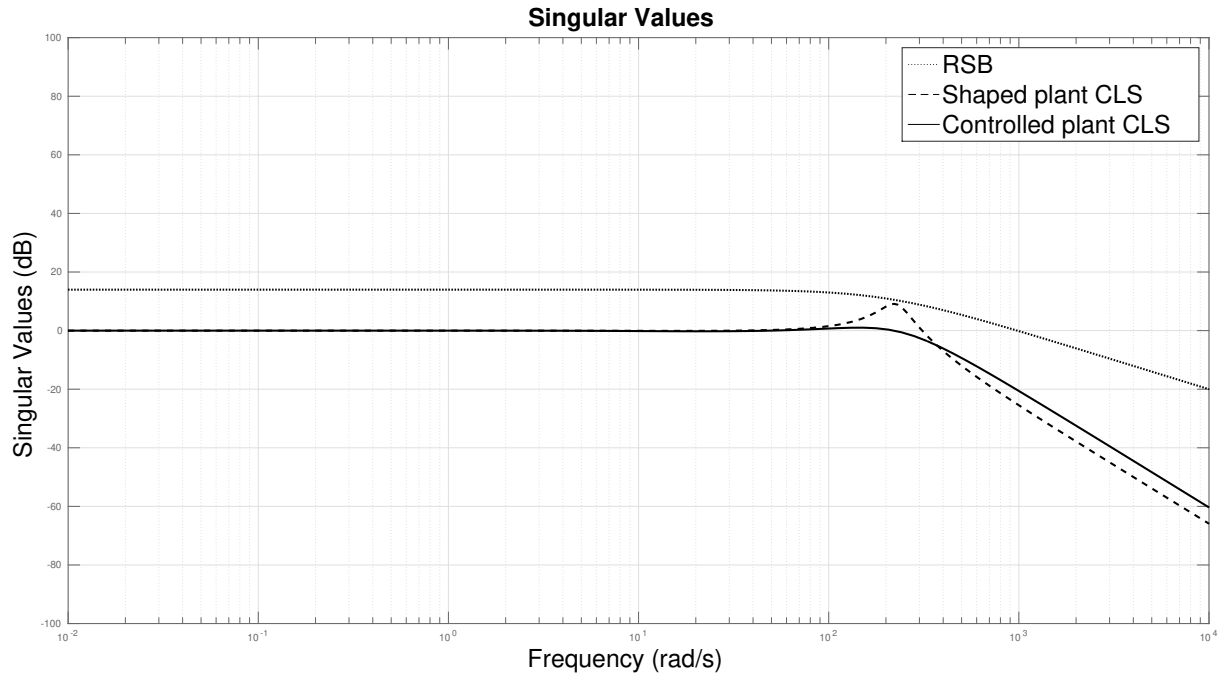
The  $H_\infty$  controller  $K(s) = \hat{\tau}(s)/r(s)$  – where  $r(s)$  regards the reference signal – obtained through the loop-shaping method is given by:

$$K(s) = \frac{47.40(s + 134.75)(s + 12.17)}{(s + 513.37)(s + 0.19)} \times I_3. \quad (4.9)$$

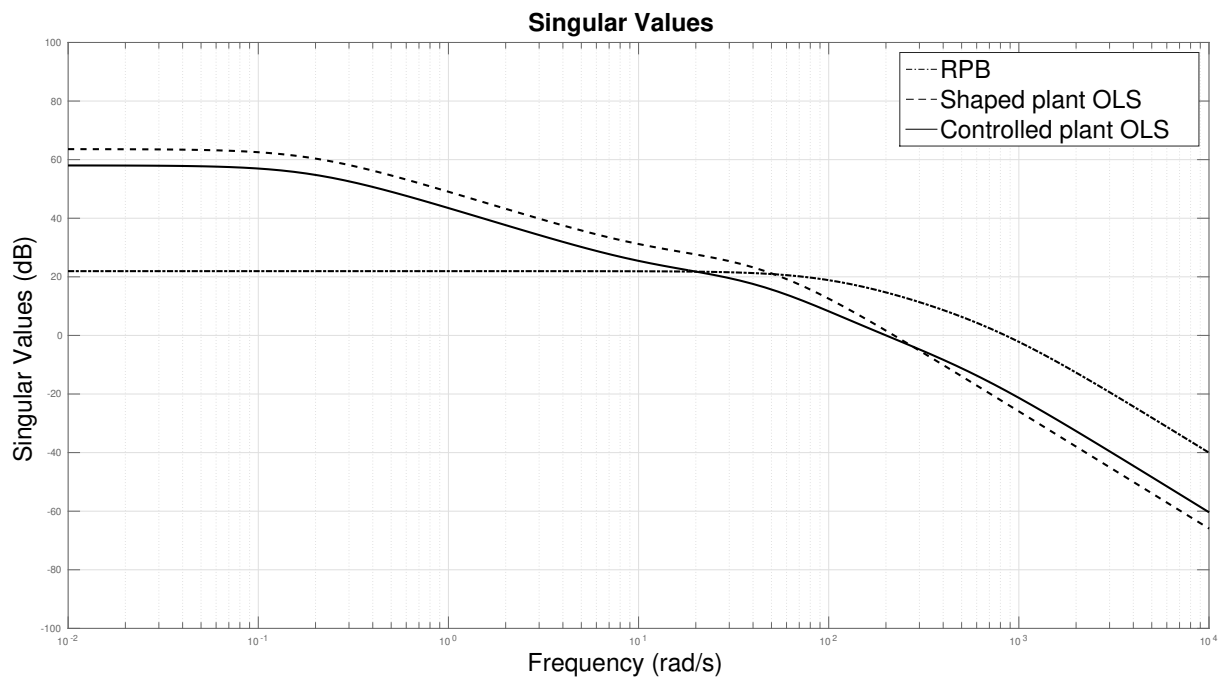
Analyzing the robust stability and performance barriers shown in Figure 10, one concludes that the  $H_\infty$  controller satisfies the robust stability and performance criteria.

To support the theoretical results presented in this Section, time-domain simulations with sinusoidal inputs were performed in the MATLAB/Simulink environment. The model parameters are shown in Table 2. For the gravity, the standard value  $g = 9.8 \text{ m/s}^2$  was adopted.

A feedback linearization (FL) control with  $\lambda = 100 \text{ rad/s}$  was also implemented for performance comparison. The nominal system open loop model considering only the



(a) Robust stability barrier (RSB) and shaped and controlled plants closed-loop system (CLS) response.



(b) Robust performance barrier (RPB) and shaped and controlled plants open-loop system (OLS) response.

Figure 10: Robustness analysis. Source: the author.

feedback linearization control is then given by:

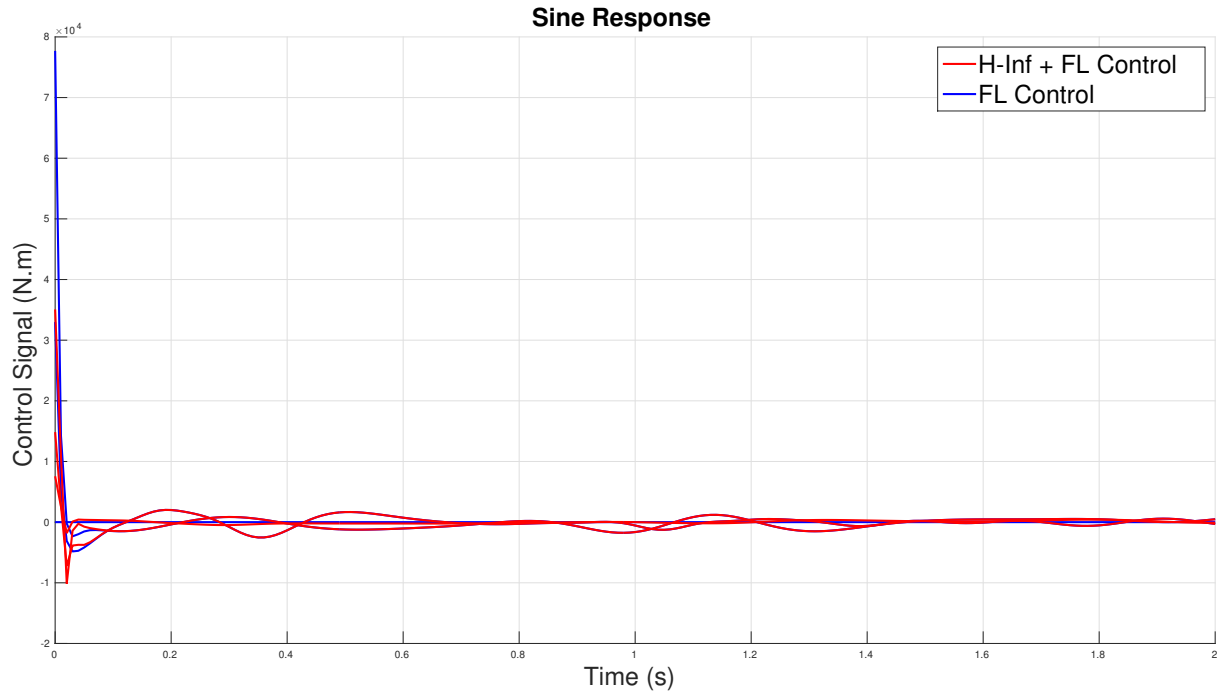
$$\frac{q(s)}{r(s)} = \frac{\lambda^2}{(s + \lambda)^2}. \quad (4.10)$$

Feed forward terms were added in both control laws.

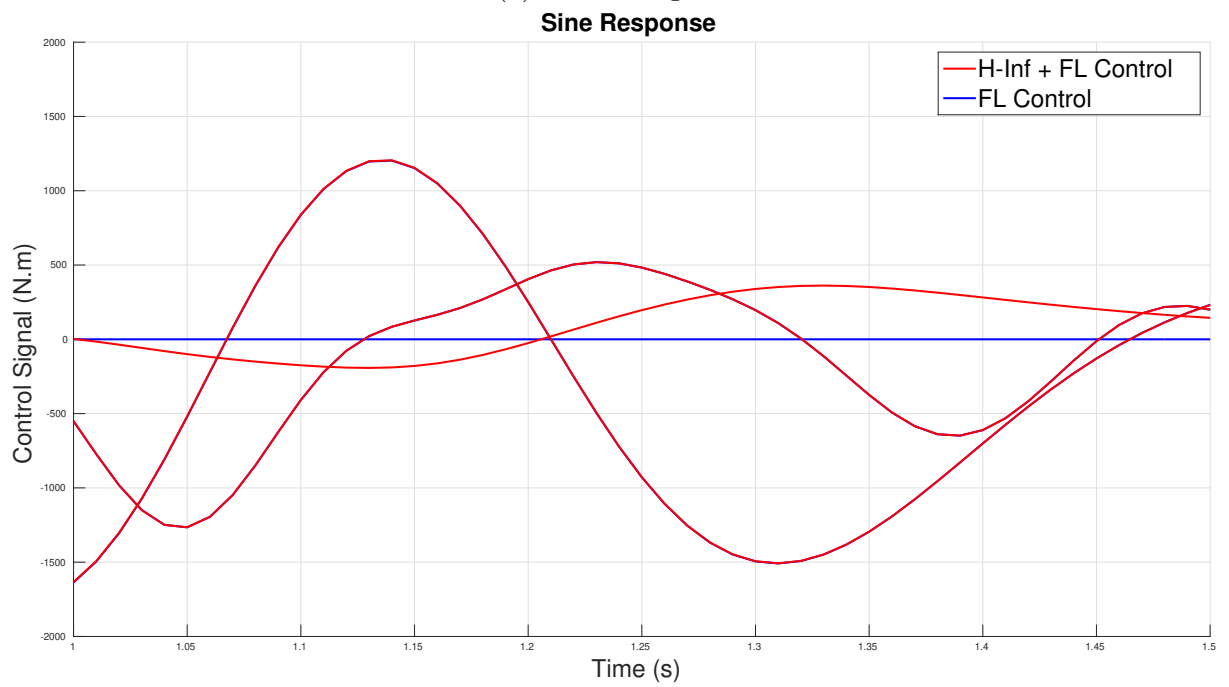
Table 2: 3-DOF RRR spatial serial mechanism nominal parameters.

Parameter	Value
$m_1$	20 [kg]
$m_2$	20 [kg]
$m_3$	5 [kg]
$l_1$	1 [m]
$l_2$	1 [m]
$l_3$	1 [m]
$l_{g1}$	0.75 [m]
$l_{g2}$	0.75 [m]
$l_{g3}$	0.5 [m]
$J_{x1}$	1.6667 [kg.m <sup>2</sup> ]
$J_{y1}$	1.6667 [kg.m <sup>2</sup> ]
$J_{z1}$	0 [kg.m <sup>2</sup> ]
$J_{x2}$	0 [kg.m <sup>2</sup> ]
$J_{y2}$	1.6667 [kg.m <sup>2</sup> ]
$J_{z2}$	1.6667 [kg.m <sup>2</sup> ]
$J_{x3}$	0 [kg.m <sup>2</sup> ]
$J_{y3}$	0.4167 [kg.m <sup>2</sup> ]
$J_{z3}$	0.4167 [kg.m <sup>2</sup> ]

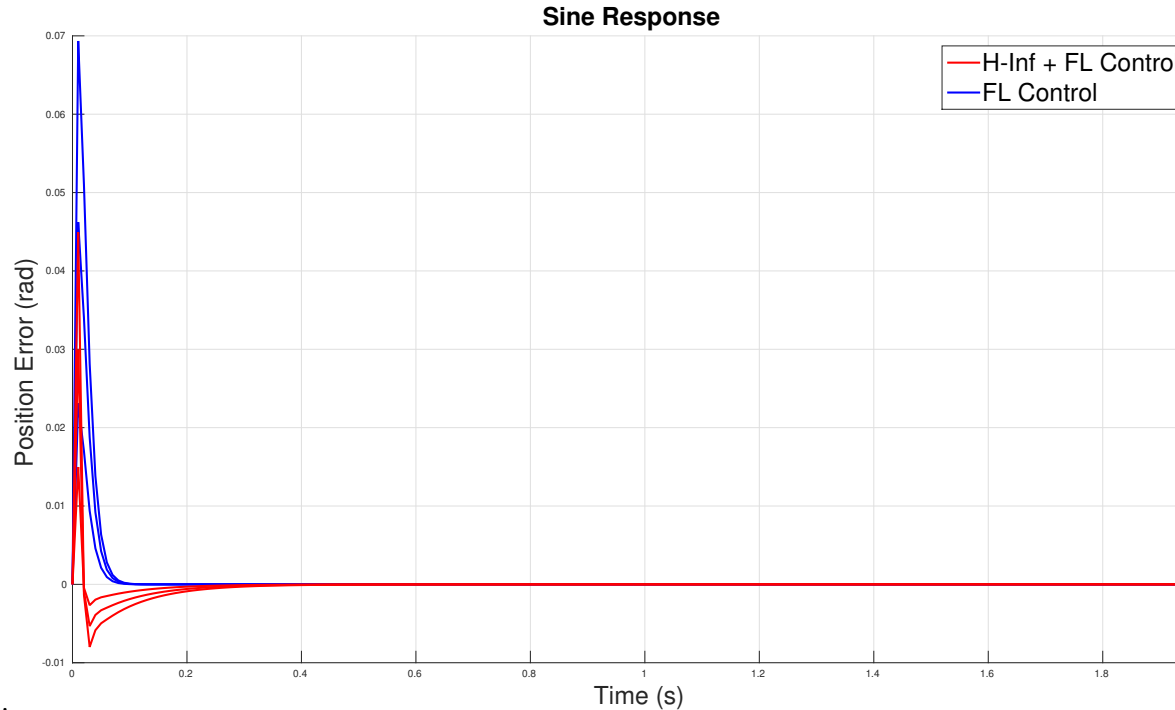
The first simulation considered the robot nominal parameters – that is, the exact values presented in Table 2 – and the results are shown in Fig. 11. Figs. 11(a) and 11(b) show that the  $H_\infty$ /feedback linearization combination and the FL technique only led almost to exact the same control signals with the exception of one component that the FL technique presented smaller values. In Fig. 11(c), the errors for a sinusoidal input are shown, concluding that the  $H_\infty$ /feedback linearization combination and the feedback linearization control provided equivalent results regarding the nominal model.



(a) Control signal.



(b) Zoomed image of the control signal.



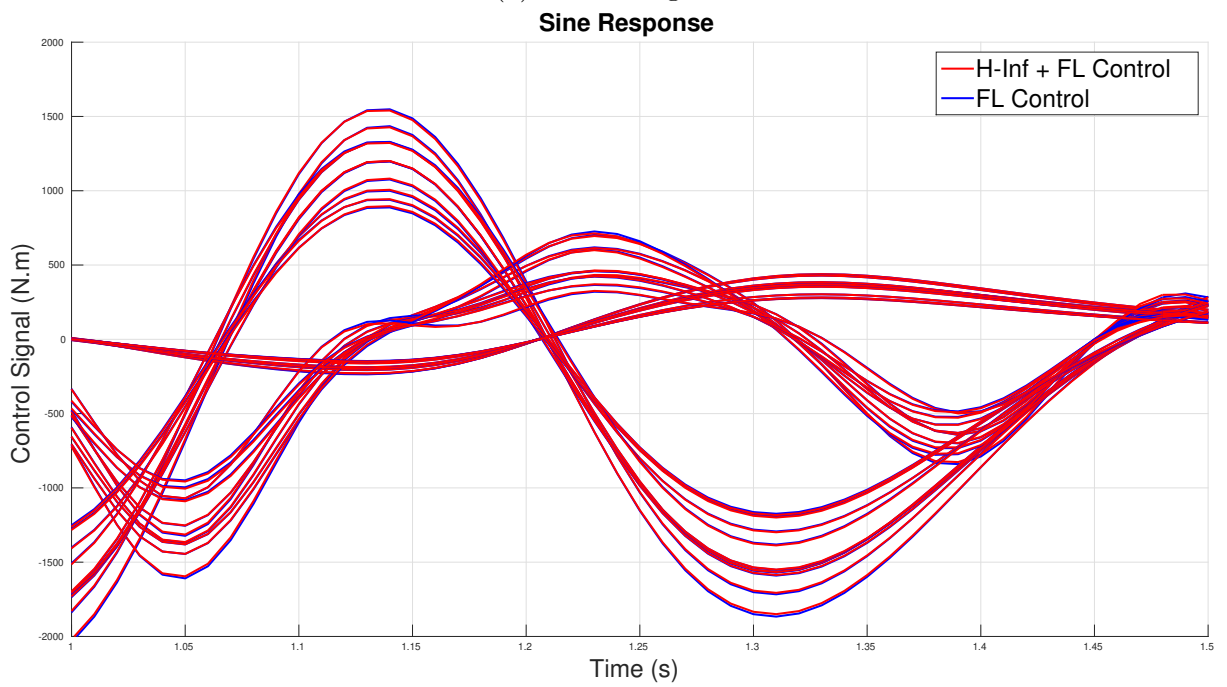
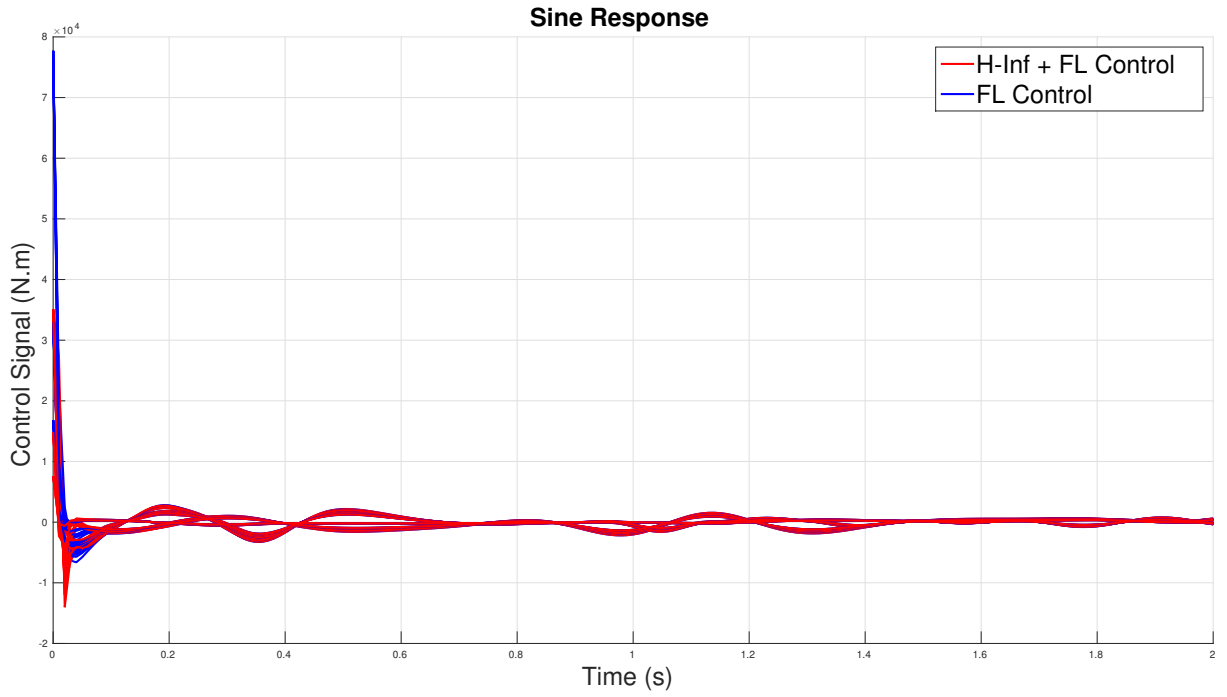
Position error.

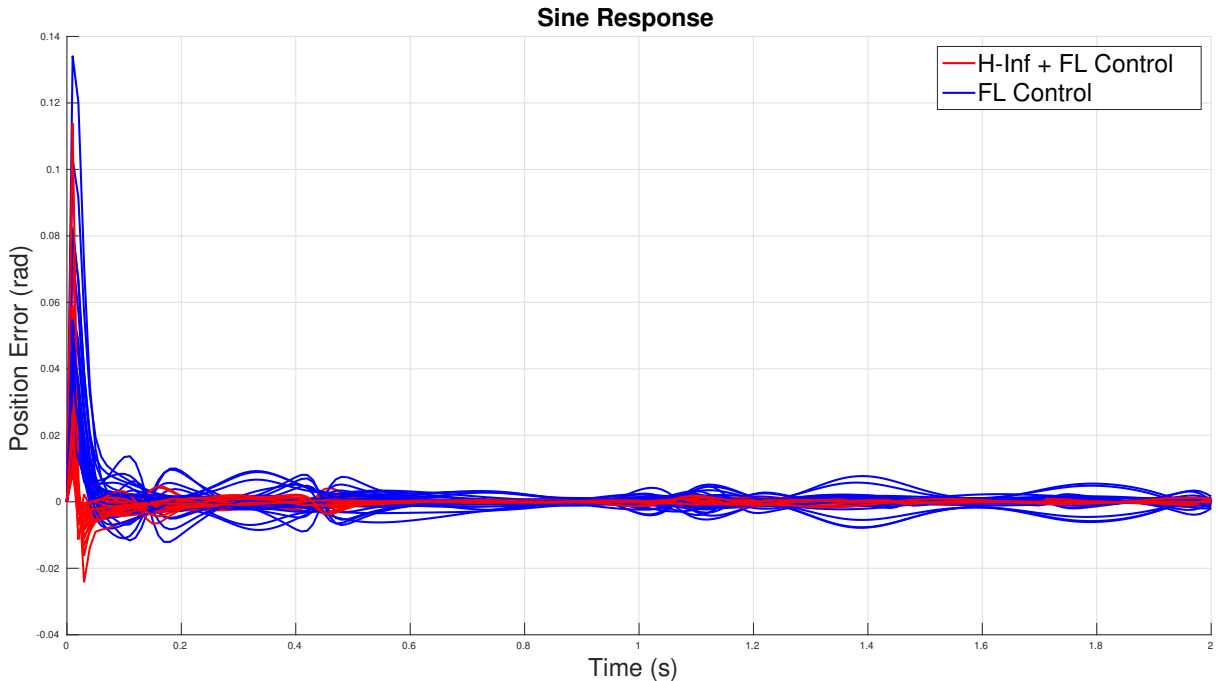
(d)

(e)

Figure 11: Nominal model response for sinusoidal input. Source: the author.

To perform the second simulation, 10 uncertain samples were considered for the robot model parameters from Table 2 within a 20% tolerance for the inertia parameters and a 5% tolerance for the link lengths, since the last ones could be precisely measured. The results are shown in Fig. 12. As in the nominal case simulation, in Figs. 12(a) and 12(b) the control signals of the  $H_\infty$ /feedback linearization combination and the FL technique only are very similar too, but now it was the  $H_\infty$ /feedback linearization combination that led to slightly smaller values. Fig. 12(c) show that, in the presence of remaining nonlinear dynamics, the  $H_\infty$ /feedback linearization combination led to almost a ten times better performance than only the feedback linearization control. This result was achieved due only to the  $H_\infty$ /feedback linearization combination robustness, since no significant increase in the control signal was observed – as a matter of fact, the  $H_\infty$ /feedback linearization combination control signals were slightly smaller than only the feedback linearization control ones.





(c) Position error.

Figure 12: Uncertain model response for sinusoidal input. Source: the author.

With the proposed robust control design validated for the serial mechanism, it was time to apply it to the parallel one.

## 4.2 Parallel Model

### 4.2.1 Nominal Parameters

The parallel mechanism was first simulated considering its nominal parameters presented in Table 3. The gravitational acceleration is defined as  $g = 9.81 \text{ m/s}^2$  and the motor torque constant is defined as  $K_t = 0.05632 \text{ N.m/A}$  for all simulations performed on this study.

The motor torque constant and the parallel mechanism nominal parameters were retrieved from Coutinho (2020).

### 4.2.2 Uncertain Parameters

As explained in Section 3.1, the real mechanism could present parameters different from the nominal ones (see Table 3), inevitably leading to different responses in comparison to the nominal case. In order to verify this scenario, a set of different parameters

Table 3: 2-DOF parallel mechanism nominal parameters.

Parameter	Value
$m_1$ [kg]	0.0620
$m_2$ [kg]	0.1105
$l_0$ [m]	0.0500
$l_1$ [m]	0.1200
$l_2$ [m]	0.1600
$l_{g1}$ [m]	0.0600
$l_{g2}$ [m]	0.0680
$J_{z1}$ [kg.m <sup>2</sup> ]	0.00027510
$J_{z2}$ [kg.m <sup>2</sup> ]	0.00045380

samples needs to be produced. Instead of choosing it randomly, the latin hypercube sampling technique was used to generate this set. The LHS provides a more complete coverage of the sample space because each sample is chosen considering the total number of samples, so the resultant set is more uniformly distributed throughout the sample space (HELTON; DAVIS; JOHNSON, 2005; HELTON; DAVIS, 2002), as can be seen in Figure 13. Essentially, for a set of parameters with  $n$  variables, the LHS divides the range of each variable into  $m$  equally probable intervals. Then,  $m$  sample points are placed to satisfy the Latin hypercube criteria, which is defined as follows: a sample set is a Latin hypercube if, and only if, each sample is the only one in each axis-aligned hyperplane containing it (Figure 14). This means that the number of samples does not depend on the number of variables, which could be really helpful when dealing with complex systems (STEIN, 1987).

Then, two main issues of using random sampling to generate the parameters set were solved by opting for LHS instead: generating different samples randomly would not have any guarantee that the output set is actually distributed along the sample space; also, generating a combination of  $m$  different sample points for  $n$  variables would result in a set of  $n^m$  values that could escalate exponentially in size when combining a high number of parameters, becoming impracticable to simulate all cases (MANTEUFEL, 2000).

The parameters were generated considering a 10% tolerance for inertial parameters (masses and moments of inertia) and a 5% tolerance for the bar lengths since the latter can be more precisely measured. A total of 12 samples were generated: the first 10 computed through LHS MATLAB built-in function *lhsdesign* (MATHWORKS, 2020b) and the last 2 considering the positive and negative tolerance boundaries, respectively. The set is presented on Table 4, sample 0 considering the nominal parameters from Table 3 for

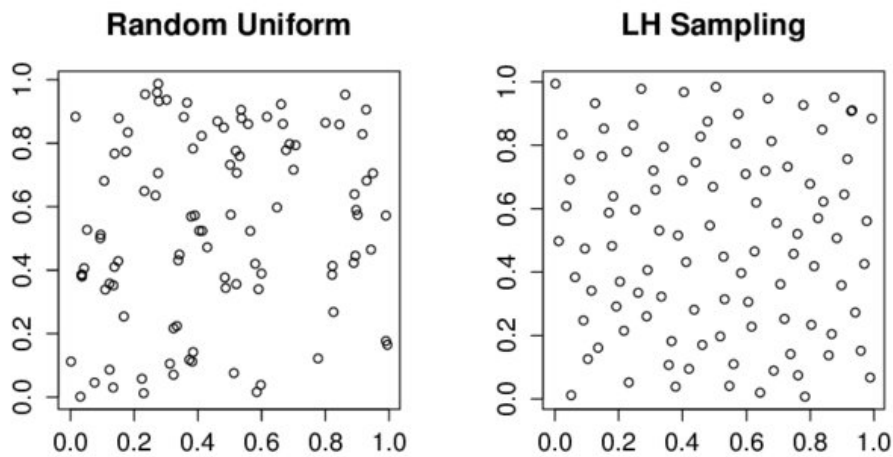


Figure 13: Randomly sampled variables versus Latin hypercube samples (bidimensional space). Source: Rustell (2016).

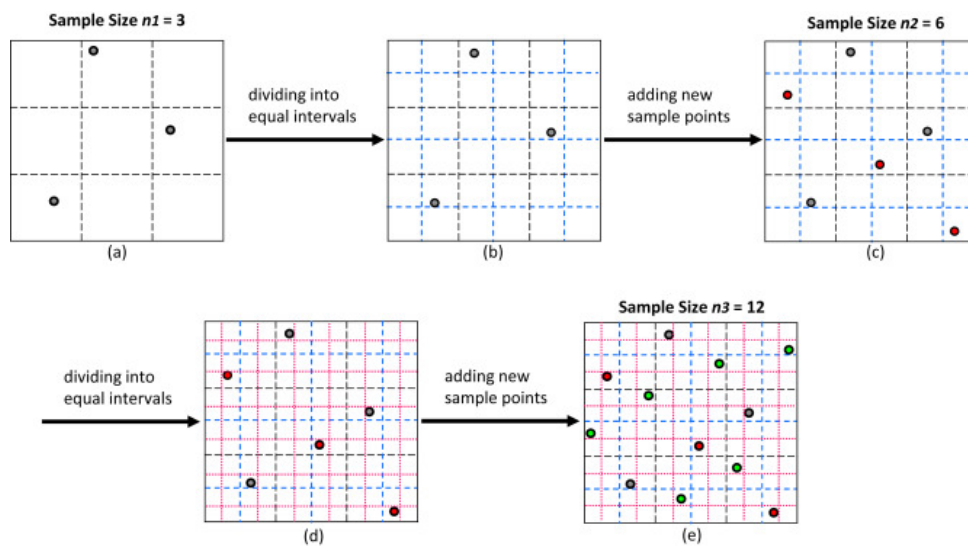


Figure 14: How the LHS works when increasing the number of samples (bidimensional space). Source: Sheikholeslami and Razavi (2017).

comparison.

### 4.3 Feedback Linearization Analysis

In this study, the feedback linearization was applied to the 2-DOF parallel mechanism following equation (3.4) with  $\lambda = 40$  rad/s and using nominal model parameters (Table 3) when computing the system dynamics matrices, resulting in a nominal model with transfer

Table 4: 2-DOF parallel mechanism uncertain parameters.

Sample	Parameter values								
	$m_1$	$m_2$	$l_0$	$l_1$	$l_2$	$l_{g2}$	$l_{g2}$	$J_{z1}$	$J_{z2}$
0	0.062000	0.11050	0.050000	0.12000	0.16000	0.060000	0.068000	0.00027510	0.00045380
1	0.066519	0.11768	0.049419	0.12431	0.15668	0.060668	0.063473	0.00027407	0.00045825
2	0.058819	0.10334	0.051179	0.11835	0.16033	0.057556	0.062037	0.00025282	0.00042336
3	0.060605	0.12133	0.052281	0.11522	0.15305	0.058905	0.066243	0.00028801	0.00043276
4	0.065539	0.10756	0.047835	0.12359	0.16504	0.058455	0.064879	0.00025627	0.00048126
5	0.063954	0.11685	0.049742	0.11442	0.15430	0.065665	0.074037	0.00029748	0.00044855
6	0.062410	0.10074	0.050504	0.12059	0.15827	0.055140	0.070277	0.00029700	0.00049077
7	0.061854	0.10882	0.050124	0.11981	0.15881	0.062739	0.071991	0.00025956	0.00047296
8	0.056080	0.10546	0.048853	0.12523	0.16230	0.063709	0.068421	0.00026950	0.00044164
9	0.067144	0.11303	0.051536	0.12143	0.16728	0.061844	0.067580	0.00028515	0.00041156
10	0.057446	0.11171	0.048408	0.11668	0.16378	0.055423	0.072906	0.00028053	0.00047018
11	0.068200	0.12155	0.052500	0.12600	0.16800	0.066000	0.074800	0.00030261	0.00049918
12	0.055800	0.09945	0.047500	0.11400	0.15200	0.054000	0.061200	0.00024759	0.00040842

function matrix given by:

$$G_0(s) = \frac{q_a(s)}{U_R(s)} = \frac{1600}{s^2 + 40s + 1600} \times I_2. \quad (4.11)$$

$\lambda$  value was chosen as an intermediate choice between the ones proposed for the different controllers and trajectories compared in Coutinho (2020) where, through simulation and experimental results,  $\lambda$  values from 25 rad/s to 70 rad/s were considered. In order to evaluate feedback linearized, that is the system in Figure 4, several open loop simulations were performed using the values from Table 3 for nominal model simulations and from Table 4 for uncertain model simulations. Different sinusoidal reference trajectories were applied according to the following equation system:

$$\begin{cases} x_{ref}(t) &= -0.05 \sin(2\pi ft) \\ y_{ref}(t) &= 0.158 - 0.05 \cos(2\pi ft) \end{cases}, \quad (4.12)$$

with frequencies varying from 0.2 Hz to 16 Hz (the standard operation frequency is 2 Hz). It is worth mentioning that this frequency range was used for all frequency domain simulations performed in this Chapter. The reference trajectory in terms of the end-effector positions  $x(t)$  and  $y(t)$  is presented in Figure 15. Also, all simulations used the same initial conditions:

$$\begin{cases} x(0) &= 0 \\ y(0) &= 0.108 \\ \dot{x}(0) &= -\frac{\pi}{10} \\ \dot{y}(0) &= 0 \end{cases}. \quad (4.13)$$

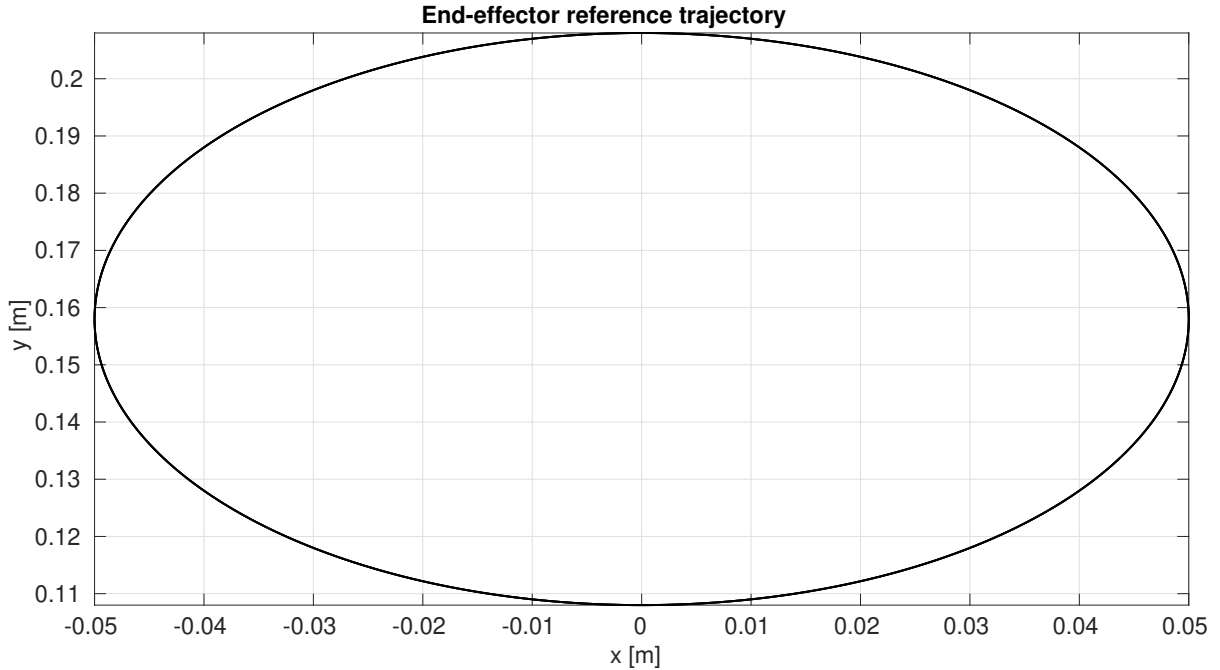


Figure 15: End-effector reference trajectory. Source: the author.

Both reference trajectory and initial conditions were the same used by Coutinho (2020). As they are defined in the end-effector coordinates, the forward kinematics from Section 2.1 was used to generate the complete reference vector  $q_{ref}$ .

It is important to remember that, theoretically, the system has the matrix of transfer functions from equation (4.11), but if there is uncertainty in the parameters, the nonlinearities are not perfectly canceled. The Fast Fourier transform (FFT) was applied to extract the magnitude value at each frequency point for each different input frequency. Then, the magnitude value at the fundamental frequency was considered to generate the simulated curves presented in the frequency responses from this Section. Regarding implementation, the FFT MATLAB built-in function *fft* (MATHWORKS, 2020a) was used – an example of its output is presented in Figure 16. The frequency response from the nominal model described by equation (4.11) is also presented for comparison purposes (Figures 17, 18 and 19).

First, in order to validate the implemented model, the simulation did not consider the effects of any disturbances – that is, the model from Figure 3. The results are presented in Figure 17, which shows that the simulation response is close to the nominal model, as expected since no disturbance is being considered.

Later on, the simulation considered the effects from the feedforward loop for model matrices computation – that is, the model from Figure 4. The results are presented in Figure 18, which shows that the simulation response is close to the nominal model

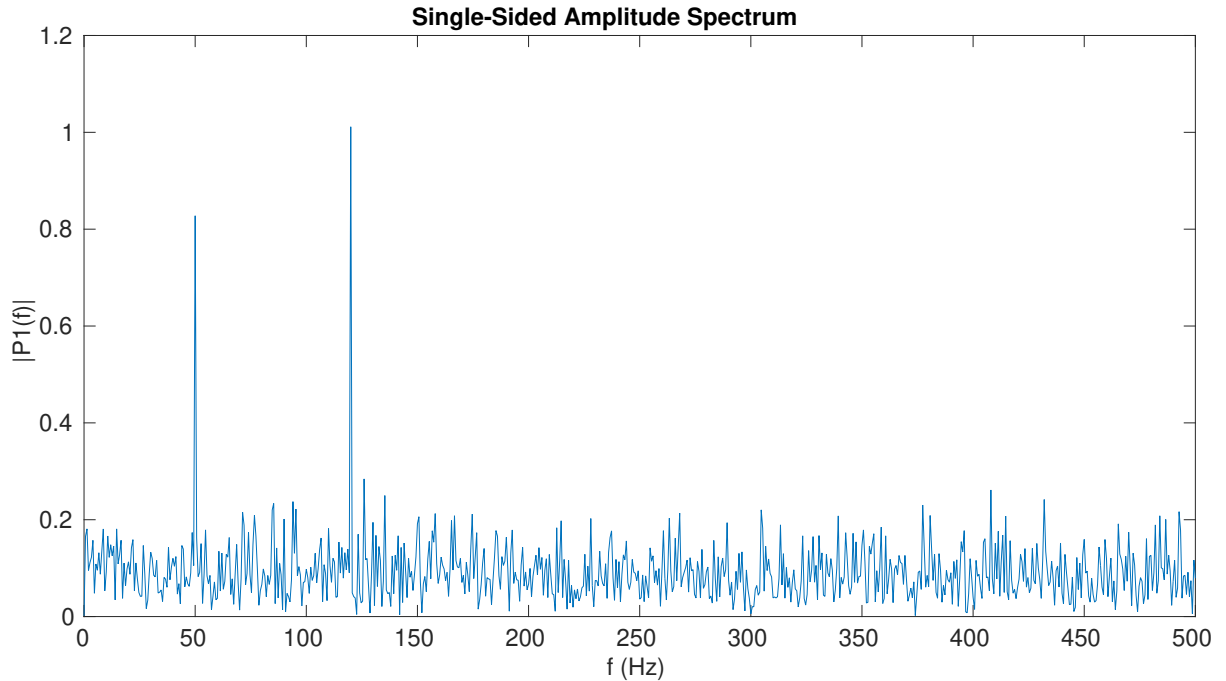


Figure 16: Example of Fourier Transform analysis. Source: MathWorks (2020a).

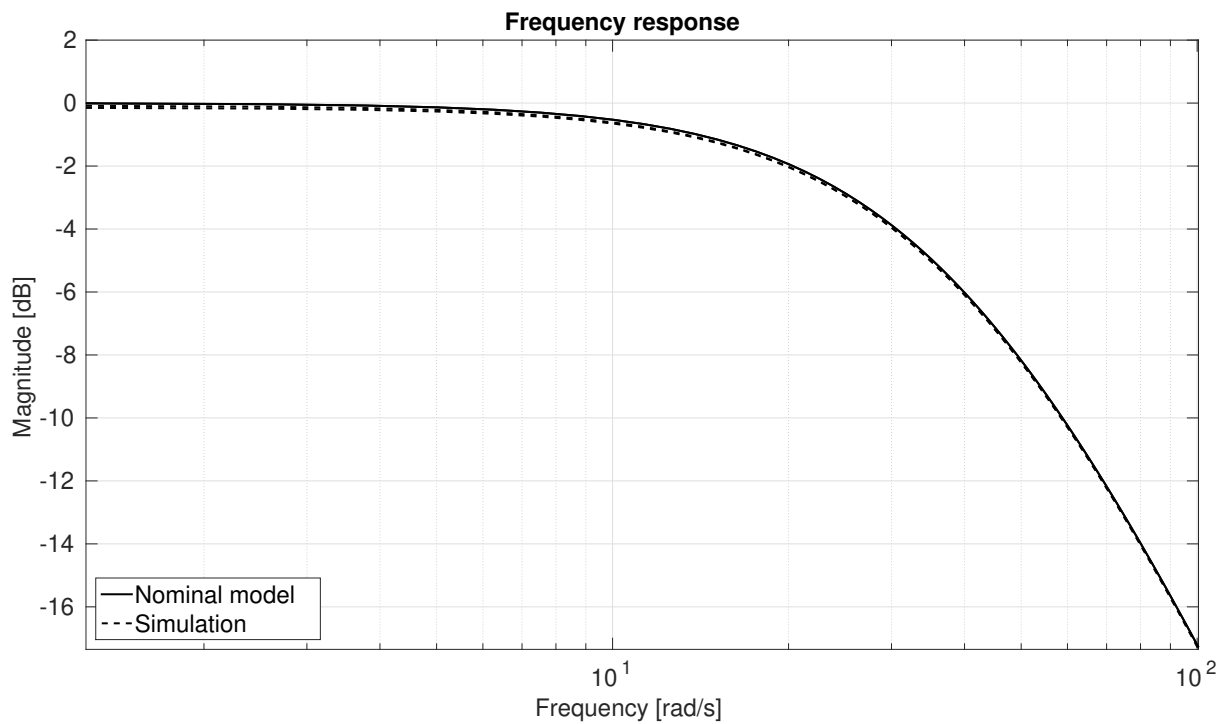


Figure 17: Frequency response considering nominal parameters (Table 3) and no disturbances. Source: the author.

from equation (4.11) for lower frequencies, diverging as the frequency increases. This phenomena is expected when the feedforward loop is used for model matrices computation since a higher frequency means that the input, and consequently the output, variations occur faster, so not using the actual states in model matrices computation is more crucial.

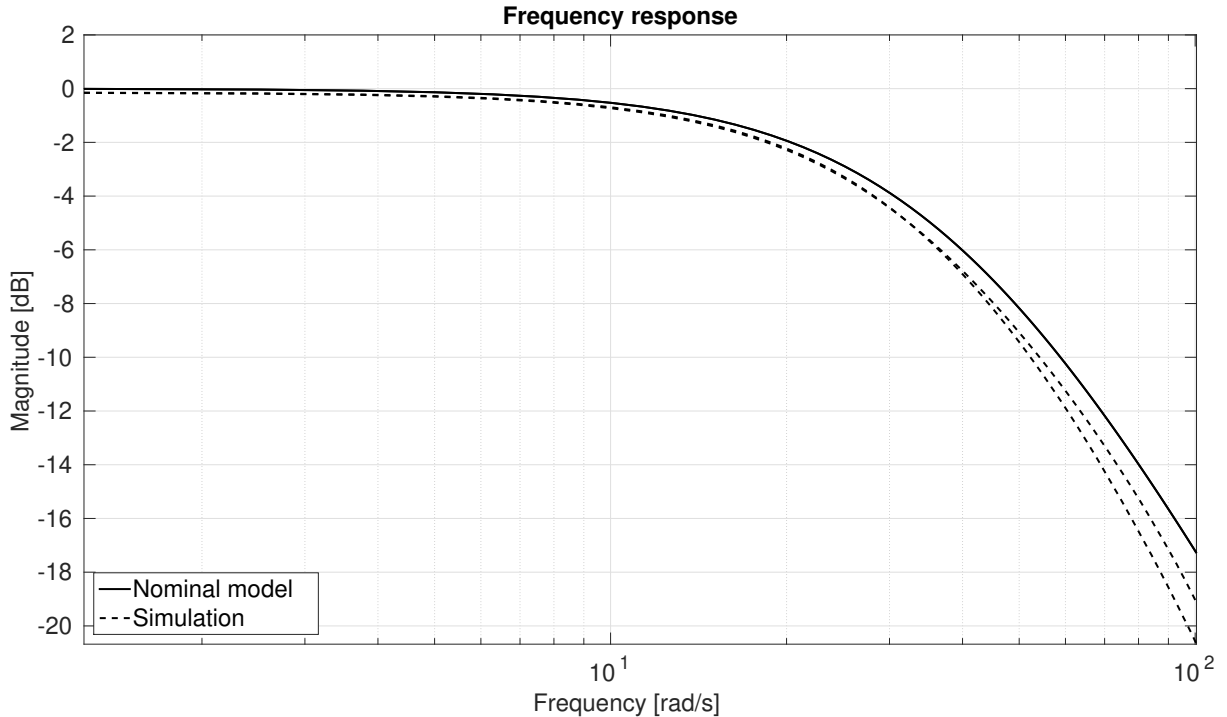


Figure 18: Frequency response considering nominal parameters (Table 3) and feedforward loop for model matrices computation. Source: the author.

Finally, the feedback linearization was applied to the system considering not only the feedforward loop for model matrices computation but also uncertain parameters. The result is expected to differ from the nominal model from equation (4.11) more than the results presented in Figure 18. In order to evaluate this difference, a frequency domain analysis similar to the one carried out for the nominal parameters was performed taking into account all 27 samples of uncertain parameters from Table 4, producing the results presented in Figure 19. With all samples simulated, at each input frequency the results were compared to appoint the minimum and maximum values the different set of parameters could produce, delimiting the range in which all responses were contained (red area in Figure 19). This illustrates the family of plants accounted in Section 3.2.

Also, to validate that this frequency response is reliable to be used for the robust controller design, a total harmonic distortion (THD) analysis was carried out for the output of all uncertain open-loop models simulated samples. Essentially, the THD measures the influence of the harmonics over the total system response. Since a pure linear system should not introduce any harmonics in the output signal, a system output presenting high magnitude harmonics means that the nonlinearities introduced by the system can not be

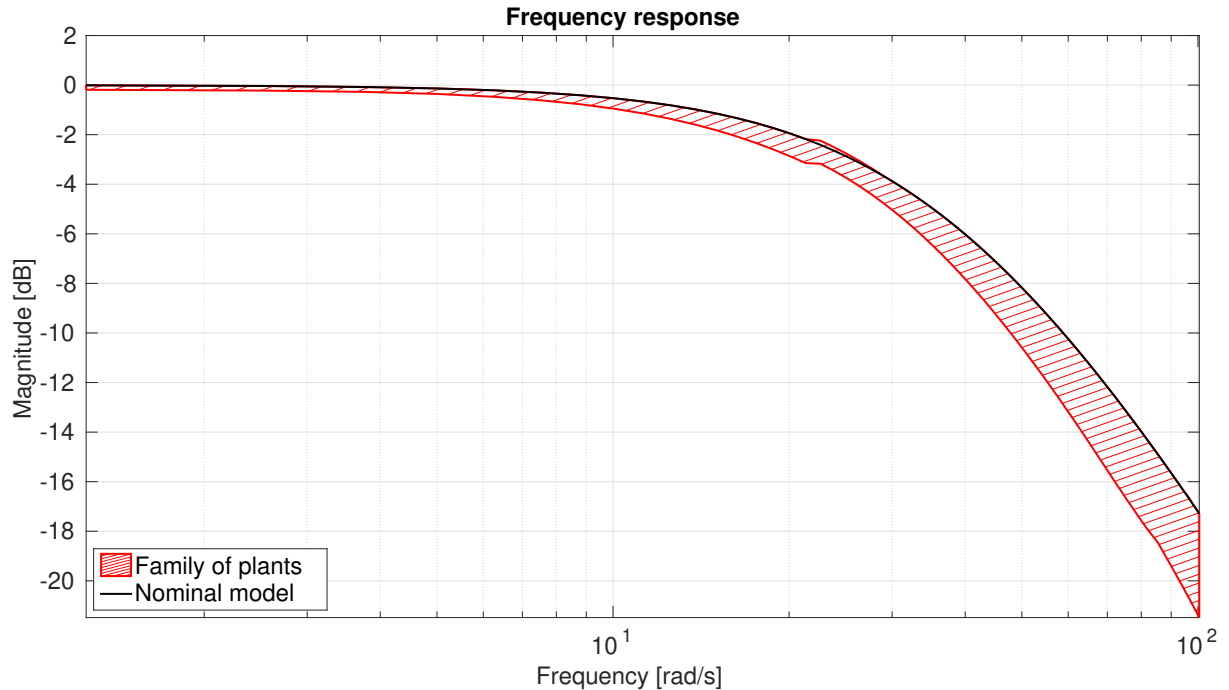


Figure 19: Frequency response considering uncertain parameters (Table 4) and feedforward loop for model matrices computation. Source: the author.

neglected. The THD of a signal is given by:

$$THD = \frac{\sqrt{\sum_{i=2}^n V_i^2}}{V_1}, \quad (4.14)$$

where  $V_1$  is the fundamental frequency magnitude and  $V_i$ ,  $i = 2, 3, \dots, n$  is the  $i^{th}$  harmonic magnitude (SHMILOVITZ, 2005). Regarding implementation, the THD MATLAB built-in function *thd* (MATHWORKS, 2020d) was used and an example of its usage is shown in Figure 20. The analysis was carried out for a subset of frequencies for each sample of Table 4, as shown in Table 5. As an example of the carried out analysis, Figure 21 shows the THD analysis for sample 11 in four different input frequencies – as expected, the THD values match the ones presented in Table 5.

From the data presented in Table 5, in the worst case scenario – that is, the higher total harmonic distortion between all samples among all analyzed frequencies – is -10.33 dB, which means that the fundamental frequency magnitude represents, at least, 70% percent of the system response. In the best scenario – that is, the lower total harmonic distortion between all samples among all analyzed frequencies – is -19.65 dB, which means that the fundamental frequency magnitude represents, at most, 90% percent of the system response. Ideally, in a linear time-invariant system, the fundamental frequency magnitude would be 100%.

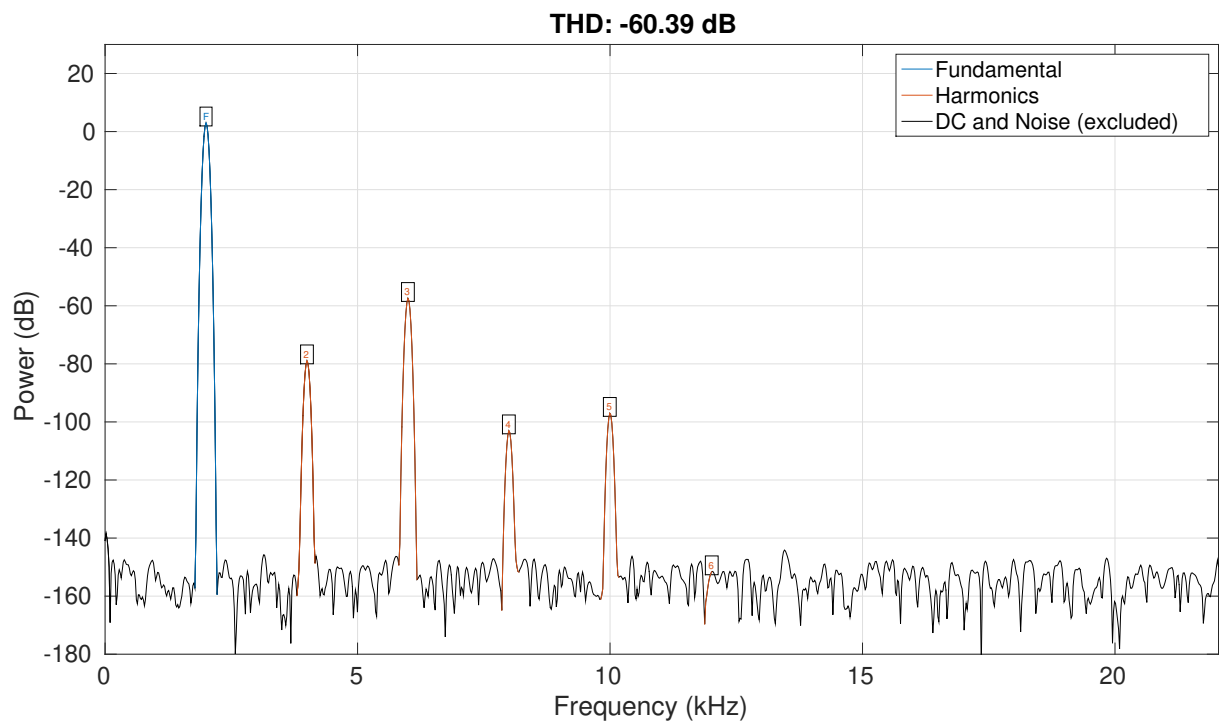
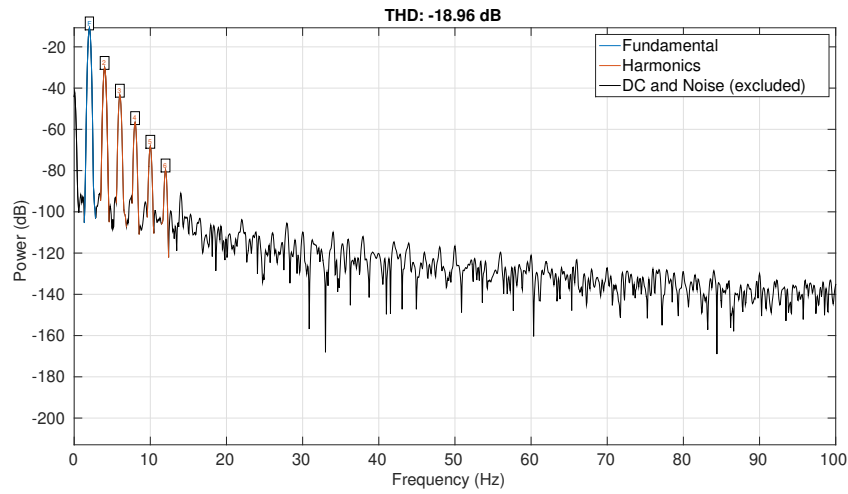


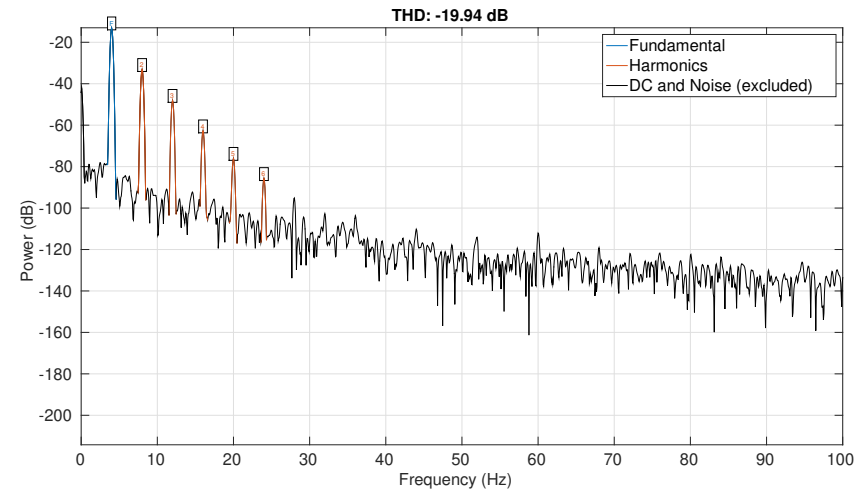
Figure 20: Example of total harmonic distortion analysis. Source: MathWorks (2020d).

Table 5: Total harmonic distortion analysis for open-loop system.

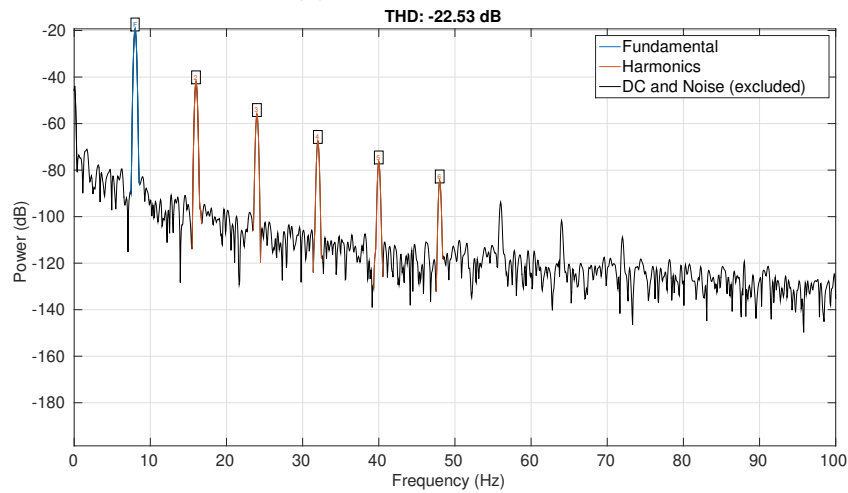
		Total harmonic distortion [dB]															
Sample	Frequency [Hz]	1	2	3	4	5	6	7	8	9	10	11	12	13	14	15	16
	1		-18.49	-19.24	-19.54	-17.14	-16.61	-16.38	-16.28	-16.18	-16.02	-15.69	-15.23	-14.58	-13.86	-14.31	-12.97
2		-18.75	-19.35	-19.62	-19.30	-18.90	-18.52	-18.16	-17.75	-17.24	-16.63	-15.96	-15.15	-14.19	-13.17	-12.08	-10.89
3		-18.19	-18.35	-18.91	-17.85	-17.09	-16.67	-16.37	-16.11	-15.80	-15.35	-14.82	-14.11	-13.30	-12.39	-11.57	-11.86
4		-18.67	-19.30	-19.53	-19.34	-19.19	-19.03	-18.84	-18.55	-18.14	-17.61	-16.92	-16.11	-15.16	-14.13	-13.00	-11.79
5		-18.71	-19.14	-19.30	-18.62	-18.13	-17.81	-17.54	-17.26	-16.89	-16.40	-15.79	-15.00	-14.07	-13.07	-11.97	-10.77
6		-18.69	-19.03	-19.30	-18.65	-17.99	-17.53	-17.16	-16.78	-16.36	-15.84	-15.21	-14.40	-13.50	-12.52	-11.46	-10.33
7		-18.70	-19.12	-19.38	-18.67	-18.13	-17.77	-17.47	-17.16	-16.79	-16.29	-15.65	-14.87	-13.97	-12.95	-11.84	-10.66
8		-18.68	-19.10	-19.40	-18.81	-18.37	-18.06	-17.79	-17.51	-17.11	-16.61	-15.98	-15.17	-14.25	-13.23	-12.10	-10.92
9		-18.67	-19.29	-19.48	-19.30	-19.16	-19.03	-18.85	-18.57	-18.19	-17.67	-16.99	-16.18	-15.22	-14.20	-13.06	-11.86
10		-18.71	-19.41	-19.50	-19.36	-19.22	-19.10	-18.90	-18.59	-18.20	-17.63	-16.96	-16.15	-15.23	-14.20	-13.08	-11.91
11		-18.59	-18.96	-19.05	-18.49	-18.24	-18.16	-18.12	-18.01	-17.77	-17.35	-16.75	-15.96	-15.03	-13.94	-12.79	-11.56
12		-18.81	-19.41	-19.65	-19.32	-18.81	-18.33	-17.85	-17.35	-16.81	-16.16	-15.42	-14.58	-13.64	-12.63	-11.52	-10.33



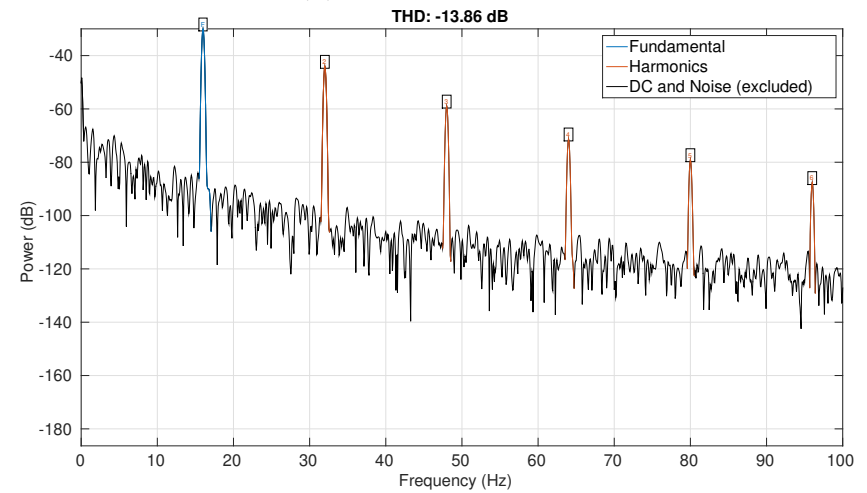
(a) Input signal 2 Hz.



(b) Input signal 4 Hz.



(c) Input signal 8 Hz.



(d) Input signal 16 Hz.

Figure 21: Total harmonic distortion analysis for sample 11 open-loop simulation. Source: the author.

## 4.4 Robust Control Analysis and Design

As can be seen in Figure 19, the family of plants is well behaved in the sense that the red area follows the same shape of the nominal model, approximately. Yet, the nominal response is not in the center of the family of plants, as expected. Therefore, a new nominal plant is proposed for the robust control design in order to place its response in the center of the family of plants, allowing the lumped disturbance to be treated as a multiplicative model uncertainty and the family of plants being represented by equation (3.6). As presented in Figure 22, the new centric nominal plant  $G(s)$  is given by:

$$G(s) = \frac{1518.2}{(s + 39.17)(s + 39.16)}. \quad (4.15)$$

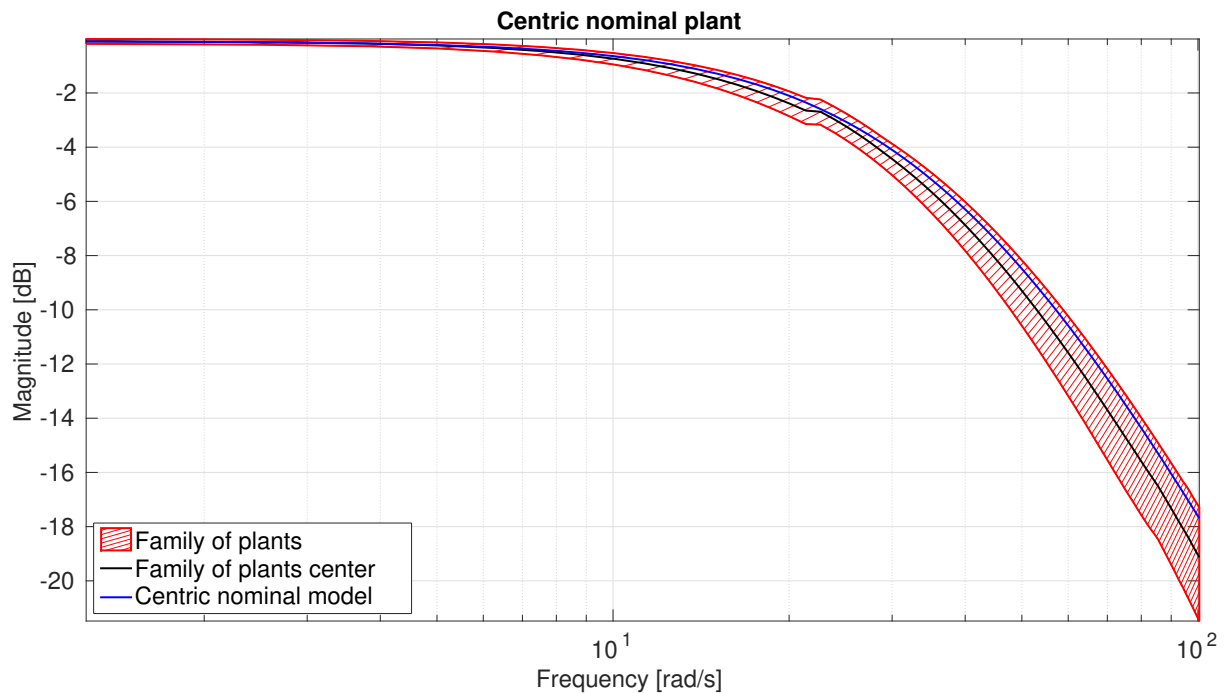


Figure 22: Frequency response considering uncertain parameters (Table 4) and feed-forward loop for model matrices computation, with new proposed nominal plant  $G(s)$ . Source: the author.

As stated in Section 3.2, the worst case uncertainty  $l_m(\omega)$  given by equation (3.15) represents the range within the uncertain plants responses are contained. Considering the 2-DOF parallel mechanism disturbed by the use of uncertain parameters from Table 4 and the inclusion of pre-computed feedforward loop as in Figure 8,  $l_m(\omega)$  with respect to  $G(s)$  from equation (4.15) is presented in Figure 23. Also, Figure 23 presents the uncertainty upper bound  $w_\Delta(s)$  defined by equation (3.16) and parameterized according

to the resultant  $l_m(\omega)$  as:

$$w_\Delta(s) = \frac{0.75(s + 2)}{(s + 150)}. \quad (4.16)$$

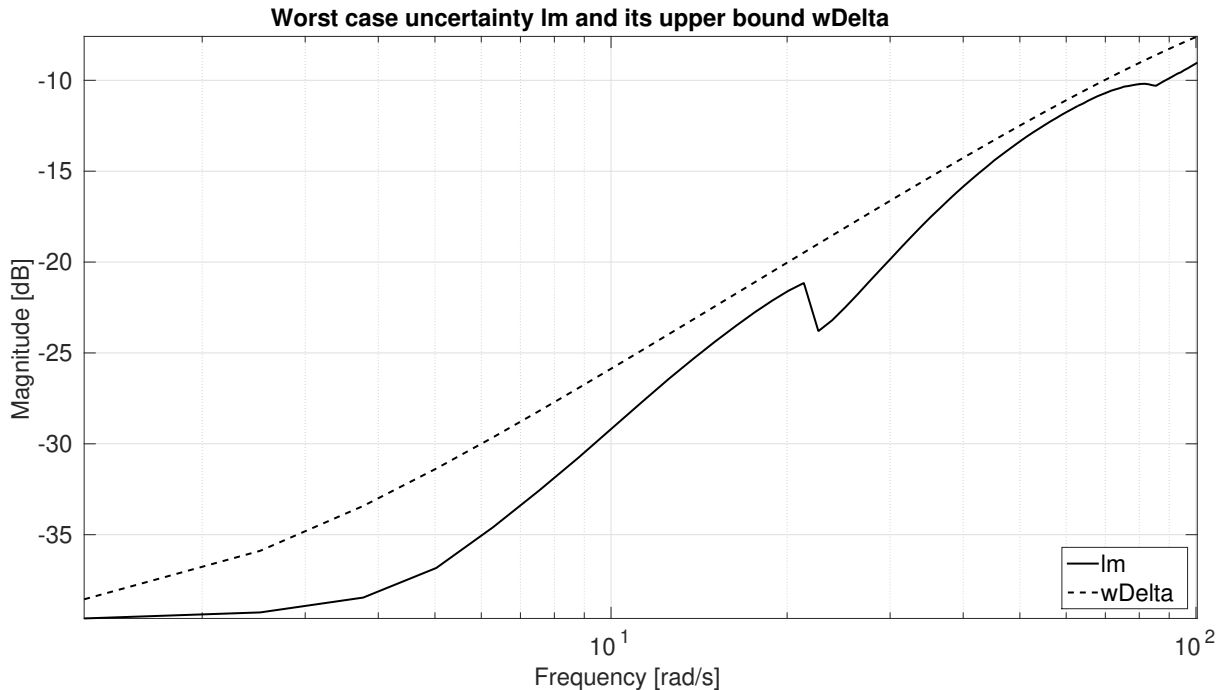


Figure 23: Worst case uncertainty  $l_m(\omega)$  and its upper bound  $w_\Delta(s)$  respective to the centric nominal model  $G(s)$ . Source: the author.

Also, the nominal performance condition  $w_P(s)$  defined by equation (3.14) is parameterized with  $A = 0.001$ ,  $M = 3$  and  $\omega_B^* = 25.13$  rad/s, resulting in:

$$w_P(s) = \frac{0.33(s + 75.4)}{(s + 0.02513)}, \quad (4.17)$$

where  $M$  was chosen in order to reduce oscillations during transient state while attenuating the influence of disturbances,  $A$  was chosen to reduce steady-state error considering a step input and  $\omega_B^*$  was chosen to define a frequency range including the operation frequency (2 Hz) where the system would response according to the desired performance criteria.

Now, in order to compute the  $H_\infty$  robust controller through the mixed-sensitivity design method presented in Section 3.2.2.1, weight functions  $W_1(s)$ ,  $W_2(s)$  and  $W_3(s)$  must be defined. Typically, they are defined as follows:

$$W_1(s) = w_\Delta(s), \quad (4.18)$$

$$W_2(s) = w_u(s), \quad (4.19)$$

$$W_3(s) = w_P(s), \quad (4.20)$$

with  $w_u(s)$  as a control signal weight function usually given as a constant gain. For this control design,  $w_u(s) = 0.1$ . The weight functions are presented in Figure 24.

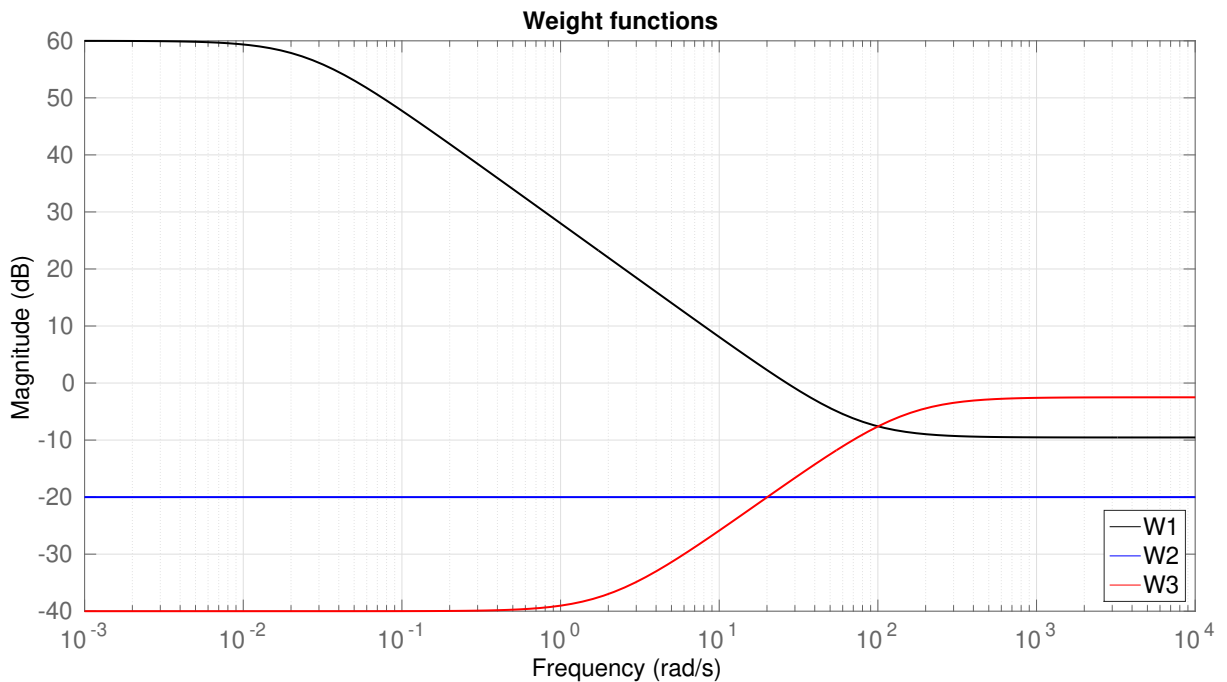


Figure 24: Weight functions for mixed-sensitivity design. Source: the author.

The mixed-sensitivity  $H_\infty$  synthesis MATLAB built-in function *mixsyn* (MATWORKS, 2020c) was used to compute the sub-optimal  $H_\infty$ . This function takes as inputs the nominal plant  $G(s)$  from equation (4.15) and the weight functions  $W_1(s)$ ,  $W_2(s)$  and  $W_3(s)$  to formulate the augmented plant  $P(s)$  presented in Figure 6 and synthesize the sub-optimal  $H_\infty$  controller. The synthesized controller is given by (it is omitted here the multiplication by the  $2 \times 2$  identity matrix for all the matrix of transfer functions):

$$K_{mixsyn} = \frac{13696(s + 39.17)(s + 39.16)(s + 150)}{(s + 2703)(s + 0.02513)(s^2 + 326.3s + 27430)}, \quad (4.21)$$

with a controller performance parameter  $\gamma = 0.6058$ . As  $\gamma < 1$ , this means that the resultant controller satisfy the design criteria imposed by the weight functions  $W_1(s)$ ,  $W_2(s)$  and  $W_3(s)$ .

Typically, the  $H_\infty$  synthesis return high order controllers. In this case, the synthesized controller is of 4th order. Since the parallel mechanism operation frequency is 2 Hz, an order reduction was performed focusing on approximate the original controller frequency response in lower frequencies with the trade-off of a different response in higher ones. Therefore, the original synthesized controller frequency response was manually approximated by a first order transfer function as shown in Figure 25, where the reduced order

controller  $K(s)$  is given by:

$$K(s) = \frac{1.7(s + 24)}{(s + 0.025)}. \quad (4.22)$$

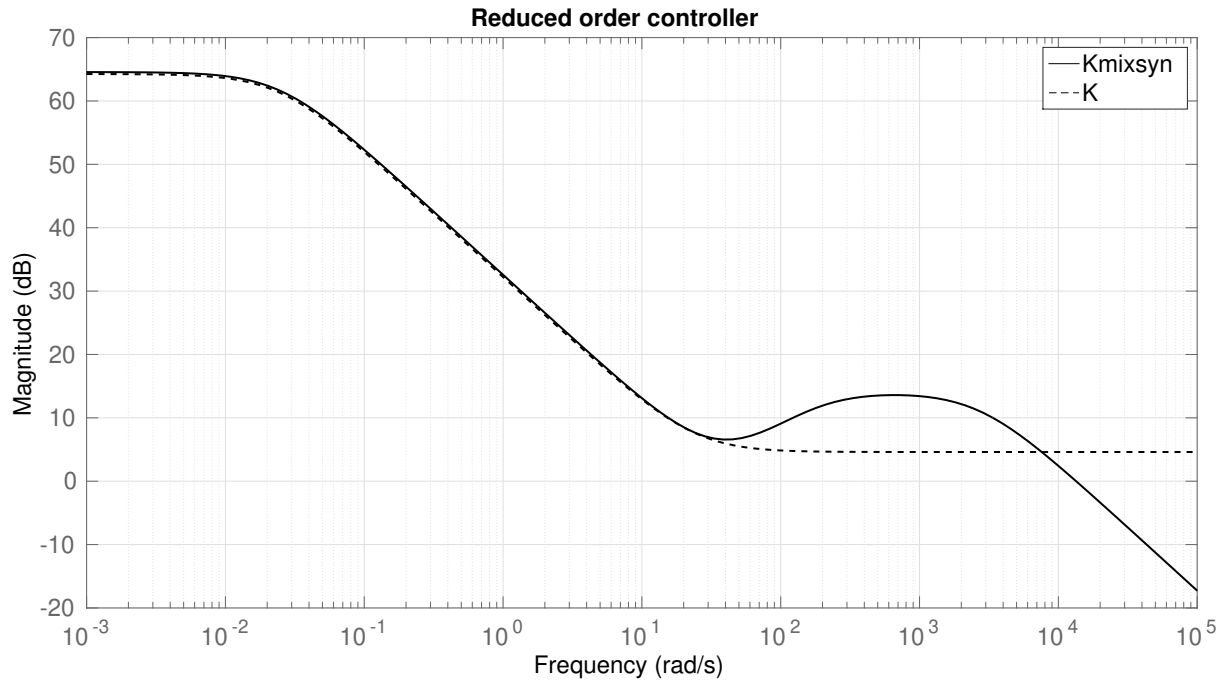


Figure 25:  $H_\infty$  controller order reduction. Source: the author.

With the final controller  $K(s)$ , it is possible to obtain the closed-loop transfer functions  $S(s)$  and  $T(s)$  with respect to the centric nominal model  $G(s)$ :

$$S(s) = \frac{(s + 39.17)(s + 39.16)(s + 0.025)}{(s + 21.38)(s^2 + 56.98s + 2899)} \quad (4.23)$$

$$T(s) = \frac{2580.9(s + 24)}{(s + 21.38)(s^2 + 56.98s + 2899)}, \quad (4.24)$$

with both functions being represented in Figure 26.

Now, it is time to verify whether the controller  $K(s)$  satisfies the closed-loop control criteria from equation (3.41): nominal performance and robust stability and performance. Evaluating equation (3.41) with the controller  $K(s)$  from equation (4.22), the uncertainty upper bound  $w_\Delta(s)$  from equation (4.16) and the nominal performance weight  $w_P(s)$  from equation (4.17), one gets:

$$\|w_p(s)S(s)\|_\infty = 0.7704 < 1 \Leftrightarrow \text{NP is achieved}, \quad (4.25)$$

$$\|w_\Delta(s)T(s)\|_\infty = 0.2171 < 1 \Leftrightarrow \text{RS is achieved}, \quad (4.26)$$

$$\|w_p(s)S(s)\|_\infty + \|w_\Delta(s)T(s)\|_\infty = 0.9874 < 1 \Leftrightarrow \text{RP is achieved}. \quad (4.27)$$

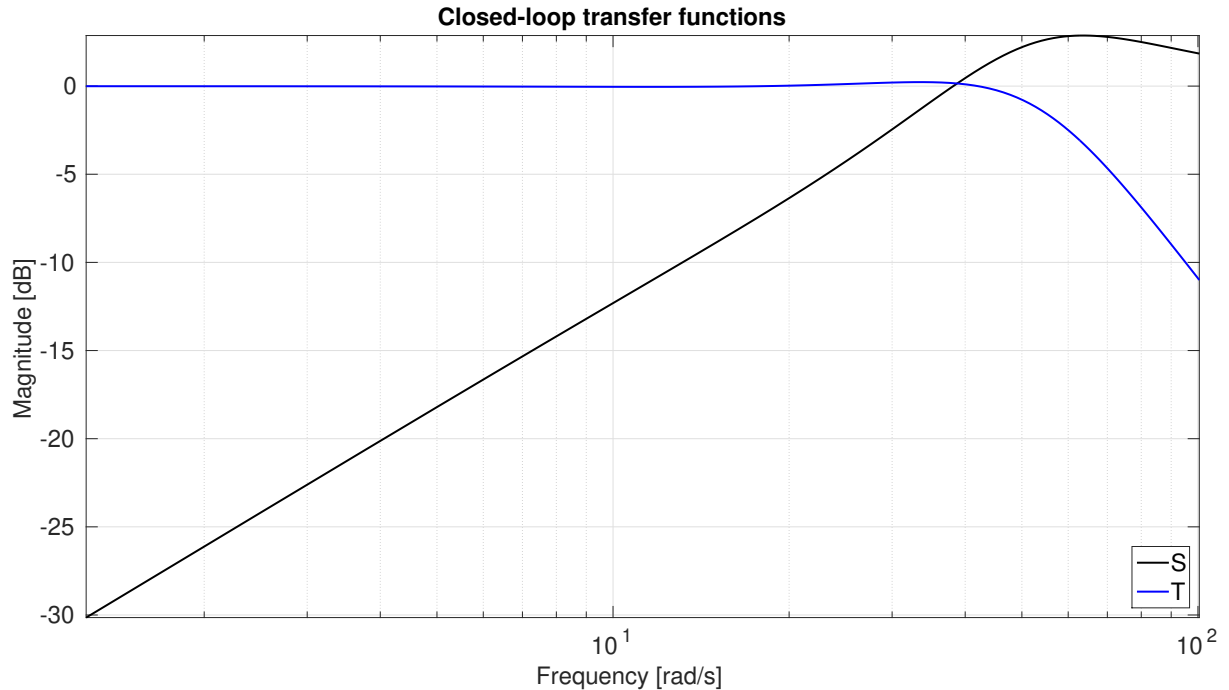


Figure 26: Closed-loop transfer functions  $S(s)$  and  $T(s)$  respective to the centric nominal model  $G(s)$ . Source: the author.

To validate the robust control design, the same simulation procedure applied in Section 4.3 was used. In this case, the feedback linearization was applied to the system considering the feedforward loop for model matrices pre-computation and uncertain parameters, with the control loop being closed with the robust controller  $K(s)$  as shown in Figure 8. The results are presented in Figure 27.

As expected, the closed-loop transfer function  $T(s)$  response (blue line) remains inside the family of close-loop plants response (red area). Also, it can be noticed that the family of closed-loop plants response remains close to the centric closed-loop system until the performance bandwidth  $\omega_B^* = 25.13$ , dispersing as the frequency increases. Then, a harmonic distortion analysis similar to the one performed on Section 4.3 was carried out for all uncertain closed-loop models simulated samples. The analysis was carried out for a subset of frequencies for all the LHS samples, as shown in Table 6. As an example of the carried out analysis, Figure 28 shows the THD analysis for sample 11 in four different input frequencies – as expected, the THD values match the ones presented in Table 6.

From the data presented in Table 6, in the worst case scenario – that is, the higher total harmonic distortion between all samples among all analyzed frequencies – is -14.65 dB, which means that the fundamental frequency magnitude represents, at least, 82% percent of the system response. In the best scenario – that is, the lower total harmonic distortion between all samples among all analyzed frequencies – is -20.95 dB, which means

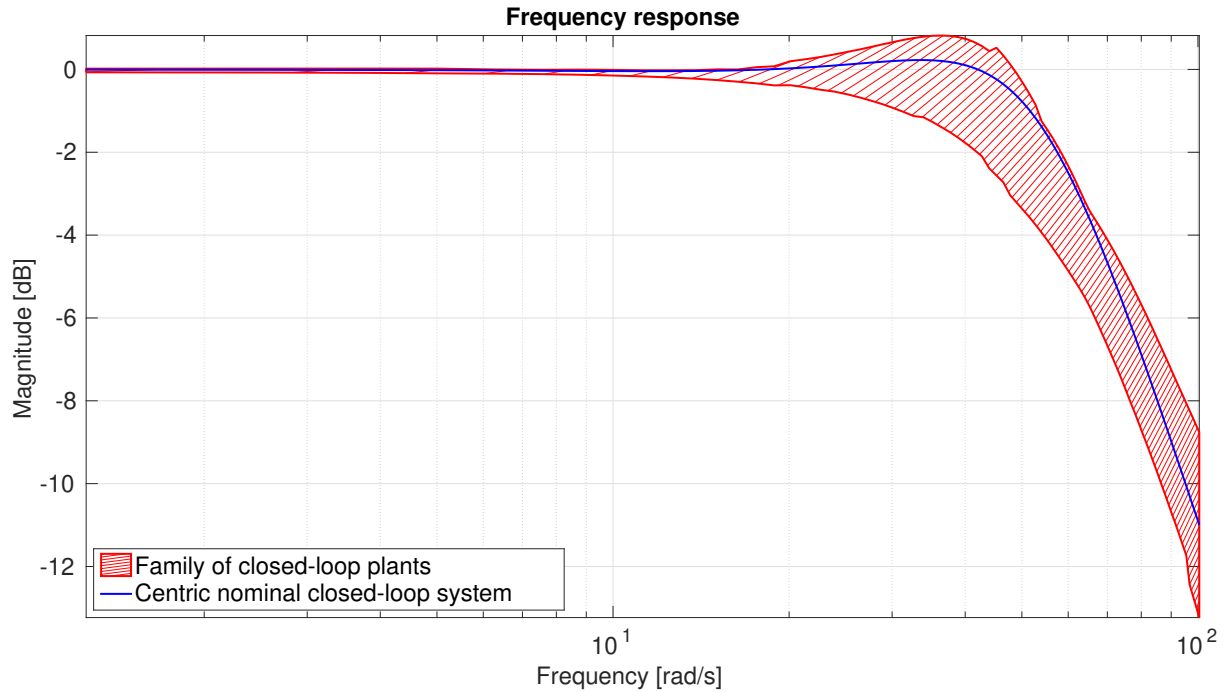
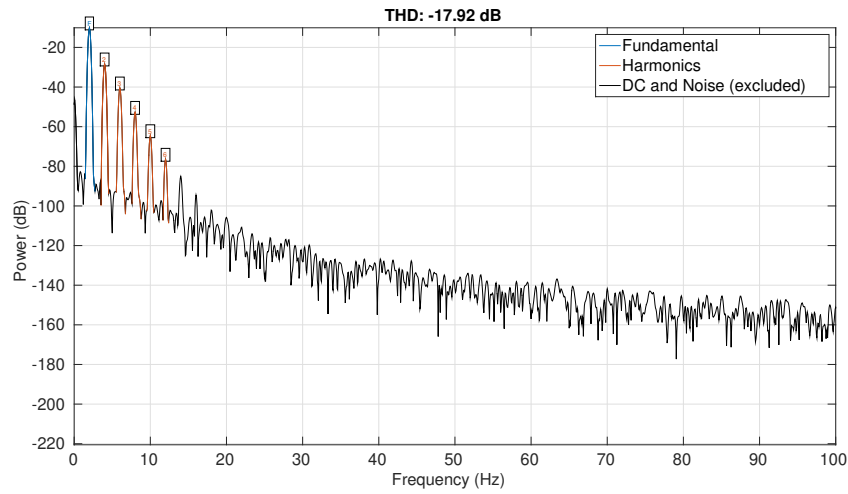


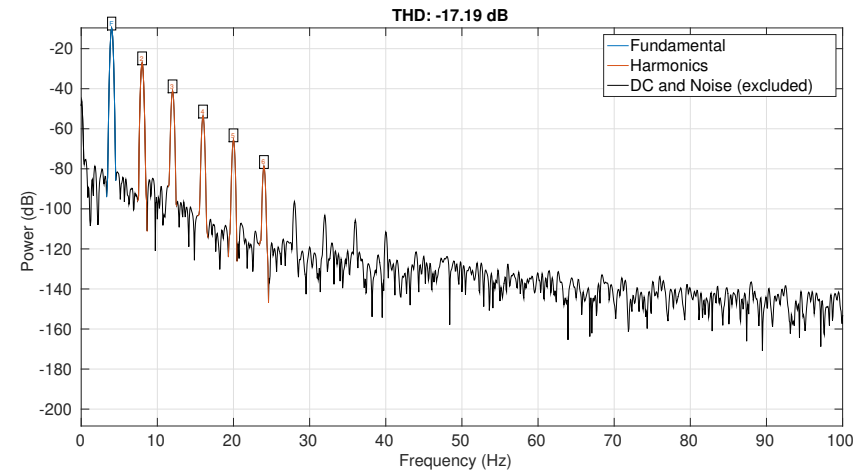
Figure 27: Closed-loop frequency response considering uncertain parameters (Table 4) and feedforward loop for model matrices computation. Source: the author.

that the fundamental frequency magnitude represents, at most, 91% percent of the system response. The higher THD significantly decreased in comparison to the open-loop analysis from Section 4.3, which means that the harmonics have less influence on the system response so the nonlinear components are smaller with the robust controller.

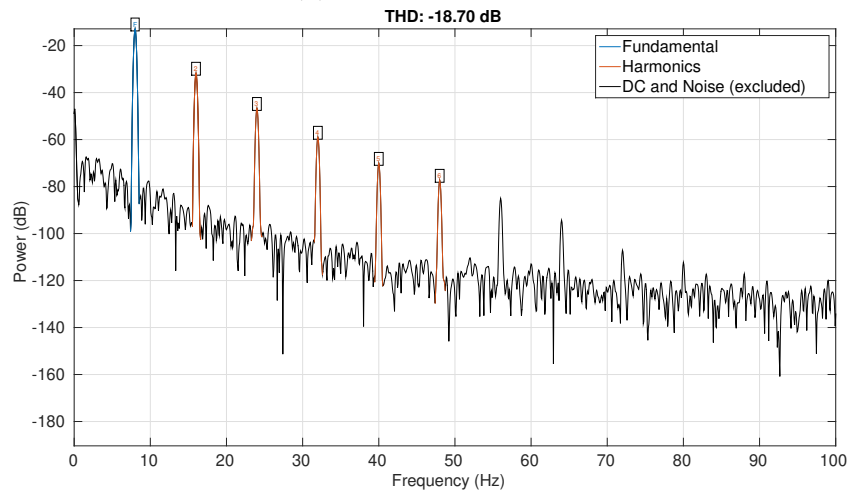
Computing the mean values and standard deviations for each column in Tables 5 and 6 and plotting them in Figure 29, it is possible to notice that the open-loop system without robust controller THD values increase with the frequency, which means that the nonlinear components become more relevant in higher frequencies. On the other hand, the closed-loop system with robust controller THD values tend to remain around a constant value, indicating that the nonlinear components influence does not depend on the frequency.



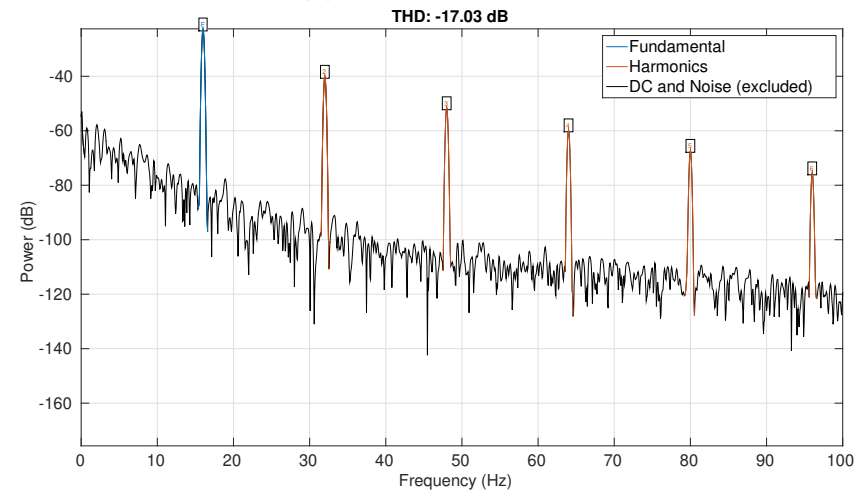
(a) Input signal 2 Hz.



(b) Input signal 4 Hz.



(c) Input signal 8 Hz.



(d) Input signal 16 Hz.

Figure 28: Total harmonic distortion analysis for sample number 11 closed-loop simulation. Source: the author.

Table 6: Total harmonic distortion analysis for closed-loop system.

Sample	Frequency [Hz]	Total harmonic distortion [dB]															
		1	2	3	4	5	6	7	8	9	10	11	12	13	14	15	16
1		-18.14	-17.57	-16.45	-16.17	-16.45	-16.94	-17.44	-14.65	-18.35	-18.70	-18.31	-19.02	-18.94	-18.64	-18.18	-19.51
2		-18.32	-18.19	-18.02	-17.70	-17.90	-18.28	-18.39	-18.44	-18.46	-18.42	-18.24	-17.99	-17.61	-17.13	-16.53	-15.90
3		-18.22	-18.02	-16.59	-15.68	-17.36	-17.53	-15.07	-15.26	-15.91	-16.78	-18.20	-18.10	-17.88	-17.52	-17.04	-16.43
4		-18.30	-18.09	-17.80	-17.78	-18.01	-18.31	-18.57	-18.77	-18.88	-18.89	-18.80	-18.56	-18.22	-17.73	-17.15	-16.47
5		-18.29	-18.15	-17.72	-17.44	-17.65	-17.92	-17.30	-18.29	-18.34	-18.32	-18.22	-18.01	-17.67	-17.24	-16.68	-16.05
6		-18.28	-18.15	-17.64	-17.74	-17.77	-17.61	-16.89	-16.66	-16.96	-18.27	-18.23	-18.08	-17.80	-17.42	-16.92	-16.31
7		-18.30	-18.15	-17.92	-17.34	-17.51	-17.93	-17.24	-17.16	-18.33	-18.33	-18.25	-18.07	-17.77	-17.33	-16.77	-16.14
8		-18.29	-18.09	-17.80	-17.71	-17.56	-18.02	-17.57	-17.59	-18.57	-18.60	-18.55	-18.38	-18.07	-17.63	-17.06	-16.40
9		-18.31	-17.97	-17.83	-17.80	-18.02	-18.33	-18.60	-18.79	-18.86	-18.85	-18.73	-18.45	-18.06	-17.57	-16.98	-16.27
10		-18.32	-18.08	-17.77	-17.88	-18.43	-18.51	-18.71	-19.12	-19.66	-20.18	-20.62	-20.89	-20.95	-20.87	-20.56	-20.08
11		-18.25	-17.92	-17.50	-17.19	-17.75	-17.88	-17.49	-18.70	-18.94	-19.07	-19.11	-19.03	-18.79	-18.31	-17.72	-17.03
12		-18.34	-18.31	-18.23	-17.87	-17.92	-18.17	-18.21	-18.27	-18.19	-18.06	-17.81	-17.50	-17.10	-16.58	-16.00	-15.37

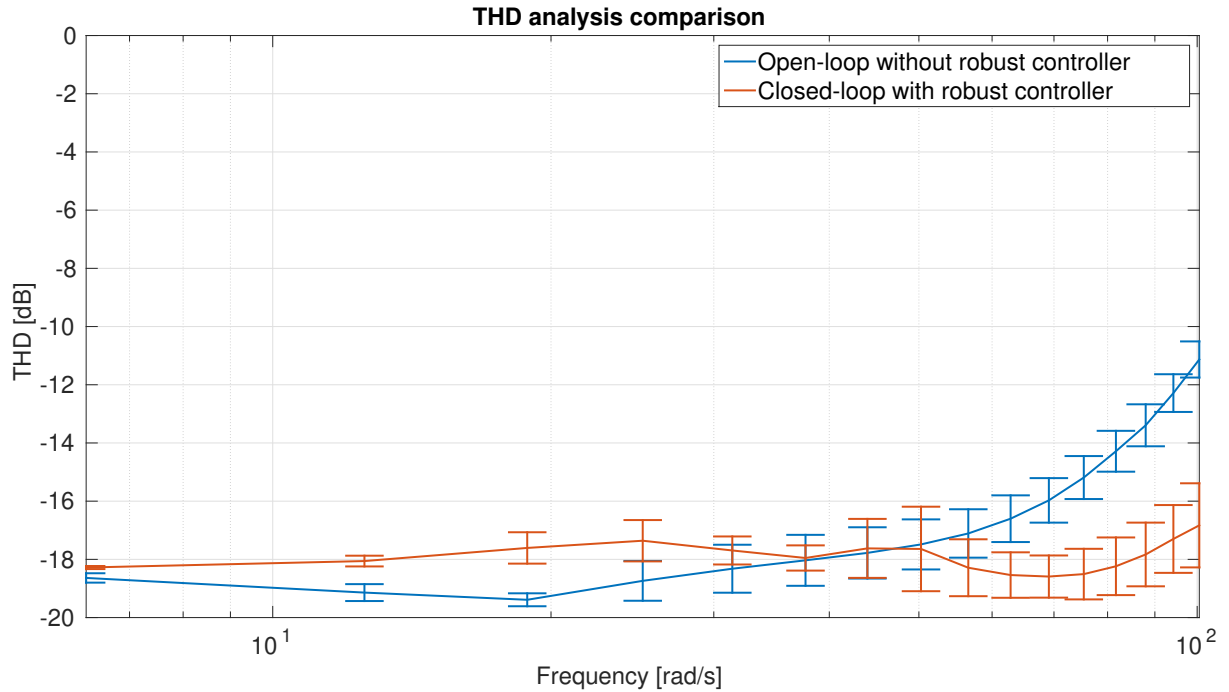


Figure 29: THD analysis comparison. Source: the author.

Finally, the closed-loop system responses with and without the robust controller were compared through time domain simulations in order to evaluate the influence of the robust controller over the system performance. Sample 11 was considered during all simulations. Joints  $\theta_{1,1}$  and  $\theta_{2,1}$  were considered for this analysis since they are the actuated variables, as mentioned in Chapter 2. The results are presented in Figures 30, 31 and 32. The root-mean-square error (RMSE) of the responses was also evaluated, the results are presented in Table 7.

Table 7: RMSE for closed-loop time domain simulation.

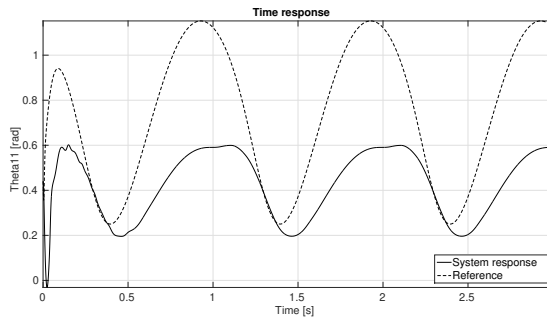
		RMSE			
		Without robust controller		With robust controller	
Frequency [Hz]	Joint	$\theta_{1,1}$	$\theta_{2,1}$	$\theta_{1,1}$	$\theta_{2,1}$
1		0.3758	0.3698	0.0757	0.0894
2		0.3888	0.3733	0.1120	0.1270
4		0.4396	0.4083	0.2079	0.2186

As expected, for lower frequencies the robust controller influence is more apparent, reducing the RMSE in almost 80% in the best scenario. For higher frequencies, although the RMSE reduction was not as high as in the lower frequencies case, a slightly reduction of almost 50% was observed. The robust controller influence can also be qualitative checked through Figures 30, 31 and 32 as the system response is closer to the reference

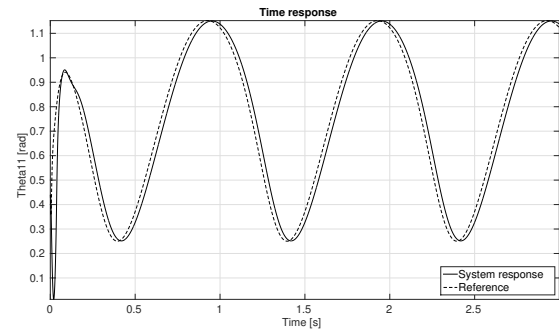
signal.

Analyzing each time domain response, with 1 Hz and 2 Hz input frequencies (Figures 30 and 31) the steady-state control effort remain below the actuators saturation threshold – which is around 8 A. With 4 Hz input frequency (Figure 32), the control effort exceeded this limit even in steady-state, which is expected since faster reference signals require higher control efforts. Despite that, in comparison to the closed-loop response without the robust controller, all different input frequencies responses presented an expressive reduction in control effort in steady-state. Regarding control effort in transient state, no substantial improvement was observed in all different input frequencies responses when comparing the closed-loop responses with and without the robust controller, all of them exceeding the actuators saturation threshold – even the operation frequency response (2Hz). Summarizing, the control effort presented a significant decrease in the presence of the robust controller in steady-state, but it exceeded the actuators saturation during transient state. For future development, the robust controller could be redesigned to treat this aspect as well.

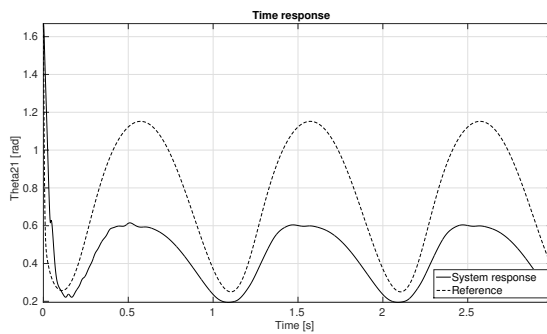
Nevertheless, the robust controller promote a significant improvement in the system closed-loop performance in the presence of model uncertainties, enhancing the system robustness in comparison to using only the feedback linearization approach.



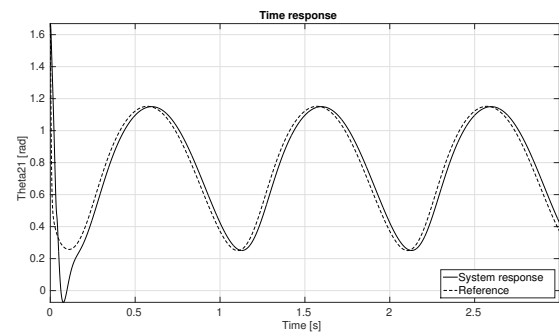
(a) Actuated joint  $\theta_{1,1}$  in closed-loop simulation without robust controller.



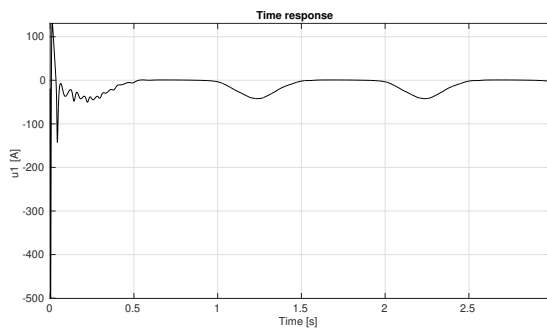
(b) Actuated joint  $\theta_{1,1}$  in closed-loop simulation with robust controller.



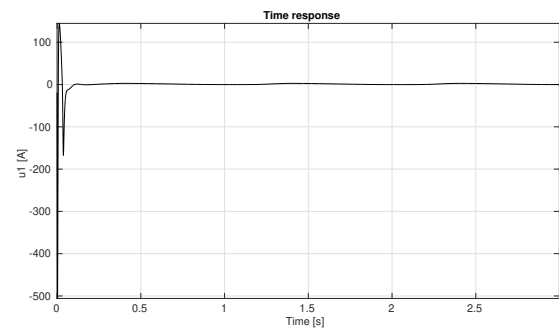
(c) Actuated joint  $\theta_{2,1}$  in closed-loop simulation without robust controller.



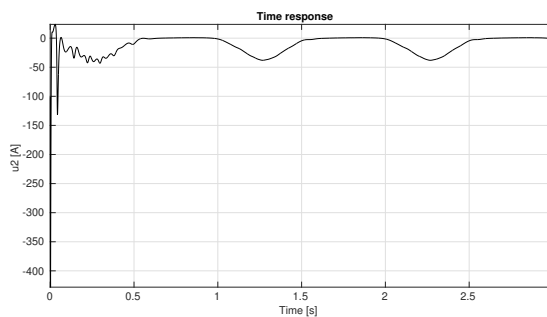
(d) Actuated joint  $\theta_{2,1}$  in closed-loop simulation with robust controller.



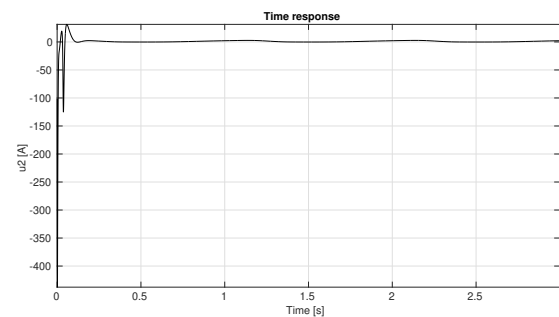
(e) Control effort  $u_{a1}$  in closed-loop simulation without robust controller.



(f) Control effort  $u_{a1}$  in closed-loop simulation with robust controller.

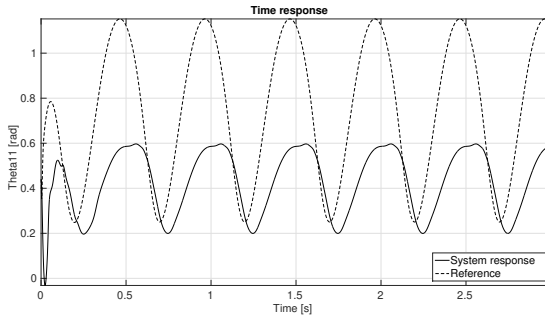


(g) Control effort  $u_{a2}$  in closed-loop simulation without robust controller.

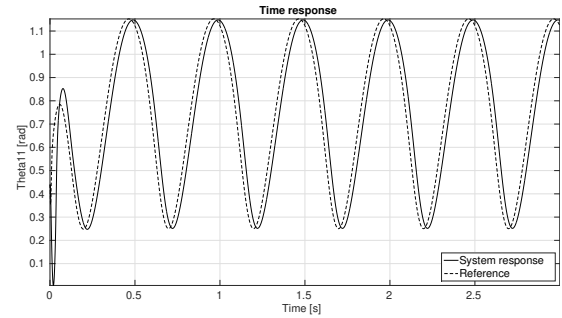


(h) Control effort  $u_{a2}$  in closed-loop simulation with robust controller.

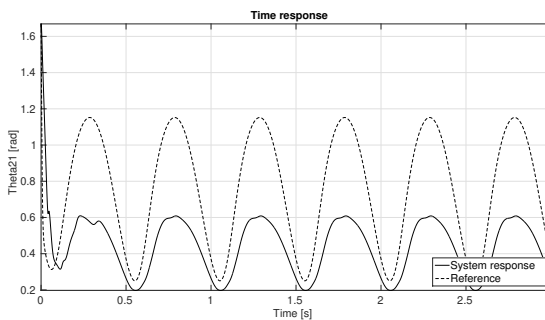
Figure 30: Time domain simulation with 1 Hz reference signal. Source: the author.



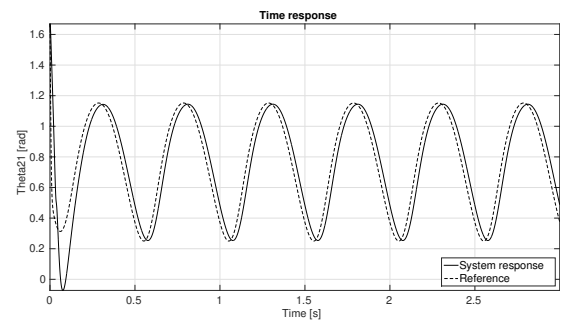
(a) Actuated joint  $\theta_{1,1}$  in closed-loop simulation without robust controller.



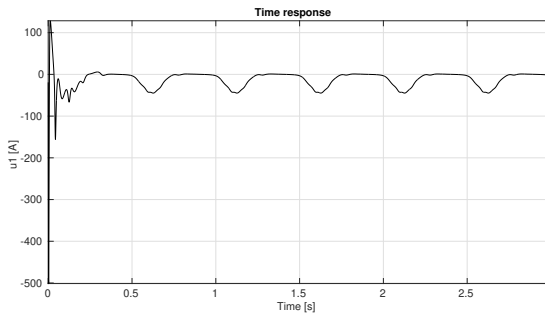
(b) Actuated joint  $\theta_{1,1}$  in closed-loop simulation with robust controller.



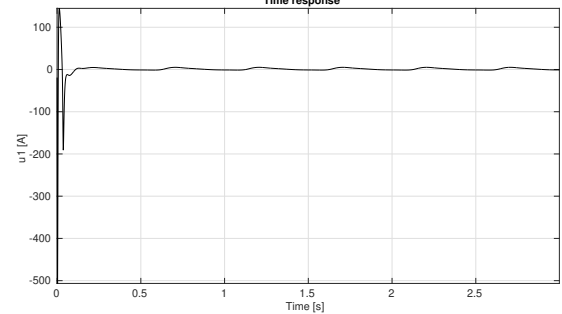
(c) Actuated joint  $\theta_{2,1}$  in closed-loop simulation without robust controller.



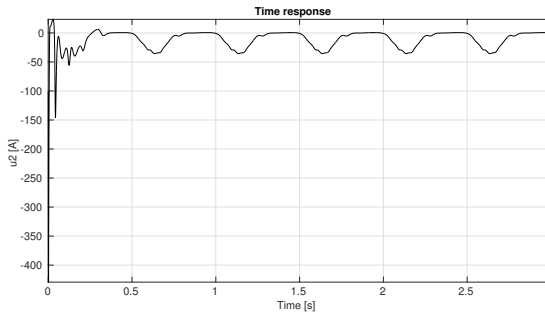
(d) Actuated joint  $\theta_{2,1}$  in closed-loop simulation with robust controller.



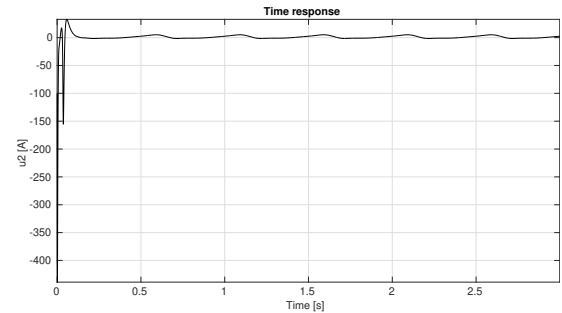
(e) Control effort  $u_{a1}$  in closed-loop simulation without robust controller.



(f) Control effort  $u_{a1}$  in closed-loop simulation with robust controller.

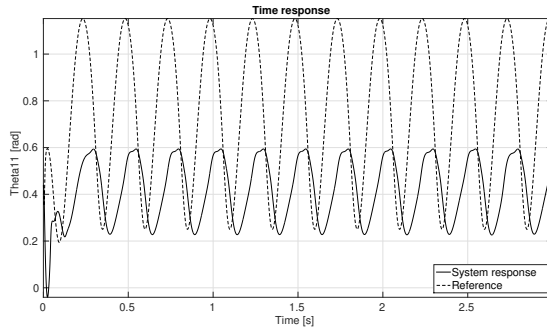


(g) Control effort  $u_{a2}$  in closed-loop simulation without robust controller.

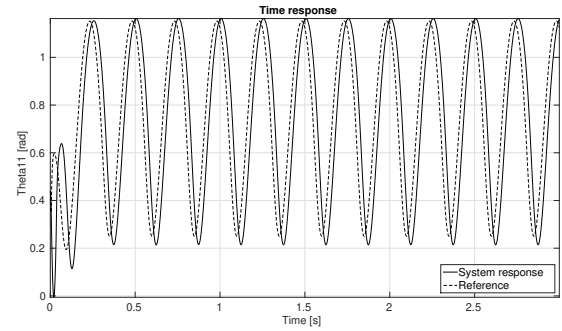


(h) Control effort  $u_{a2}$  in closed-loop simulation with robust controller.

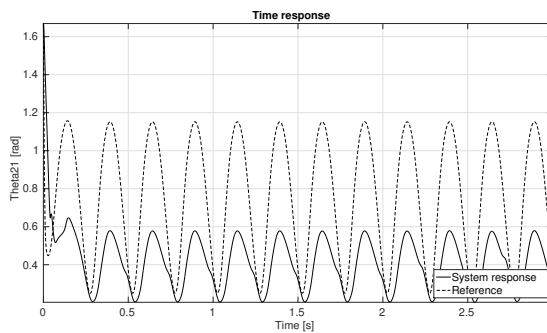
Figure 31: Time domain simulation with 2 Hz reference signal. Source: the author.



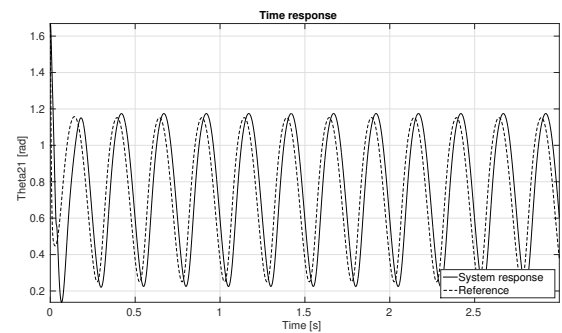
(a) Actuated joint  $\theta_{1,1}$  in closed-loop simulation without robust controller.



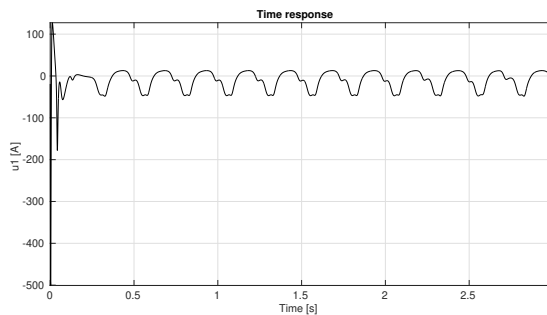
(b) Actuated joint  $\theta_{1,1}$  in closed-loop simulation with robust controller.



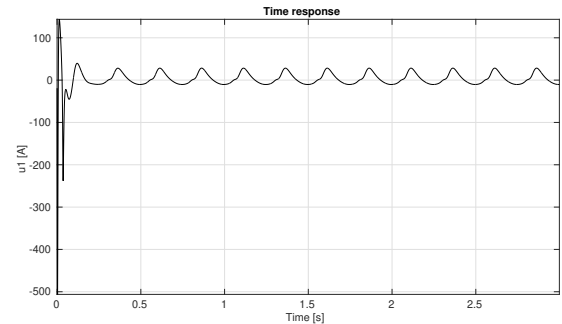
(c) Actuated joint  $\theta_{2,1}$  in closed-loop simulation without robust controller.



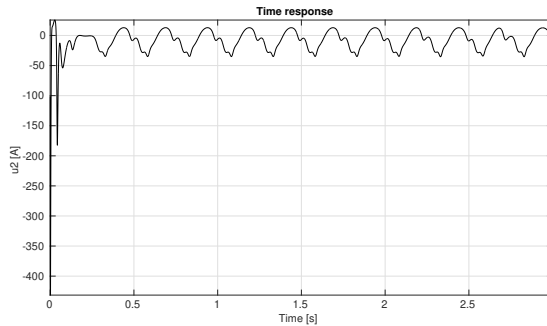
(d) Actuated joint  $\theta_{2,1}$  in closed-loop simulation with robust controller.



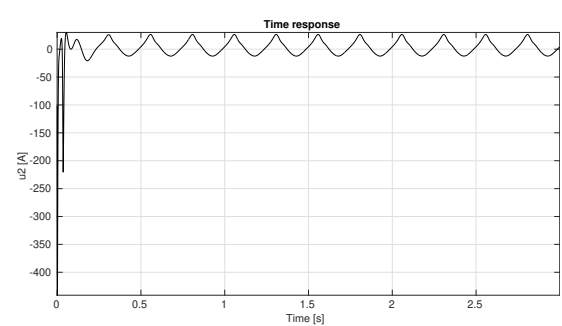
(e) Control effort  $u_{a1}$  in closed-loop simulation without robust controller.



(f) Control effort  $u_{a1}$  in closed-loop simulation with robust controller.



(g) Control effort  $u_{a2}$  in closed-loop simulation without robust controller.



(h) Control effort  $u_{a2}$  in closed-loop simulation with robust controller.

Figure 32: Time domain simulation with 4 Hz reference signal. Source: the author.

## 5 CONCLUSIONS

The 2-DOF parallel mechanism was modeled through a new method that consists in fragment the parallel system into serial subsystems and then piece them together through mechanical constraints obtained from the robot kinematics. With the robot dynamic model, the feedback linearization technique was applied in order to linearize the system. Since this technique does not account for possible model uncertainties, the feedback linearization alone would not be sufficient to control the real mechanism.

To deal with this issue, an  $H_\infty$  robust control design was proposed. Using the mixed-sensitivity method, the  $H_\infty$  robust controller was designed according to the uncertain model responses obtained through simulation and the desired performance criteria. With the synthesized controller, first a theoretical robust stability and performance analysis was carried out to validate that the resultant controller was sufficient to satisfy the design criteria. Then, a series of frequency and time domains simulations was performed to evaluate the system response, confirming the theoretical results accrued through the  $H_\infty$  robustness analysis.

As discussed in Chapter 4, the  $H_\infty$  robust controller enhanced the system robustness against disturbances and model uncertainties, in comparison to using the feedback linearization approach alone. Specially for low frequency inputs, the robust controller decreased the steady-state error abruptly when comparing its response with the feedback linearization alone case. Also, the THD measurement reduced in the presence of the robust controller, meaning that the residual nonlinear components from the imperfect model linearization due to model uncertainties and disturbances were less influential in this configuration.

Yet, the control effort presented a high magnitude during transient state, even in the presence of the  $H_\infty$  robust controller. Future work could address this aspect through a control redesign. Other suggestions for future work are the experimental implementation of this controller in the real parallel mechanism and a comparison of performance with the simulated case.

## REFERENCES

- ACHILI, B.; DAACHI, B.; AMIRAT, Y.; ALI-CHERIF, A.; DAACHI, M. A stable adaptive force/position controller for a c5 parallel robot: a neural network approach. *Robotica*, Cambridge University Press, v. 30, n. 7, p. 1177–1187, 2012.
- AKBARZADEH, A.; ENFERADI, J.; SHARIFNIA, M. Dynamics analysis of a 3-rrp spherical parallel manipulator using the natural orthogonal complement. *Multibody System Dynamics*, Springer, v. 29, n. 4, p. 361–380, 2013.
- AL-MAYYAH, A.; ALDAIR, A. A.; CHATWIN, C. Control of a 3-rrr planar parallel robot using fractional order pid controller. *International Journal of Automation and Computing*, Springer, v. 17, n. 6, p. 822–836, 2020.
- ALKAMACHI, A.; ERÇELEBI, E. H-infinity control of an overactuated tilt rotors quadcopter. *Journal of Central South University*, Springer, v. 25, n. 3, p. 586–599, 2018.
- ALMEIDA, R.; HESS-COELHO, T. Dynamic model of a 3-DOF asymmetric parallel mechanism. *Open Mechanical Engineering Journal*, Bentham Science Publishers B. V., P. O. Box 1673 Hilversum 1200 BR The Netherlands, v. 4, n. 1, p. 48–55, 2010.
- ALMEIDA, R.; HESS-COELHO, T. Dynamic model simplification of an asymmetric parallel robot for the development of real time control system. In: ABCM. *Proceedings of the XV International Symposium on Dynamic Problems of Mechanics*. Rio de Janeiro, Brazil, 2013. p. 17–22.
- ALTUZARRA, O.; EGGERS, P. M.; CAMPA, F. J.; ROLDAN-PARAPONIARIS, C.; PINTO, C. Dynamic modelling of lower-mobility parallel manipulators using the boltzmann-hamel equations. In: *Mechanisms, Transmissions and Applications*. New York, USA: Springer, 2015. p. 157–165.
- ANSARIESHLAGHI, F.; EBERHARD, P. Adaptive interaction control of a very flexible parallel robot manipulator. In: SPRINGER. *International Conference on Informatics in Control, Automation and Robotics*. [S.l.], 2019. p. 133–150.
- ARIAN, A.; DANAEI, B.; ABDI, H.; NAHAVANDI, S. Kinematic and dynamic analysis of the gantry-tau, a 3-dof translational parallel manipulator. *Applied Mathematical Modelling*, Elsevier, v. 51, p. 217–231, 2017.
- BEIRA, R.; SANTOS-CARRERAS, L.; SENGUL, A.; SAMUR, E.; CLAVEL, R.; BLEULER, H. An external positioning mechanism for robotic surgery. *Journal of System Design and Dynamics*, The Japan Society of Mechanical Engineers, v. 5, n. 5, p. 1094–1105, 2011.
- BRACEWELL, R. N. *The Fourier transform and its applications*. [S.l.]: McGraw-Hill New York, 1986. v. 31999.

- CHEN, W.-H.; YANG, J.; GUO, L.; LI, S. Disturbance-observer-based control and related methods—an overview. *IEEE Transactions on Industrial Electronics*, IEEE, v. 63, n. 2, p. 1083–1095, 2015.
- CODOUREY, A.; BURDET, E. A body-oriented method for finding a linear form of the dynamic equation of fully parallel robots. In: IEEE. *Proceedings of International Conference on Robotics and Automation*. New Mexico, USA, 1997. v. 2, p. 1612–1618.
- COLÓN, D. Connections between screw theory and cartan’s connections. In: SOCIEDADE BRASILEIRA DE AUTOMÁTICA. *Proceedings of the Congresso Brasileiro de Automática 2014*. Belo Horizonte, 2014.
- COLÓN, D. Cartan connections as a tool for kinematic chain calculation. *Journal of Control, Automation and Electrical Systems*, v. 26, n. 6, p. 630–641, 2015. ISSN 2195-3899.
- COLÓN, D. Cartan’s connection, fiber bundles and quaternions in kinematics and dynamics calculations. In: *Proceedings of the ASME 2015 IDETC/CIE 2015*. Boston: ASME, 2015.
- COLÓN, D. Cartan connection applied to dynamic calculation in robotics. *Journal of the Brazilian Society of Mechanical Sciences and Engineering*, v. 40, n. 8, p. 369, Jul 2018. ISSN 1806-3691.
- COUTINHO, A. G. *Contribuições à modelagem dinâmica e ao controle de manipuladores paralelos*. Thesis (Doctoral) — Universidade de São Paulo, 2020.
- COUTINHO, A. G.; BARTHOLOMEU, V. P.; STEVANI, I.; OLIVEIRA-FUESS, J. M. de; HESS-COELHO, T. A.; COLÓN, D. Design and control of a 2-DOF parallel mechanism. In: *Proceedings of the XXV ABCM International Congress of Mechanical Engineering*. Uberlândia, Brazil: [s.n.], 2019.
- COUTINHO, A. G.; COELHO, T. A. H. A new approach for obtaining the dynamic balancing conditions in serial mechanisms. *International Journal of Mechanisms and Robotic Systems*, Inderscience Publishers (IEL), v. 3, n. 1, p. 32–47, 2016.
- CRAIG, J. J. *Introduction to robotics: mechanics and control*. [S.l.]: Pearson/Prentice Hall Upper Saddle River, NJ, USA, 2005. v. 3. ISBN 978-0201543612.
- DASGUPTA, B.; MRUTHYUNJAYA, T. A newton-euler formulation for the inverse dynamics of the stewart platform manipulator. *Mechanism and machine theory*, Elsevier, v. 33, n. 8, p. 1135–1152, 1998.
- DOBRIANSKYJ, G. M.; COUTINHO, A. G.; HESS-COELHO, T. A. Development of a controller for a 3-dof robotic platform for user interaction in rehabilitation therapies. In: IEEE. *International Conference on Biomedical Robotics and Biomechatronics*. São Paulo, Brazil, 2014. p. 819–824.
- DOYLE, J.; GLOVER, K.; KHARGONEKAR, P.; FRANCIS, B. State-space solutions to standard h2 and h-infinity control problems. In: IEEE. *1988 American Control Conference*. [S.l.], 1988. p. 1691–1696.

- GALLARDO-ALVARADO, J.; RODRÍGUEZ-CASTRO, R.; DELOSSANTOS-LARA, P. J. Kinematics and dynamics of a 4-prur schönflies parallel manipulator by means of screw theory and the principle of virtual work. *Mechanism and Machine Theory*, Elsevier, v. 122, p. 347–360, 2018.
- GRZELCZYK, D.; STAŃCZYK, B.; AWREJCEWICZ, J. Prototype, control system architecture and controlling of the hexapod legs with nonlinear stick-slip vibrations. *Mechatronics*, Elsevier, v. 37, p. 63–78, 2016.
- HAIJAJI, A. E.; OULADSINE, M. Modeling and nonlinear control of magnetic levitation systems. *IEEE Transactions on industrial Electronics*, IEEE, v. 48, n. 4, p. 831–838, 2001.
- HARTMANN, V. N. *Contribuição ao controle experimental de robôs paralelos*. Thesis (Doctoral) — Universidade de São Paulo, 2018.
- HE, C.; WANG, G.; GONG, Z.; XING, Z.; XU, D. A control algorithm for the novel regenerative–mechanical coupled brake system with by-wire based on multidisciplinary design optimization for an electric vehicle. *Energies*, Multidisciplinary Digital Publishing Institute, v. 11, n. 9, p. 2322, 2018.
- HELTON, J. C.; DAVIS, F. Illustration of sampling-based methods for uncertainty and sensitivity analysis. *Risk analysis*, Wiley Online Library, v. 22, n. 3, p. 591–622, 2002.
- HELTON, J. C.; DAVIS, F.; JOHNSON, J. D. A comparison of uncertainty and sensitivity analysis results obtained with random and latin hypercube sampling. *Reliability Engineering & System Safety*, Elsevier, v. 89, n. 3, p. 305–330, 2005.
- HESS-COELHO, T. A.; HASZL, G. Desenvolvimento atual e tendências futuras em máquinas de cinemática paralela. In: *Anais do III Congresso Brasileiro de Engenharia de Fabricação*. Santa Catarina, Brazil: [s.n.], 2005.
- HESSELBACH, J.; PIETSCH, I.; BIER, C.; BECKER, O. Model-based control of plane parallel robots – how to choose the appropriate approach? In: *Proc. of 4th Chemnitz Parallel Kinematics Seminar (PKS2004)*. Chemnitz, Germany: [s.n.], 2004. p. 211–231.
- HONGLIANG, R. H-infinity loop-shaping design of flexible systems. In: IEEE. *2013 25th Chinese Control and Decision Conference (CCDC)*. Guiyang, China, 2013. p. 3279–3284.
- KOBEL, P.; CLAVEL, R. Micro robot for rotary desktop assembly line. In: IEEE. *2011 IEEE International Symposium on Assembly and Manufacturing (ISAM)*. Tampere Talo, Finland, 2011. p. 1–6.
- LANCZOS, C. *The variational principles of mechanics*. Massachusetts, USA: Courier Corporation, 2012. ISBN 0-486-65067-7.
- LI, Y.; XU, Q. Kinematics and inverse dynamics analysis for a general 3-prs spatial parallel mechanism. *Robotica*, Cambridge University Press, v. 23, n. 2, p. 219–229, 2005.
- LI, Y.; XU, Q. Dynamic modeling and robust control of a 3-prc translational parallel kinematic machine. *Robotics and Computer-Integrated Manufacturing*, Elsevier, v. 25, n. 3, p. 630–640, 2009.

- LI, Y.-W.; WANG, J.-S.; WANG, L.-P.; LIU, X.-J. Inverse dynamics and simulation of a 3-dof spatial parallel manipulator. In: IEEE. *2003 IEEE International Conference on Robotics and Automation*. Taipei, Taiwan, 2003. v. 3, p. 4092–4097.
- LIU, Y.-A.; TANG, S.; LIU, Y.; KONG, Q.; WANG, J. Extended dissipative sliding mode control for nonlinear networked control systems via event-triggered mechanism with random uncertain measurement. *Applied Mathematics and Computation*, Elsevier, v. 396, p. 125901, 2021.
- MA, T.; XIONG, H.; ZHANG, L.; DIAO, X. Control of a cable-driven parallel robot via deep reinforcement learning. In: IEEE. *2019 IEEE International Conference on Advanced Robotics and its Social Impacts (ARSO)*. [S.l.], 2019. p. 275–280.
- MANTEUFEL, R. Evaluating the convergence of latin hypercube sampling. In: *41st Structures, Structural Dynamics, and Materials Conference and Exhibit*. [S.l.: s.n.], 2000. p. 1636.
- MATHWORKS. *fft - Fast Fourier transform*. 2020. Accessed: 2020-04-20. Disponível em: <<https://www.mathworks.com/help/matlab/ref/fft.html>>.
- MATHWORKS. *lhsdesign - Latin hypercube sample*. 2020. Accessed: 2020-04-20. Disponível em: <<https://www.mathworks.com/help/stats/lhsdesign.html>>.
- MATHWORKS. *mixsyn - Mixed-sensitivity H-infinity synthesis method for robust control loop-shaping design*. 2020. Accessed: 2020-10-27. Disponível em: <<https://www.mathworks.com/help/robust/ref/lti.mixsyn.html>>.
- MATHWORKS. *thd - Total harmonic distortion*. 2020. Accessed: 2020-04-20. Disponível em: <<https://www.mathworks.com/help/signal/ref/thd.html>>.
- MERLET, J.-P.; GOSSELIN, C. Parallel mechanisms and robots. In: *Springer Handbook of Robotics*. New York, USA: Springer, 2008. p. 269–285.
- MOHAMMED, B.; HASNAA, E. H. Robust control of two link rigid manipulator with nonlinear dynamic model. In: IEEE. *2017 International Conference on Electrical and Information Technologies (ICEIT)*. Rabat, Morocco, 2017. p. 1–6.
- MOLINA, F. A. L. *Simulação e implementação experimental de um controlador preditivo generalizado para um robô orthoglide baseado na modelagem dinâmica*. Thesis (Doctoral) — Universidade Estadual de Campinas, 2012.
- NATAL, G. S.; CHEMORI, A.; PIERROT, F. Nonlinear control of parallel manipulators for very high accelerations without velocity measurement: stability analysis and experiments on par2 parallel manipulator. *Robotica*, Cambridge University Press, v. 34, n. 1, p. 43–70, 2016.
- ORSINO, R. M. M. *A contribution on modeling methodologies for multibody systems*. Thesis (Doctoral) — PhD thesis, São Paulo, Brazil: University of São Paulo. See <http://www.teses.usp.br/teses/disponiveis/3/3151/tde-22062016-160724/en.php>, 2016.

- ORSINO, R. M. M.; HESS-COELHO, T. A. A contribution on the modular modelling of multibody systems. *Proc. R. Soc. A*, The Royal Society, v. 471, n. 2183, p. 20150080, 2015.
- ORSINO, R. M. M.; HESS-COELHO, T. A.; PESCE, C. P. Analytical mechanics approaches in the dynamic modelling of delta mechanism. *Robotica*, Cambridge University Press, v. 33, n. 4, p. 953–973, 2015.
- OWEN, J.; JAMES, G. Robust h-infinity disturbance minimization by duality. *Systems & control letters*, Elsevier, v. 19, n. 4, p. 255–263, 1992.
- PACCOT, F.; ANDREFF, N.; MARTINET, P. A review on the dynamic control of parallel kinematic machines: Theory and experiments. *The International Journal of Robotics Research*, SAGE Publications Sage UK: London, England, v. 28, n. 3, p. 395–416, 2009.
- PAN, L.-x.; JIN, H.-z.; WANG, L.-l. Robust control based on feedback linearization for roll stabilizing of autonomous underwater vehicle under wave disturbances. *China Ocean Engineering*, Springer, v. 25, n. 2, p. 251, 2011.
- PASHKEVICH, A.; CHABLAT, D.; WENGER, P. Kinematics and workspace analysis of a three-axis parallel manipulator: the orthoglide. *Robotica*, Cambridge University Press, v. 24, n. 1, p. 39–49, 2006.
- PATEL, Y.; GEORGE, P. Parallel manipulators applications – a survey. *Modern Mechanical Engineering*, Scientific Research Publishing, v. 2, n. 03, p. 57, 2012.
- PILTAN, F.; SULAIMAN, N. B. Review of sliding mode control of robotic manipulator. *World Applied Sciences Journal*, v. 18, n. 12, p. 1855–1869, 2012.
- RACHEDI, M.; BOURI, M.; HEMICI, B. H-infinity feedback control for parallel mechanism and application to delta robot. In: IEEE. *22nd Mediterranean Conference on Control and Automation*. [S.l.], 2014. p. 1476–1481.
- RAMIREZ, F.; PACAS, M. Finite control set model based predictive control of a pmsm with variable switching frequency and torque ripple optimization. In: VDE. *PCIM Europe 2016; International Exhibition and Conference for Power Electronics, Intelligent Motion, Renewable Energy and Energy Management*. [S.l.], 2016. p. 1–8.
- RAMÍREZ-NERIA, M.; SIRA-RAMÍREZ, H.; LUVIANO-JUÁREZ, A.; RODRIGUEZ-ÁNGELES, A. Active disturbance rejection control applied to a delta parallel robot in trajectory tracking tasks. *Asian Journal of Control*, Wiley Online Library, v. 17, n. 2, p. 636–647, 2015.
- RICHARD, M.; CLAVEL, R. Modularity and parallel kinematics: an original design methodology applied to high precision. In: *Field Robotics*. Singapore: World Scientific, 2012. p. 933–940.
- RIGATOS, G.; SIANO, P.; POMARES, J. A nonlinear H-infinity control approach for closed-chain robotic mechanisms. In: *Proceedings - 2017 IEEE International Conference on Mechatronics, ICM 2017*. Gippsland, Australia: IEEE, 2017. p. 31–36. ISBN 9781509045389.

- RIGATOS, G.; SIANO, P.; RAFFO, G. An H-infinity nonlinear control approach for multi-DOF robotic manipulators. *IFAC-PapersOnLine*, v. 49, n. 12, p. 1406–1411, 2016.
- RUSTELL, M. *Knowledge extraction and the development of a decision support system for the conceptual design of liquefied natural gas terminals under risk and uncertainty*. Thesis (Doctoral) — University of Surrey, 2016.
- SHEIKHOLESLAMI, R.; RAZAVI, S. Progressive latin hypercube sampling: An efficient approach for robust sampling-based analysis of environmental models. *Environmental modelling & software*, Elsevier, v. 93, p. 109–126, 2017.
- SHIAU, T.-N.; TSAI, Y.-J.; TSAI, M.-S. Nonlinear dynamic analysis of a parallel mechanism with consideration of joint effects. *Mechanism and Machine Theory*, Elsevier, v. 43, n. 4, p. 491–505, 2008.
- SHMILOVITZ, D. On the definition of total harmonic distortion and its effect on measurement interpretation. *IEEE Transactions on Power delivery*, IEEE, v. 20, n. 1, p. 526–528, 2005.
- SINGH, Y.; SANTHAKUMAR, M. Inverse dynamics and robust sliding mode control of a planar parallel (2-prp and 1-ppr) robot augmented with a nonlinear disturbance observer. *Mechanism and Machine Theory*, Elsevier, v. 92, p. 29–50, 2015.
- SINGH, Y.; VINOTH, V.; KIRAN, Y. R.; MOHANTA, J. K.; MOHAN, S. Inverse dynamics and control of a 3-dof planar parallel (u-shaped 3-ppr) manipulator. *Robotics and Computer-Integrated Manufacturing*, Elsevier, v. 34, p. 164–179, 2015.
- SINGH, Y.; VINOTH, V.; SANTHAKUMAR, M. Dynamic modelling and control of a 3-dof planar parallel robotic (xy $\theta$ z motion) platform. *Procedia Materials Science*, Elsevier, v. 5, p. 1528–1539, 2014.
- SKOGESTAD, S.; POSTLETHWAITE, I. *Multivariable feedback control: analysis and design*. New York, USA: Wiley New York, 2007. v. 2.
- SLOTINE, J.-J. E.; LI, W. *Applied nonlinear control*. New Jersey, USA: Prentice hall Englewood Cliffs, NJ, 1991. v. 199. ISBN 0-13-040890-5.
- STAICU, S. Inverse dynamics of the 3-prr planar parallel robot. *Robotics and Autonomous Systems*, Elsevier, v. 57, n. 5, p. 556–563, 2009.
- STAICU, S. Recursive modelling in dynamics of delta parallel robot. *Robotica*, Cambridge University Press, v. 27, n. 2, p. 199–207, 2009.
- STAICU, S.; ZHANG, D. A novel dynamic modelling approach for parallel mechanisms analysis. *Robotics and Computer-Integrated Manufacturing*, Elsevier, v. 24, n. 1, p. 167–172, 2008.
- STAICU, S.; ZHANG, D.; RUGESCU, R. Dynamic modelling of a 3-dof parallel manipulator using recursive matrix relations. *Robotica*, Cambridge University Press, v. 24, n. 1, p. 125–130, 2006.
- STEIN, M. Large sample properties of simulations using latin hypercube sampling. *Technometrics*, Taylor & Francis Group, v. 29, n. 2, p. 143–151, 1987.

- STEVANI, I.; COUTINHO, A. G.; COLÓN, D.; HESS-COELHO, T. A. H-infinity control of a 3-DOF RRR spatial serial mechanism. In: SBA. *Proceedings of the XXII Brazilian Conference on Automation*. Paraíba, Brazil, 2018.
- TERRA, M. H.; MACIEL, B. C.; NAKASHIMA, P. H.; BERGERMAN, M. Underactuated Manipulator Robot Control By State Feedback Linearization Via H-infinity. *IFAC Proceedings Volumes*, v. 33, n. 14, p. 513–518, sep 2000.
- TIMCENKO, A.; ALLEN, P. Modeling dynamic uncertainty in robot motions. In: IEEE. *[1993] Proceedings IEEE International Conference on Robotics and Automation*. [S.l.], 1993. p. 531–536.
- TSAI, L.-W. *Robot analysis: the mechanics of serial and parallel manipulators*. [S.l.]: John Wiley & Sons, 1999.
- VUKIC, V. D.; MRVIC, J.; KATIC, V. A. High-order harmonics of the ac/dc converter, generated during the intermittent and continuous operation of gan-hemt power switches. In: VDE. *PCIM Europe 2019; International Exhibition and Conference for Power Electronics, Intelligent Motion, Renewable Energy and Energy Management*. [S.l.], 2019. p. 1–8.
- WANG, D.; WU, J.; WANG, L.; LIU, Y.; YU, G. A method for designing control parameters of a 3-dof parallel tool head. *Mechatronics*, Elsevier, v. 41, p. 102–113, 2017.
- WEN, S.; ZHA, Y.; YU, H.; MANFREDI, L.; LI, X.; WANG, S. Fuzzy neural network algorithm based on the delay compensation force/position control structure of a redundant actuation parallel robot. In: IEEE. *2019 WRC Symposium on Advanced Robotics and Automation (WRC SARA)*. [S.l.], 2019. p. 142–147.
- WU, W.; ZHU, S.; WANG, X.; LIU, H. Closed-loop dynamic parameter identification of robot manipulators using modified fourier series. *International Journal of Advanced Robotic Systems*, SAGE Publications Sage UK: London, England, v. 9, n. 1, p. 29, 2012.
- WU, Y.; LIU, T.; WU, Y.; ZHANG, Y. H-infinity output tracking control for uncertain networked control systems via a switched system approach. *International Journal of Robust and Nonlinear Control*, Wiley Online Library, v. 26, n. 5, p. 995–1009, 2016.
- XI, F.; SINATRA, R. Inverse dynamics of hexapods using the natural orthogonal complement method. *Journal of manufacturing systems*, Elsevier, v. 21, n. 2, p. 73–82, 2002.
- YANG, J.; CHEN, W.-H.; LI, S. Non-linear disturbance observer-based robust control for systems with mismatched disturbances/uncertainties. *IET control theory & applications*, IET, v. 5, n. 18, p. 2053–2062, 2011.
- YANG, J.; LI, S.; CHEN, W.-H. Nonlinear disturbance observer-based control for multi-input multi-output nonlinear systems subject to mismatching condition. *International Journal of Control*, Taylor & Francis, v. 85, n. 8, p. 1071–1082, 2012.
- YAO, J.; GU, W.; FENG, Z.; CHEN, L.; XU, Y.; ZHAO, Y. Dynamic analysis and driving force optimization of a 5-dof parallel manipulator with redundant actuation. *Robotics and Computer-Integrated Manufacturing*, Elsevier, v. 48, p. 51–58, 2017.

- YUN, Y.; LI, Y. Active vibration control based on a 3-dof dual compliant parallel robot using lqr algorithm. In: IEEE. *2009 IEEE/RSJ International Conference on Intelligent Robots and Systems*. [S.l.], 2009. p. 775–780.
- ZEINALI, M.; NOTASH, L. Adaptive sliding mode control with uncertainty estimator for robot manipulators. *Mechanism and Machine Theory*, Elsevier, v. 45, n. 1, p. 80–90, 2010.
- ZHAN, Z.; ZHANG, X.; JIAN, Z.; ZHANG, H. Error modelling and motion reliability analysis of a planar parallel manipulator with multiple uncertainties. *Mechanism and Machine Theory*, Elsevier, v. 124, p. 55–72, 2018.
- ZHANG, X.; ZHANG, X.; CHEN, Z. Dynamic analysis of a 3-rrr parallel mechanism with multiple clearance joints. *Mechanism and Machine Theory*, Elsevier, v. 78, p. 105–115, 2014.
- ZHAO, Y.; GAO, F. Inverse dynamics of the 6-dof out-parallel manipulator by means of the principle of virtual work. *Robotica*, Cambridge University Press, v. 27, n. 2, p. 259–268, 2009.
- ZHOU, K.; DOYLE, J. C. *Essentials of robust control*. [S.l.]: Prentice hall Upper Saddle River, NJ, 1998. v. 104.
- ZHU, Z.; LI, J.; GAN, Z.; ZHANG, H. Kinematic and dynamic modelling for real-time control of tau parallel robot. *Mechanism and machine theory*, Elsevier, v. 40, n. 9, p. 1051–1067, 2005.
- ZUBIZARRETA, A.; CABANES, I.; MARCOS, M.; PINTO, C. A redundant dynamic model of parallel robots for model-based control. *Robotica*, Cambridge University Press, v. 31, n. 2, p. 203–216, 2013.